THE UNIVERSITY of EDINBURGH
Institute of Materials and Processes
School of Engineering

The Behaviour of Nanocolloidal Particles on Mica: Investigations Using Atomic Force Microscopy

Richard John Walker

A thesis submitted to the University of Edinburgh
for the Degree of Doctor of Philosophy

February 2010

In memory of David

Declaration

I declare that this thesis has been composed by myself and is all my own work except where otherwise stated.

_____

John Walker
February 2010

Acknowledgements

In the time that I have worked on this thesis there have been many people that have assisted me along the way. I would like to take this time to acknowledge the individuals that have made the difference in this time. This work could have not been possible without the help, guidance and support of these people.

First and foremost, I would like to thank my supervisor Dr. Vasileios Koutsos. During the past four and a half years he has offered both his expert advice and unique form of encouragement as I have overcome both technical issues and experimental frustration. There has never been a language barrier and he has always respected me and treated me as an equal, and is never shy about having an opinion on any matter, be it academia or foreign politics. Without doubt his help, especially during the final months of authoring this thesis, have been crucial in its completion.

I am also grateful to both Dr. Jane Blackford and to Prof. Chris Hall for their open door policy; offering me both encouragement and support when I have needed it throughout my time as a postgrad. I have immensely appreciated their time and to be treated as a friend rather than an understudy, their friendly and good spirited natures have helped me through some rough patches!

I am thankful to Dr. Andrew Schofield from the Physics Department of Edinburgh University for his contribution of colloidal particles and expert advice on their manufacturing, behaviour and general knowledge on the subject matter.

I am very thankful to my colleagues Dr. Daniel Higgins, Dr. Dave Curry, Dr. Frederic Madani, Dr. Manos Dr. Qianqian Li, Dr. Andrea Hamilton, Dr. Alexandros Chremos, Dr. Emmanouil Glynos, Dr. Kostas Kiritsis, Gerasimos Skouvaklis, Iain Roberts, Jovana Radulovic, Apostolos Evangelopoulos, Michalis Kalloudis, Tom Barraclough and Julia Morris for their friendship, advice and for providing me with an enjoyable working environment and coffee break companionship.

I thank my parents Raymond and Margaret for their unwavering support and love, even when things went over schedule and I still didn't have a "real job". I'm sorry that this has meant that I have been away from home for far too long. To my sisters Alison and Kathryn who have always been their supporting me in their own unique way, we are now a family of doctors!

Finally, and most importantly, to my fiancée Sarah. This PhD has given me the best gift anyone could ask for, a soul mate. Because of it I was able to meet you and in its time I have gotten to know you, fall in love and ask you to be my wife. I can truly say that I have no regrets about having spent these years doing this thesis as I spent them with you, and now with its completion we shall soon be married and spend our lives together. You have always been there with your unquestioning support when various aspects of this work have gotten me down and your constant help in whatever form has made the experience that much more enjoyable. I would be lost without you.

For funding me during my PhD, many thanks go to the School of Engineering and Centre for Material Science and Engineering of the University of Edinburgh.

Abstract

In this Thesis we used atomic force microscopy (AFM) to investigate systematically the behaviour of both electrostatically stabilised silica and sterically stabilised polystyrene (PS) colloidal systems on freshly cleaved mica substrates. For the silica colloidal nanoparticles we explored the effect of colloidal suspension concentration, particle size, and different application techniques on both the adsorption behaviour and subsequent structuring of the particles. For the PS colloidal nanoparticles we explored concentration effects and experimented with both dip-coating and droplet application techniques.

We showed that silica nanoparticles adsorbed onto mica via irreversible adsorption that possessed lateral mobility due to the weak attraction between the nanoparticles and the substrate, facilitating subsequent capillary structuring of the nanoparticles during drying. We associated the effects of volume fraction with Debye screening, and kinetics effects with particle size and volume fraction. We also successfully imaged a partially dried film and showed the role of convective/capillary forces in the structuring of the nanoparticles. Studies with variations in particle size generated a number of different topography structures; with dewetting phenomena observed for 10 nm nanoparticles and the formation of crystalline structures for 100 nm nanoparticles. Spin coating techniques were used to produce even larger crystalline structures of nanoparticles. Size dependent ordering occurred for low concentration samples due to the polydispersity of the colloidal suspension. We showed that acceleration can affect interparticle spacing. We also studied the role of rotational speed on the crystallinity of the particle configurations and showed how fine tuning of rotational speed can generate large scale monolayer crystalline formations of nanoparticles.

Contents

Chapter 1: Introduction

The world of colloidal science was once an overlooked branch of chemistry that has in recent years become a multidisciplined, billion dollar industry at the cutting edge of modern research. Applications of colloidal suspensions and their adsorption onto surfaces is the basis of many industrial processes, including waste water management, paper manufacturing, the application of paints and coatings and many chemical processes.

One of the great prospects for colloidal science is the exploitation of self assembly techniques [1-5]. The relentless drive to shrink down the scale at which devices can be manufactured has begun to approach the physical limits of what top down manufacturing techniques can achieve; and so attention has turned to the use of bottom up techniques [6, 7] for manufacturing in many areas of industry. Current applications of bottom up processes using self assembly techniques include photonics [8], biosensors [9], the semiconductor industry [1, 10] and quantum dot technology [11]. Colloidal particles have been widely used as a stock material in constructing nanostructures due to their modifiable physicochemical properties [12, 13]. This has fuelled research into the behaviour of colloidal particles in suspension [14, 15], their subsequent deposition or adsorption [16-18] onto a surface and their final structuring during drying [19-27]. Silica colloidal particles [28] in particular have been used extensively in research due to their native surface chemistry providing an effective and easily attained colloidal stability when suspended in a polar liquid [29]. Research into the behaviour of silica colloids on surfaces has tended to focus on systems where the colloidal particle and the substrate have an opposite electrostatic charge. Such systems are bound by irreversible and immobile adsorption of the nanoparticles, which can affect the formation of close packed structures as observed by Johnson *et al*. [30]. Studies of systems where a similar charge exists between the nanoparticle and the substrate are however scarce, with only a few systems having been investigated using irregular and polydisperse alumina grains on mica [31, 32]. Such systems were described as irreversible (i.e. no desorption) but with lateral mobility due to the weak adsorption of the particle to the substrate. There are many aspects of the behaviour of such systems that have not been explored or quantified in current literature. It is the objective of this thesis to

fully explore the behaviour of such systems in-depth, providing an alternative system for bottom up self assembly of colloidal nanoparticles.

The work in this thesis is organised as follows:

In **Chapter 2** a brief theoretical background is provided to familiarise the reader with what exactly is a colloid, how colloids interact with the world around them and how we can dictate the colloidal behaviour of a suspension. The surface properties of silica and mica are illustrated and concepts in self assembly and dewetting phenomena are also discussed. Finally a review on some of the basic concepts of atomic force microscopy is presented along with modes of operation.

In **Chapter 3** we used dip-coating and droplet evaporation methodologies of silica colloid suspensions of ≈ 85 nm to adsorb and deposit silica nanoparticles on mica surfaces. We investigated the roles of particle mobility and capillary forces on the adsorption and structuring of the nanoparticles on mica. Our findings indicated that the system has irreversible adsorption with lateral mobility due to the weak attraction between the particles and the substrate. The final structuring of the particles was governed by the emergence of capillary forces between neighbouring particles which led to close packed formations. We also imaged partially dried samples which left an ultrathin film of the fluid on the mica surface.

In **Chapter 4** we expanded our range of particle sizes to include 10 nm, 50 nm and 100 nm nanocolloids. We discussed the implications that particle size and concentration have on the adsorption behaviour of the systems in terms of volume fraction and kinetics effects. The magnitude of capillary forces for different particle sizes was assessed and found to be effective for the self assembly of crystalline structures only for larger nanoparticles at high adsorption densities, while dewetting phenomenon is found to dictate the structuring behaviour of smaller 10 nm particles.

In **Chapter 5** we explored the use of spin coating as an alternative method of self assembly of colloidal particles. We employed silica nanoparticles of 150 nm and

deposited them onto freshly cleaved mica using a variety of different rotational speeds, accelerations and colloidal concentrations. We observed a diverse range of structuring in the colloidal particles. We discussed the effects of centrifugal and viscous forces on the surface of the spinning substrate and their relationship with the packing configurations of the colloidal particles. We also observed particle structuring in a *size dependent* ordering configuration, and successfully produced large monocrystal structures of colloidal particles on mica.

In **Chapter 6** we moved from electrostatically stabilised to sterically stabilised colloidal suspensions, and investigated the nanostructures and ultrathin films resulting from the deposition and adsorption of polystyrene nanocolloidal particles and methoxy poly(ethylene glycol) methacrylate surfactants on mica surfaces from mixed suspensions in water. We observed uniform ultrathin films and extended islands of the surfactant oligomers indicating their self-assembly in monolayers and multilayers while the polystyrene nanoparticles were embedded within the surfactant structures. Dip-coating induced the formation of extended nanoparticle clusters with colloidal crystalline structuring.

A Final Note

The Chapters have been written in a way that can be both read in succession and independently.

1.1. References

[1] J. H. Fendler, Chemistry of Materials 13 (2001) 3196-3210.
[2] J. Texter, M. Tirrell, Aiche Journal 47 (2001) 1706-1710.
[3] G. M. Whitesides, B. Grzybowski, Science 295 (2002) 2418-2421.
[4] S. C. Glotzer, M. J. Solomon, N. A. Kotov, Aiche Journal 50 (2004) 2978-2985.
[5] A. Fahmib, A. D'Aleoc, L. De Colad, F. Vogtle, Systems Self-Assembly: Multidisciplinary Snapshots (2008) 1.
[6] M. Shimomura, T. Sawadaishi, Current Opinion in Colloid & Interface Science 6 (2001) 11-16.
[7] D. Mijatovic, J. C. T. Eijkel, A. van den Berg, Lab on a Chip 5 (2005) 492-500.
[8] S. H. Im, Y. T. Lim, D. J. Suh, O. O. Park, Advanced Materials 14 (2002) 1367-1369.
[9] O. D. Velev, E. W. Kaler, Langmuir 15 (1999) 3693-3698.
[10] P. Hanarp, D. S. Sutherland, J. Gold, B. Kasemo, Colloids and Surfaces a-Physicochemical and Engineering Aspects 214 (2003) 23-36.
[11] P. Guyot-Sionnest, Comptes Rendus Physique 9 (2008) 777-787.
[12] M. Qhobosheane, S. Santra, P. Zhang, W. H. Tan, Analyst 126 (2001) 1274-1278.
[13] M. S. Romero-Cano, A. Martin-Rodriguez, G. Chauveteau, F. J. de las Nieves, Journal of Colloid and Interface Science 198 (1998) 266-272.
[14] J. Z. Xue, E. Herbolzheimer, M. A. Rutgers, W. B. Russel, P. M. Chaikin, Physical Review Letters 69 (1992) 1715-1718.
[15] M. Elimelech, C. R. Omelia, Langmuir 6 (1990) 1153-1163.
[16] Z. Adamczyk, Journal of Colloid and Interface Science 229 (2000) 477-489.
[17] Z. Adamczyk, L. Szyk, Langmuir 16 (2000) 5730-5737.
[18] Z. Adamczyk, B. Siwek, M. Zembala, Colloids and Surfaces 62 (1992) 119-130.
[19] N. Rana, S. T. Yau, Nanotechnology 15 (2004) 275-278.
[20] S. Maenosono, T. Okubo, Y. Yamaguchi, Journal of Nanoparticle Research 5 (2003) 5-15.
[21] N. Samid-Merzel, S. G. Lipson, D. S. Tannhauser, Physica A 257 (1998) 413-418.
[22] J. Aizenberg, P. V. Braun, P. Wiltzius, Physical Review Letters 84 (2000) 2997-3000.
[23] P. A. Kralchevsky, N. D. Denkov, Current Opinion in Colloid & Interface Science 6 (2001) 383-401.
[24] P. A. Kralchevsky, K. Nagayama, Langmuir 10 (2002) 23-36.
[25] A. S. Dimitrov, K. Nagayama, Langmuir 12 (1996) 1303-1311.
[26] N. D. Denkov, O. D. Velev, P. A. Kralchevsky, I. B. Ivanov, H. Yoshimura, K. Nagayama, Langmuir 8 (1992) 3183-3190.
[27] K. Nagayama, Colloids and Surfaces a-Physicochemical and Engineering Aspects 109 (1996) 363-374.
[28] R. K. Iler, The chemistry of silica: solubility, polymerization, colloid and surface properties, and biochemistry, Wiley, New York, 1979, p. xxiv, 866 p.
[29] S. H. Behrens, D. G. Grier, Journal of Chemical Physics 115 (2001) 6716-6721.

[30] C. A. Johnson, A. M. Lenhoff, Journal of Colloid and Interface Science 179 (1996) 587-599.
[31] A. Thill, O. Spalla, Langmuir 18 (2002) 4783-4789.
[32] O. Spalla, S. Desset, Langmuir 16 (2000) 2133-2140.

Chapter 2: Theoretical and Experimental Background

2.1. Definition of a Colloid

The behaviour of colloids has become an ever expanding area of research due to the increasing number of applications in both scientific and industrial fields where their unique properties are being exploited. Such areas include bio sensors, catalyst processes, microelectronics industry and drug delivery applications [1]. But what is a colloid? While it is easy for us to understand materials in terms of solids liquids and gases, materials that span these states can be less well defined. For instance, brine is a *solution* of salt dissolved at a molecular level into a medium of water forming a homogenous mixture. A *colloidal suspension* however is not homogeneous, but in fact consists of a dispersed or discontinuous phase distributed uniformly throughout a dispersion or continuous medium. These combinations of phases and mediums give rise to a multitude of different examples of materials that can be referred to as colloids, a few of which are given in Table 2-1.

		Dispersed Medium		
		GAS	**LIQUID**	**SOLID**
Continuous Medium	**GAS**	**None** (All gases are soluble)	**Liquid Aerosol** Examples: Fog, mist	**Solid aerosol** Examples: Smoke, air particulates
	LIQUID	**Foam** Examples: Whipped cream, Shaving foam	**Emulsion** Examples: mayonnaise, hand cream	**Sol** Examples: Milk, pigmented ink, blood
	SOLID	**Solid Foam** Examples: Aerogel, Styrofoam	**Gel** Examples: Butter, gelatine, jelly, cheese	**Solid Sol** Examples: Cranberry glass, ruby glass

Table 2-1. Table outlining the classification of different colloidal systems by their dispersed and continuous phases.

Disperse systems where all the particles are of a similar dimension are known as monodisperse, and systems where the particles are present in a range of sizes are referred to as polydisperse.

For the majority of colloidal materials the size of the dispersed medium lies in the dimension range of 1 to 1000 nanometers, although this is not a set limit to define a

colloidal system. This range of scale gives colloidal systems one of its defining characteristics, a larger surface area to volume ratio at the dispersed phase. Consider a cube of edge length 1 cm. Its volume is 1 cm^3 and its area 6 cm^2. If we were to divide this cube up into 1000 cubes of 1 mm its volume would still be 1 cm^3 (1000 mm^3) but the effective exposed surface area would now be 60 cm^3, at 1 μm the surface area has become 60,000 cm^3. It is clear therefore that the interfacial properties between the dispersed and continuous mediums must play a dominant role in determining the behaviour of a colloidal system.

It is normally desired that a colloidal suspension of particles remains dispersed and suspended within its medium. Due to their size colloidal particles are subject to random molecular collisions from the surrounding medium in a phenomenon known as Brownian motion. Such motion maintains the dispersion of the colloid particles throughout the colloidal suspension. Over time the effects of attractive forces that occur between particles will cause them to aggregate together until gravitation sedimentation occurs. In order to maintain a well dispersed suspension, it is vital that the attractive forces between these particles be counterbalanced by repulsive ones, preventing particle aggregation.

2.2. Colloidal Particle Interactions

For the context of this thesis the range of colloidal interactions covered in the theoretical background will be limited to van der Waals, electrostatic and steric forces, as these are the most dominant forces affecting particle behaviour until the interaction distance has reached in the region of a few nanometers (where solvation/hydration forces come into play). The following literature review is composed from a selection of books [2-6] and other references where noted. For a more in-depth study of the range of particle-particle and particle-surface interactions it is recommended that the referenced books are considered.

2.2.1. Van der Waals Interactions

Let us start by considering the forces that occur between two molecules. The van der Waals interaction between two molecules is composed of three distinct interactions that all vary with the inverse sixth power of the separation distance. The Keesom or *orientation* interaction evaluates interactions involving permanent dipole-dipole molecules, the Debye or *induction* interaction evaluates interactions between dipole-induced dipole interactions and finally the London or *dispersion* interaction evaluates the interaction between all atoms and molecules due to the quantum induced instantaneous dipole interactions. Of the three interactions the dispersion interaction component is the most important due to it always being present (while the induction and orientation interactions are dependent on the properties of the molecules.) As such we will discuss it in more detail.

London Dispersion forces exist between all atoms and molecules. They exist because the electron clouds around atoms are not stationary but are in constant motion and therefore statistically there will be instances where the electron cloud will not have a uniform charge. London forces can be exhibited by nonpolar molecules because electron density moves about a molecule probabilistically (based on Schrödinger equation for the variation with time of the quantum state of a physical system). When

an electron is on one side of the nucleus, this side becomes slightly negative; this in turn repels electrons in neighbouring atoms, making these regions slightly positive. This *induced instantaneous dipole* causes a brief electrostatic attraction between the two molecules (Figure 2-1). The electron immediately moves to another point and the electrostatic attraction is broken. Alternatively bond vibrations in molecules may produce the oscillations or they may be triggered by random, instantaneous coalescing of electrons in atoms.

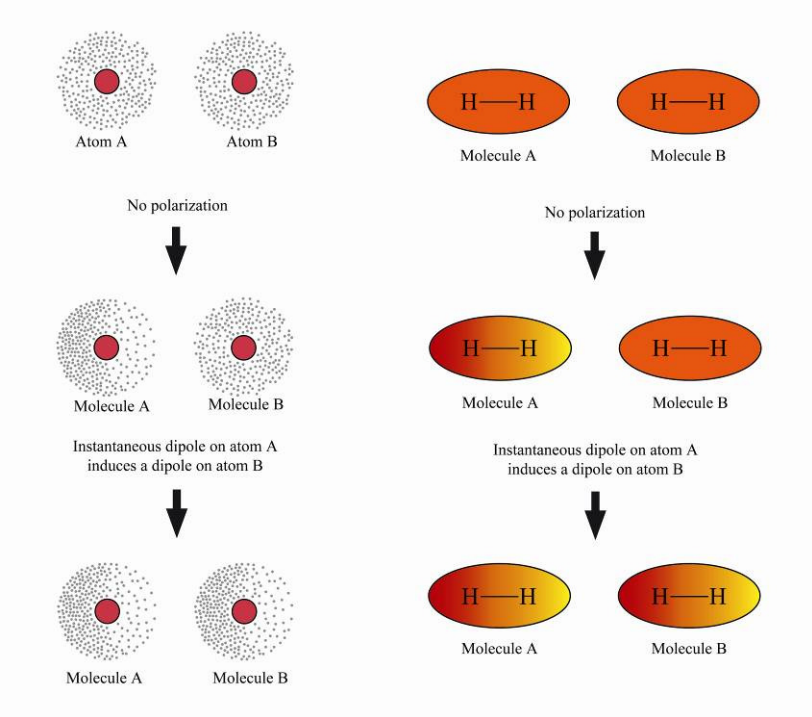

Figure 2-1. Simplified illustration of dispersion forces.

The electron-rich and electron-poor regions of the induced dipole may not persist for more that 10^{-14} or 10^{-15} seconds, but if they can polarise the electron distribution on an adjacent molecule, electron clouds on the two molecules may begin to oscillate cooperatively with each other. The dipoles are transitory but aligned, and a net attractive force pulls the molecules together. At closer range, the oscillation becomes even more effective.

The London expression for the dispersion interaction energy between two atoms or molecules is:

$$v_L = -\frac{C_L}{r^6} = -\frac{3\alpha_{01}\alpha_{02}}{2(4\pi\varepsilon_0)^2}\frac{I_1 I_2}{I_1 + I_2}\frac{1}{r^6} \qquad \textbf{2-1}$$

where C_L is referred to as the London constant and I is the ionization potential ($I = hf_i$ where h is the Planck constant and f_i is the ionisation frequency).

The London theory for the dispersion forces has two serious shortcomings. It assumes that atoms and molecules have only a single ionization potential and it cannot handle the interactions of molecules in a solvent. McLachlan presented a generalised theory of the van der Waals forces which included in one equation the Keesom, Debye and Dispersive forces. This theory was also applicable to interactions in a solvent medium.

$$v_{vdW} = -\frac{6kT}{3(4\pi\varepsilon_0)^2 r^6}\left(\frac{\alpha_1(0)\alpha_2(0)}{2\varepsilon_m^2(0)} + \sum_{n=1}^{\infty}\frac{\alpha_1(iv_n)\alpha_2(iv_n)}{2\varepsilon_m^2(iv_n)}\right) \qquad \textbf{2-2}$$

where $\alpha_j(iv_n)$ are the electronic polarizabilities at imaginary frequencies iv_n for molecule-*j*, and $\varepsilon_m(iv_n)$ is the permittivity of the medium between the molecules at imaginary frequencies iv_n. From McLachlans equation we can assess how the van der Waals interactions are affected by the presence of a solvent medium.

- Dispersion force contribution is still significantly greater than that of the dipolar contribution.
- It can be shown that the van der Waals interaction is significantly weakened by the presence of a solvent.
- The dispersion force between dissimilar molecules can be attractive or repulsive. It is repulsive when the refractive index of the medium is an

intermediary of the particles refractive index. For identical particles it is always attractive.

Due to the fact that the period of the fluctuation in the dipoles is comparable to that of the time taken for the fluctuation to be transmitted, at long distances the dispersion energy between two atoms begins to decay even faster than $-1/r^6$, approaching $-1/r^7$ for separation distances approaching 100 nm. This phenomenon is referred to as the *retardation* effect.

By assuming additivity and ignoring retardation effects, a selection of van der Waals interaction energies formulae can be derived from the integration of the interatomic van der Waals pair potential ($v_{vdW} = -C/r^6$) for sphere-sphere and sphere-surface interactions, as shown in Figure 2-2. These interaction laws are given in terms of the conventional Hamaker constant $A = \pi^2 C\rho_1\rho_2$ where ρ_1 and ρ_2 are the number of atoms per unit volume in the two bodies. Typical Hamaker constants for solids and liquids in a vacuum are approximately 10^{-19}J.

While simple pairwise additive calculations are applicable for systems in a vacuum their suitability for calculations of atom or molecules interacting in a medium become problematic. Firstly the effective polarizability of an atom changes when it is surrounded by other atoms. Secondly, in its simplest form, if a third atom is present then it too will become polarized by the instantaneous field of one of the other two atoms and its induced dipole field will affect the other atoms. The instances of field reflections cause the additivity calculations to quickly breakdown. This limitation can be completely avoided by employing the Lifshitz theory. It was shown that a charge Q in a medium of dielectric constant ε_2 at a distance D from the plane surface of a second medium of dielectric constant ε_3 experiences a force as if there was an 'image' charge at distance D on the other side of the boundary. Combining this with the van der Waals interactions of a charge Q and a planar surface, the excess bulk or volume polarizability of a planar dielectric medium 2 in medium 3 could be expressed in terms of the purely macroscopic properties of the media. From this result the Hamaker constant for the interaction of two media (1 & 2) across a third

medium 3 can be expressed in terms of McLachlan's equation (Equation 2-2) simply by knowing the dielectric permittivity of the three media involved.

The summation of a Hamaker constant for two particles of type '1' in a medium of type '3' can be approximately calculated using the following expression:

$$A_{13} \approx \left(A_{11}^{1/2} - A_{33}^{1/2}\right)^2 \qquad \textbf{2-3}$$

It should be noted that with the Lifshitz theory it is only the method by which the Hamaker constant is calculated that has changed, and the van der Waals equations from Figure 2-2 are still valid.

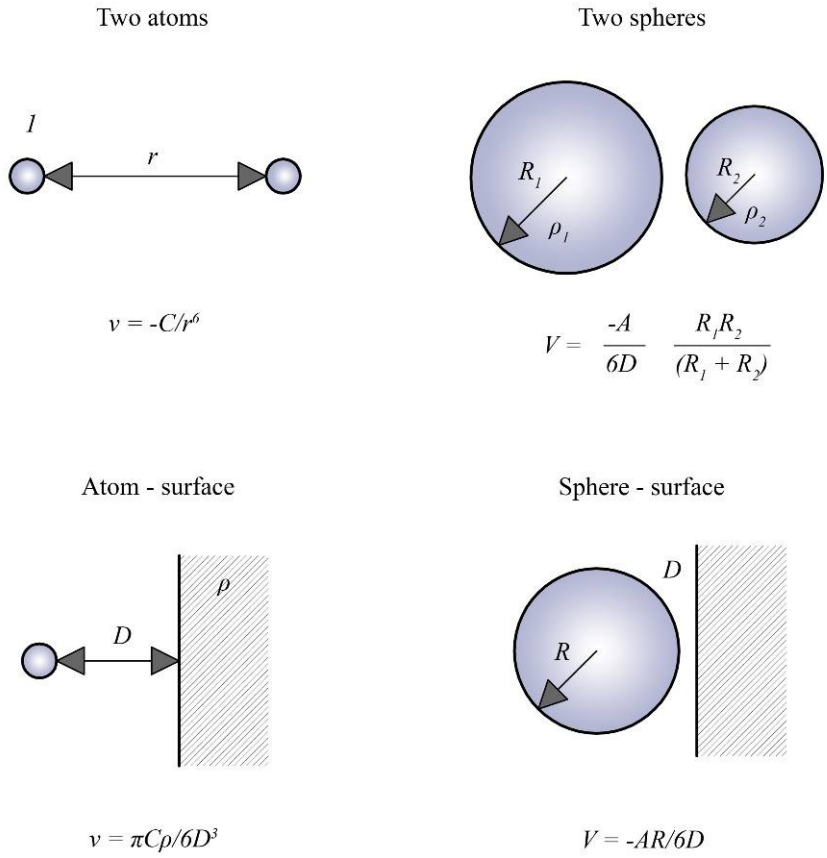

Figure 2-2. Non-retarded van der Waals interaction potential between sphere – sphere (top) and sphere – surface (bottom) systems calculated on the basis of pair wise additively (Hamaker summation method) Taken from Israelachvili.

At very short separation distances there exists a strong repulsion force generated by the overlap of the electron clouds of atoms. This force is commonly referred to as hard core repulsion or, for ions, the Born repulsion. The force is characterised by a very short range and its magnitude is rapidly increasing as the atoms approach.

The Boltzmann distribution law states that if the energy associated with some state or condition of a system is ε then the frequency with which that state or condition occurs, or the probability of its occurrence, is proportional to

$$e^{-\frac{\varepsilon}{k_B T}} \qquad \textbf{2-4}$$

where T is the system's absolute temperature and k_B is the Boltzmann constant.

2.2.2. Electrostatic Interactions

Many interfaces in an aqueous system carry an electrical charge. Interfaces with a similar charge will repel one another due to the Coulomb's law. This repulsion occurs between any "like-charge" interfaces and is an important factor in determining the colloidal behaviour of aqueous systems. Let us consider a single colloidal sphere suspended in a liquid medium. At the interface between the surface of the particle and the liquid we will assume any charged surface to be uniformly charged. Each colloid carries a "like" electrical charge which produces a force of mutual electrostatic repulsion between adjacent particles. The charging of a surface in a liquid can originate from either the ionisation or dissociation of surface groups or by the adsorption of ions from solution onto a previously uncharged surface. The final surface charge is balanced by an equal but oppositely charged region of counter-ions, some of which are bound, usually transiently, to the surface while others form an atmosphere of ions in rapid thermal motion close to the surface, known as the diffuse electrical double layer (EDL).

The electrical double layer model (Figure 2-3) is used to visualize the ionic environment in the vicinity of a charged colloid and explains how the electrostatic repulsive force occurs. Ions of the same sign as the charged surface are referred to as co-ions and those of an opposite sign are called counter-ions. In our model the colloidal particle is negatively charged, although positively charged particles would behave in a corresponding manner.

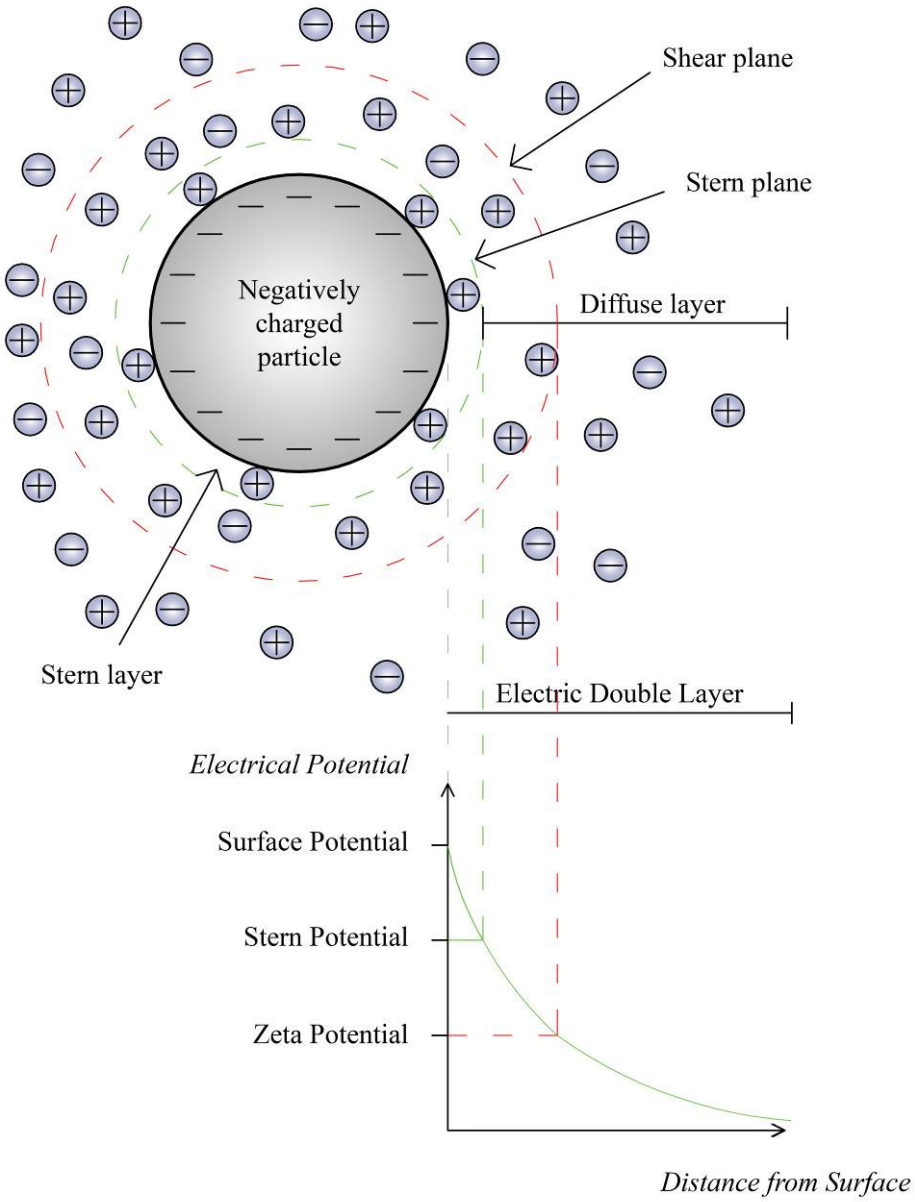

Figure 2-3 Schematic of the Electrical Double Layer with an electrical potential graph for reference.

Initially, attraction from the charged colloidal surface causes some of the counter-ions to form a firmly attached layer around the surface of the colloid; this layer of counter-ions is known as the *Stern layer*. The stern layer can be modelled using a

Langmuir isotherm, which describes the formation of a monolayer. In this instance we have a monolayer of mainly counter-ions at the surface whose population is a function of the electrostatic potential (as well as chemical interactions). If we define the surface potential as ψ_0 then the potential at the stern plane is ψ_σ due to the effect of the adsorbed ions.

Beyond the stern plane additional counter-ions are still attracted by the colloidal surface charge, but now they are repelled by the Stern layer as well as by other positive ions that are also approaching the colloid due to thermal motion. This dynamic equilibrium between diffusion and electrostatics results in the formation of a *diffuse layer* of counter-ions. They have a high concentration near the surface which gradually decreases with distance, until it reaches the value of the counter-ion concentration in the solution. In a similar, but opposite, fashion there is a lack of co-ions in the neighbourhood of the surface, because they are repelled by the negative colloid. Their concentration will gradually increase with distance, as the repulsive forces of the colloid are screened out by the counter-ions, until the value of the co-ion concentration in the solution is reached (Figure 2-4).

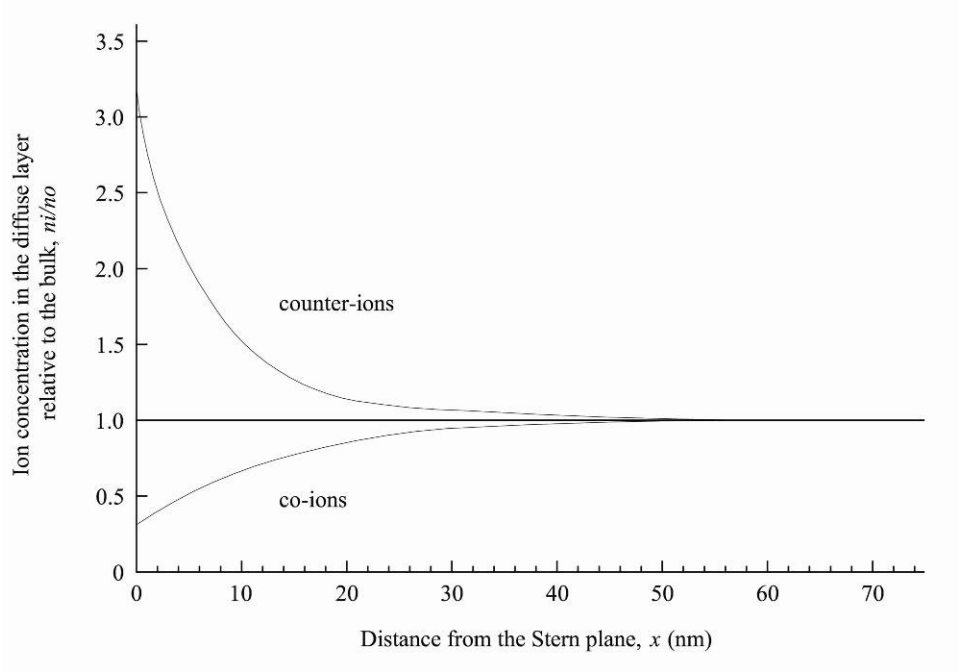

Figure 2-4. Graph of local ion concentration, n_i/n_o where n_i is the number of ions per unit volume in the bulk electrolyte n_o of 10^{-3} M NaCl. Surface potential is -30 mV.

The diffuse layer can be visualized as a charged atmosphere surrounding the colloid. The charge density at any distance from the surface is equal to the difference in concentration of positive and negative ions at that point. Charge density is greatest near the colloid and gradually diminishes toward unity as the concentration of positive and negative ions merge together. Within this diffuse layer the shear plane separates the mobile fluid from fluid that remains attached to the surface. The electric potential at this plane is called the electrokinetic potential or *zeta potential* (ζ). Although the position of the shear plane is not well defined (approximately three times the radius of a solvated ion), the zeta potential can be easily measured using electrokinetic techniques. The zeta potential can be used to evaluate the stern potential, assuming that approximately $\zeta \approx \psi_\sigma$.

In any medium containing free charges (for example water containing free ions in solution) all electrostatic fields become screened due to the polarization (displacement) of these charges. A screened electric field decays approximately exponentially with distance x according to $e^{-\kappa x}$ where κ is the Debye-Hückel parameter which is measured in length^{-1} (Equation 2-5). The Debye-Hückel parameter characterises the decay of the potential with the distance from the surface. The Debye screening length (κ^{-1}) is a term used to describe the characteristic length or "thickness" of the electrical double layer.

$$\kappa = \left(\frac{\sum_i \rho_{\infty i} e^2 z_i^2}{\varepsilon_0 \varepsilon \, k_B T} \right)^{\frac{1}{2}} \qquad \textbf{2-5}$$

where $\rho_{\infty i}$ is the ionic concentration of ions i in the bulk, e is the electronic charge constant and z_i is the valency of ion i. It is interesting to note that, other than some fundamental constants, the Debye length depends only on the temperature and the bulk electrolyte concentration. As such Debye lengths for known electrolyte concentrations can be quickly evaluated, for example, the Debye length of NaCl at 25°C is $1/\kappa = 0.304/\sqrt{[\text{NaCl}]}$ nm where [NaCl] is the molecular concentration of the electrolyte, in this case sodium chloride. At low surface potentials (<25 mV) the

potential of the EDL becomes proportional to the surface change density, and can be calculated as a function of the distance away from the stern layer as $\psi(x) \approx \psi_\sigma e^{-\kappa x}$.

2.2.3. DLVO Theory

Colloidal particle-particle interactions are described using the Derjaguin-Landau-Verwey-Overbeek (DLVO) [7] theory. The DLVO model combines the basic forces governing colloidal particles in suspension and it is primarily based on the relationships of long range repulsive electrostatic forces and short range attractive forces from the van der Waals interactions.

The stability of a particle in solution is dependent upon its total potential energy function V_T. DLVO theory assumes that V_T is the balance of two competing contributions:

$$V_T = V_A + V_R \qquad \textbf{2-6}$$

where V_A is the non-retarded van der Waals attractive potential and V_R the electrical double layer repulsive potential. The attractive potential energy related to van der Waals force interactions as the separation distance, D, between spherical particles of radius R changes is given in Equation 2-7.

$$V_A = -\frac{AR}{12D} \qquad \textbf{2-7}$$

The repulsive potential V_R (Equation 2-8) becomes significant when two colloids approach each other and their double layers begin to interfere. It has a maximum value when they are almost touching and decreases to zero outside the electrical double layer.

$$V_R = \left(\frac{64\pi k_B T R \rho_\infty \gamma^2}{\kappa^2} \right) e^{-\kappa D} \qquad \textbf{2-8}$$

where ρ_∞ is the electrolyte concentration in the bulk, $\gamma = \tanh(ze\psi_0/4k_BT)$.

DLVO theory allows evaluations of the stability of a colloidal system to be determined by the sum of these attractive and repulsive forces that exist between particles as they interact with each other. Figure 2-5 represents a system with a primary minimum and primary maximum in the total interaction energy potential. The primary minimum is where the attractive interactions dominate over the repulsive interactions and, conversely, the primary maximum is where the repulsive interactions dominate over the attractive interactions. We see that in order to reach the primary minimum the particles must exceed the primary maximum activation energy. Therefore if $V_T^{MAX} >> k_B T$ the particles will be in a stable colloidal state.

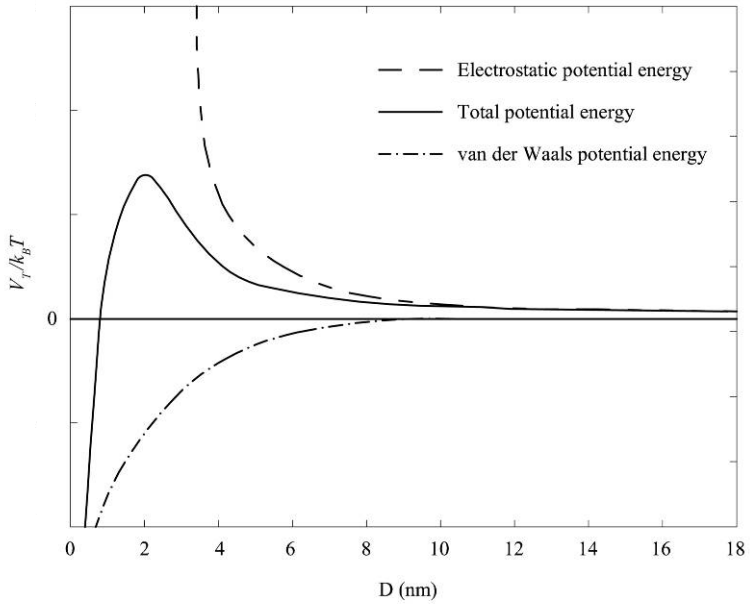

Figure 2-5. A Schematic diagram of the DLVO theory showing variation of total system energy with particle separation distance, D. The total potential energy is given by the sum of the double layer repulsive and the van der Waals attractive interaction energies that the particles experience as they approach one another.

In certain situations (e.g. high electrolyte concentrations decreases the Debye length, effectively reducing the extent and intensity of the repulsive electrostatic interactions between the colloidal particles), there is a possibility of a secondary minimum where a much weaker and potentially reversible aggregation between particles exists (Figure 2-6). At the secondary minimum $-V_T^{SMIN} \sim k_B T$ so the net attractive energy is at best only slightly larger than the average thermal energy. The result of this is the

formation of weak flocs, sufficiently stable not to be broken up by Brownian motion, but may dissociate under an externally applied force such as vigorous agitation.

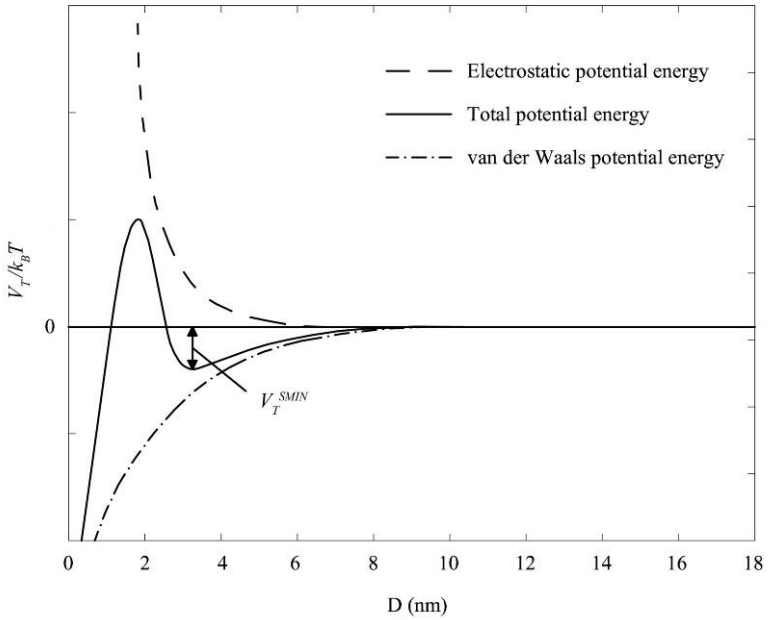

Figure 2-6. A Schematic diagram of the DLVO theory showing variation of total system energy with particle separation distance, D. In this case the compressed EDL has created a secondary minimum to the total potential energy referred to at V_T^{SMIN}.

More recently the standard DLVO model has been updated to incorporate the short-range Lewis acid–base (AB) interactions that account for electron acceptor/electron donor interactions which have a measurable effect within a few nm of separation distance. The extended DLVO or XDLVO theory also can encompass other non-DLVO interactions arising from solvation forces in aqueous systems, in particular hydration forces [8] due to the energy required to disrupt the hydrogen-bonding network formed by the binding of water molecules to hydrophilic surfaces and structuring. The hydration force is an oscillating repulsive force of periodicity roughly equal to the diameter of a water molecule that grows exponentially in magnitude. In the case of silica and mica it is believed to arise from strongly H-bonding surface groups such as hydrated ions or hydroxyl groups, which leads to the modification of the H-bonding network of liquid water adjacent to them.

2.2.4. Steric Interactions

As previously mentioned, in order to maintain the stable dispersed colloidal system, the repulsive forces must be dominant ($V_T^{MAX} >> k_B T$). To achieve an effective repulsive force without the use of electrostatic potentials, steric repulsion potentials can be utilized.

For colloidal stability the use of steric repulsion involves the application of a thermally diffuse interface of chain molecules (oligmer or polymer) attached at some point to the surface of the colloid dangling out into the solution where they are thermally mobile. On approach of an analogous colloidal particle the entropy of confining these dangling chains results in a repulsive entropic force referred to as the "steric" or "overlap" repulsion (Figure 2-7). This allows colloidal particles suspended in a non-polar medium to be stabilised against coagulation by the addition of a suitable polymer to the system adsorbing onto the colloidal particle surface and physically preventing the particle surfaces coming into close enough contact for attractive London - van der Waals forces to cause coagulation. Unlike electrostatic stabilization, there are no long range repulsive forces and the particles could be subject to attractive forces until the outer portions of the steric molecules contact each other. The magnitude of the repulsion depends on the molecular weight of the polymer chain, the coverage of the polymer on the surface of the colloid, the mechanism by which the polymer is attached to the surface (adsorbed or end grafted) and the quality of the solvent (i.e. if the polymer is in a poor solvent will coil up and shrink).

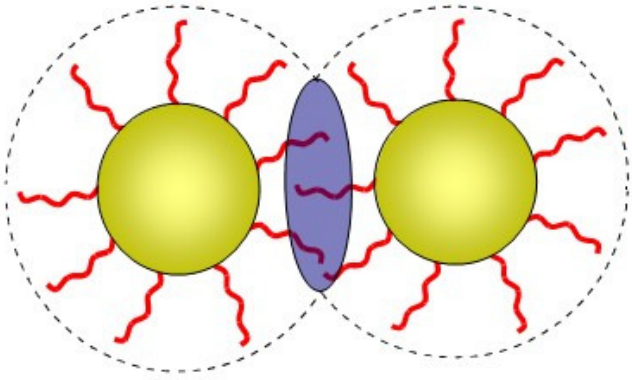

Figure 2-7. Diagram of steric repulsion between two colloidal particles.

2.3. Properties of Silica and Mica

Silica nanoparticles are mainly produced using two processes; fuming [9] and the Stöber sol-gel process [10, 11]. While fumed silica provides higher production rates in quantities of nanoparticles, the Stöber production process has been subject to much research and now represents a production method that has been fine tuned and offers the opportunity for tailoring the silica nanoparticles surface chemistry [12, 13]. When suspended in water, silica particles have a native negative charge on the surface due to the dissociation of silanol groups (Figure 2-8) which allow them to maintain an even dispersion in favourable pH levels and avoid coagulation without the need for surface chemistry modification.

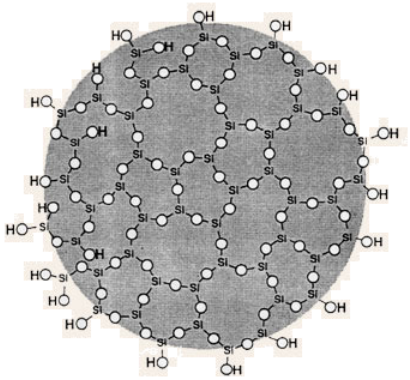

$$SiOH \text{ — } SiO^- + H^+$$

Figure 2-8. Illustration of silica colloid with hydroxyl groups at the surface in its raw state and the chemical mechanism by which these groups are ionised leading to a negative surface charge. Image taken from Silco International Technical Information media.

Mica is a group of sheet silicate (phyllosilicate) minerals that feature highly perfect basal cleavage, due to the hexagonal sheet-like arrangement of its atoms (Figure 2-9). This property provides us with an easy to prepare, atomically flat substrate. For our experiments we will be using muscovite, $KAl_2Si_3AlO_{10}(OH,F)_2$, a high-aluminium mica. Upon cleavage along the basal plane, the exposed surface of the mica is a highly hydrophilic, negatively charged surface due to the non-equilibrium

distribution of potassium ions across the cleaved surface, which reduces in time due to the attraction of oppositely charged contaminations.

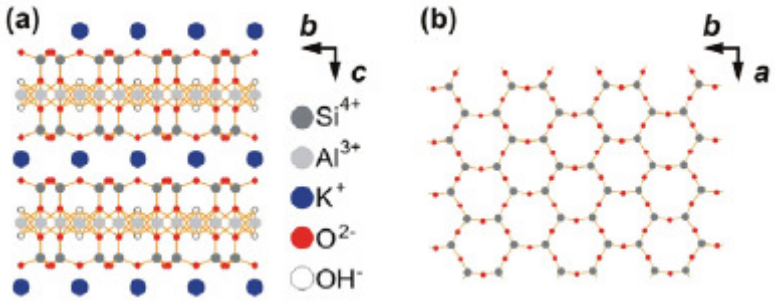

Figure 2-9. Schematic representation of the muscovite mica crystal structure. Vectors *a* and *b* define the [001] planes, vector *c* is the surface normal vector. (a) Side-view (projection onto the *a*-axis) exhibiting aluminosilicate layers separated by electrostatically bound interlayer potassium ions. (b) Hexagonal arrangement of the [001] surface top layer (projection onto the *c*-axis) exhibiting Si and O atoms of a cleaved mica surface, residual potassium ions are not displayed. Taken from Ostendorf *et al.* [14]

2.4. Self Assembly Mechanisms

2.4.1. Colloidal Self Assembly Techniques

Self assembly of colloids is an area of colloidal research that has immense impact in the industrial sector having numerous applications in the photonics [15], electronics [16], material sciences [17] and biological applications [18]. It is a term used to describe the ordering of systems into structures or forms without external assistance. These structures can be formed by the initial input of some energy (static systems), by the cyclical balance of chemical reactions that are initiated and eventually dissipate (dynamic) or due to pre-patterning of the underlying substrate to facilitate a desired structure (templated). Table 2-2 gives a brief overview of some of the systems that self assembly is used in, the types of self assembly used and its application or importance in industry/science.

System	Type	Applications/importance
Atomic, ionic, and molecular crystals	S	Materials, optoelectronics
Phase-separated and ionic layered polymers	S	
Self-assembled monolayers (SAMs)	S, T	Microfabrication, sensors, nanoelectronics
Lipid bilayers and black lipid films	S	Biomembranes, emulsions
Liquid crystals	S	Displays
Colloidal crystals	S	Band gap materials, molecular sieves
Bubble rafts	S	Models of crack propagation
Macro- and mesoscopic structures (MESA)	S or D, T	Electronic circuits
Fluidic self-assembly	S, T	Microfabrication

Table 2-2. Examples of self-assembly (S, static, D, dynamic, T, templated). Table taken from Whitesides and Grzybowski [19]

The forces that drive self assembly are the same forces that govern the behaviour of colloidal particles, covalent, electrostatic, van der Waals and steric forces and in addition some other forces such as capillary forces. In dried samples, that is, samples that involve the evaporation of the suspension, capillary forces play a major role in the final structuring of the colloidal particles (it should be noted that capillary forces can exist within liquid systems in the form of a gas bridge between two particles). Capillary forces have been shown to be responsible for particle ordering [20]

whereas the forces defined by the DVLO theory that govern colloidal interactions like electrostatic and van der Waals facilitate particle mobility within the suspension and substrate interactions during the assembly, but their influence on the final structure is not as pronounced [21].

2.4.2. Electrolyte Concentration Control over Particle Interactions

Due to the dependence of the Debye length on the ion concentration of the suspension, modification of the electrolyte concentration can provide us with a mechanism by which we can directly control the colloidal particle interactions. As attractive van der Waals forces are dependent only on the separation of the particles/surfaces, at low electrolyte concentrations when Debye screening is minimal, long-range repulsions severely limit the extent of adsorption due to the extended double-layer of ions surrounding it [22]. At higher electrolyte concentrations, the reduction in the Debye length causes the distance over which effective interparticle and particle-surface repulsions occur to be reduced. This suppression of the effective range of the repulsive force allows particles to approach one another and other surfaces at closer ranges, facilitating more densely packed arrangements, thus attaining higher surface coverage per unit area [23].

2.4.3. The Effects of Brownian motion and Particle Size

Colloids in liquid suspension also undergo random displacement due to their bombardment by solvent molecules which exert impulsive, stochastic forces. The thermal energy dictates the magnitude of these stochastic forces. In colloidal science the Brownian motion for a spherical particle much larger than the solvent molecules it is suspended in can be calculated by using the Stokes-Einstein diffusion relation, D_{SE}, shown in Equation 2-9.

$$D_{SE} = \frac{k_B T}{6\pi\eta R} \qquad \textbf{2-9}$$

where η is the solvent viscosity. Another important equation is the characteristic relaxation time, τ_R, which is the time it takes a particles to diffuse its own radius in an infinitely diluted system.

$$\tau_R = \frac{R^2}{6D_0} \qquad \textbf{2-10}$$

where D_0 is the diffusion coefficient associated with the particle at infinite dilution. Relating Equation 2-9 to Equation 2-10 and considering, T and η as fixed values for a particular system, we form a relationship between the relaxation time and particle size.

$$\tau_R \propto R^3 \qquad \textbf{2-11}$$

This proportional relationship clearly illustrates that particle size plays a major factor in the kinetic behaviour of the colloidal particle due to Brownian motion; with the larger particles having a lower diffusion rate than smaller particles which will diffuse rapidly for a given time frame.

2.4.4. Capillary Forces

Lateral capillary forces between colloids in thin films occur when the particles are partially immersed in the liquid layer; this immersion capillary force causes the liquid surface surrounding the particle to deform as the liquid wets the surface of the colloidal particle. As a liquid film evaporates its height from the substrate shrinks until any colloidal particles within the film protrude through it. When this happens, menisci form around the tops of the colloidal particles, generating an attractive force due to the deformation of the liquid surface and the induced asymmetry of the contact line at the surface of the particle. The magnitude of the force experienced between two neighbouring particles is dependent on several aspects including the separation distance of the particles, the radius of the three phase contact line and the

contact angle of the meniscus. The latter two are dependent on the particle size and liquid film height.

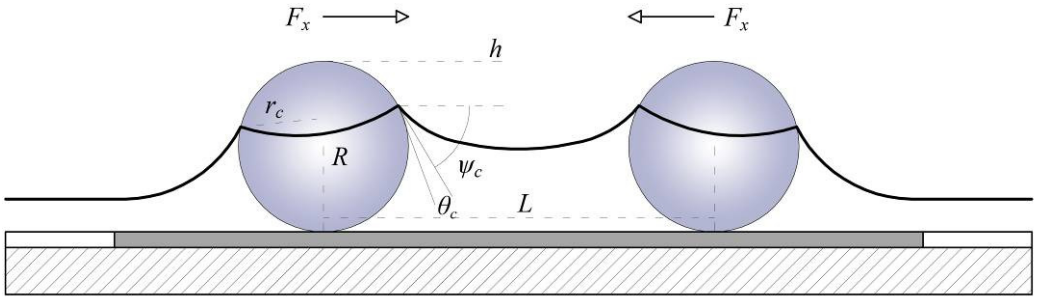

Figure 2-10. Two spheres partially immersed in a liquid layer on a horizontal solid substrate. The deformation of the liquid meniscus and the particle separation distance gives rise to interparticle attraction. Adapted from [24]

Figure 2-10 gives a schematic representation of two spheres of radius R on a surface under the influence of capillary force F_x which can be approximated [24] as:

$$F_x \approx 2\pi\sigma r_c^2(\sin^2\psi_c)(1/L) \qquad \textbf{2-12}$$

where σ is the surface tension of the liquid, r_c is the radius of the three-phase contact line at the particle surface ($r_c = [h(2R-h)]^{1/2}$), ψ_c is the mean meniscus slope angle at the contact line ($\psi_c = \arcsin(r_c/R) - \theta_c$, where θ_c is the contact angle of the bulk liquid), h is the height of the liquid layer from the top of the particle ($2R$), and L is the distance between the particles. It is clear from the equation that the radius of the particle R plays a dominant role in dictating the capillary force experienced between the colloidal particles. Also notice that force exerted by the menisci is proportional to the inverse of the distance between the neighbouring particles (L). This means that the further the neighbouring particles are apart when the menisci forms between them, the less force the capillary action exerts between them.

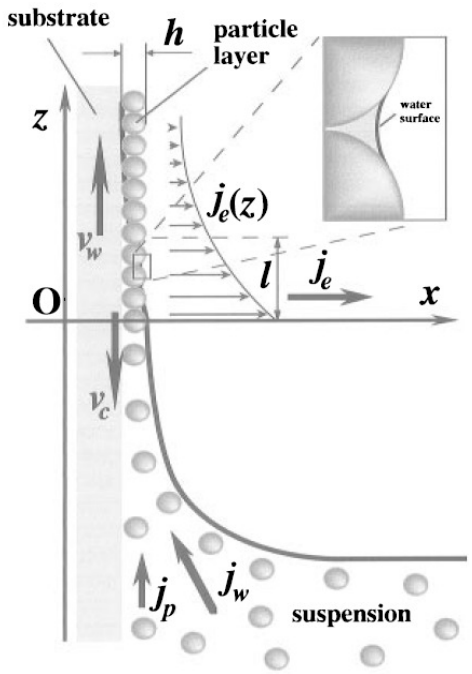

Figure 2-11. Sketch of the particle and water fluxes in the vicinity of monolayer particle arrays growing on a substrate plate that is being withdrawn from a suspension. The inset shows the menisci shape between neighbouring particles. Here, v_w is the substrate withdrawal rate, v_c is the array growth rate, j_w is the water influx, j_p is the respective particle influx, j_e is the water evaporation flux, and h is the thickness of the array. Taken from Dimitrov and Nagayama [20]

These capillary forces are the main driving force behind creating self assembled 2D colloidal crystals. These are self assembled regular patterns that may extend to areas of mm^2 and are of great interest to the photonics industry due to their Bragg diffraction properties [25]. Early techniques used for constructing 2D crystal films were simply droplets of the colloidal suspension evaporated onto a substrate. Refinement of this process came with the utilisation of the meniscus line in evaporating liquids and by the 1990s the mechanism and governing forces of the 2D particle assembly had been clarified [20]. A two stage process was observed:1) nucleus formation, under the action of attractive capillary immersion forces; and 2) crystal growth, through convective particle flux caused by the water evaporation from the already ordered array [25], as shown in Figure 2-11. Control over this capillary force comes from manipulation of the evaporation rate and the film meniscus. Dimitrov and Nagayama [20] demonstrated a now well established technique for creating tuneable 2D crystalline films using a setup akin to a dip coating device, where the substrate is submerged into the colloidal suspension then

withdrawn at a controlled rate. Other techniques include droplet application followed by tilting of the substrate [26], spin coating the colloidal suspension on the substrate [27] and the use of pre-patterned surfaces to create specific sites that are more energetically favourable to adsorb to. These techniques result in 2D crystalline films similar to those shown in Figure 2-12 where either multidomain or one large single domain crystal is grown.

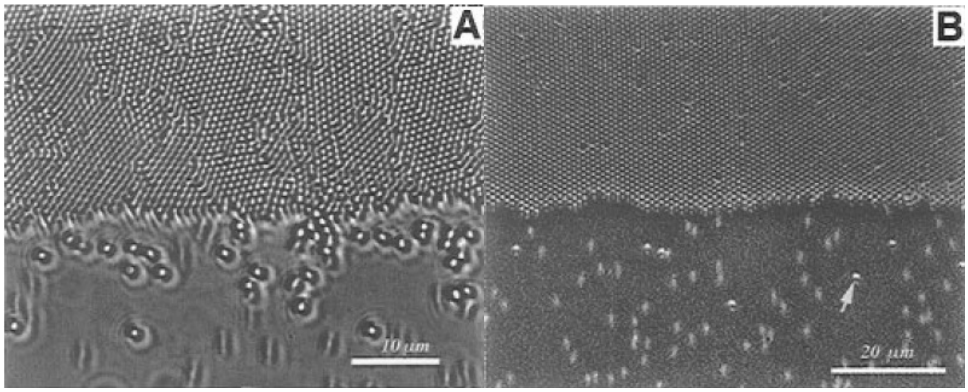

Figure 2-12. Part of the leading edge of a growing monolayer particle array. The upper-half of the photographs shows the formations of (A) differently oriented small domains of ordered 814-nm particles and (B) a single domain of ordered 953-nm particles. Taken from Dimitrov and Nagayama [20]

While the crystalline structuring of colloidal particles has typically been the domain of micrometer sized particles, research into the self assembly of nanometer sized colloids has yielded some radically different particle structuring, such as 2D cellular structures. These are normally associated with dewetting phenomena found in thin liquid films that undergo rupture and coalescence into structures seen in Figure 2-13. Martin and Moriarty [28] carried out studies linking this, normally fluid, behaviour to other systems including nanocolloidal suspensions of gold nanoparticles of a few nanometers in diameter. They found striking resemblances in morphology and using Voronoï tessellation to calculate the distribution of particles on the surface of the samples were able to assess the degree of (dis)order within a system by comparing these results with those from Poisson distributed simulations.

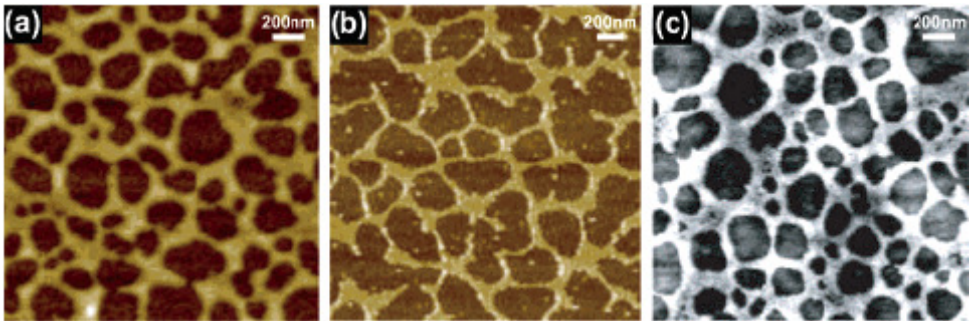

Figure 2-13. Three AFM images from experiments, showing (a) area of dewetted organometallic clusters, (b) Au nanoparticle networks on silicon, and (c) a polystyrene (PS) layer spin-coated from solution in toluene. Taken from Martin and Moriarty [28]

Rabani *et al.* [29] demonstrated a model for drying mediated self assembly of nanoparticles that simulates remarkably well the behaviour of these complex fluids by including not only the relatively weak attractions between the particles themselves but also the dynamics of an evaporating solvent. Using their model they were able to show that varying the choice of solvent, particle size and thermodynamic state gave rise to various morphologies.

2.4.5. Dewetting Phenomena

The dewetting phenomena can best be described with the analogy of a new car left in the rain. The water droplets on the waxed surface do not coat the bodywork evenly, rather they coalescence into droplets on the surface. In effect the rain water "dewets" on the car panels. Generally dewetting describes the rupture of a thin liquid film on the substrate (either a liquid itself, or a solid) and the subsequent formation of droplets.

Recent insights into the balance between short and long range forces involved in dewetting phenomena resulted in Sharma and Reiter [31, 32] presenting the following 4-stage dewetting process from experimental observations:

1. **Rupture of the thin film**
2. **Expansion and coalescence of holes to form polygonal "cellular" patterns**
3. **Fingering instability of hole rims during hole expansion witnessed only on low wettability surfaces (can also occur after stage 4)**
4. **Disintegration of liquid ridges forming the polygon into spherical drops due to Rayleigh instability**

Seemann, Herminghaus and Jacobs [33] provided a clarification of the distinction between stable, unstable and metastable films using the effective interface potential, $\Phi(h)$, which is defined as the excess free energy (per unit area) it takes to bring two interfaces from infinity to a certain distance, h. In the case of a dewetting film, the two interfaces involved are the solid/liquid interface and the liquid/air interface, and h is the initial thickness of the liquid film. By consequence $\Phi \rightarrow 0$ as $h \rightarrow \infty$ as shown in Figure 2-14. Curve 1 shows the scenario where $\Phi(h) > 0$ and the global minimum lies at infinite film thickness. In this case the liquid film is termed stable. Curve 2 shows the global minimum of $\Phi(h)$ occurring at a point h^*. When the free energy $\Phi(h)$ of the film possesses a negative curvature at the starting thickness, h_o, i.e. $\Phi''(h_o) < 0$, the system can gain energy by allowing the film thickness to reach h^*. If the initial film thickness is greater than h^* then the film will try to attain an equilibrium film thickness of h^* causing localised thinning in the film that will ultimately lead to rupturing and subsequent dewetting. Thus the portion of curve 2 in Figure 2-14 from infinity to h^* is termed unstable against *spinodal* dewetting. Spinodal Dewetting [34] is triggered by spontaneous amplification of capillary waves within the film caused by thermal fluctuations and is usually characterised by a bicontinuous structure of the phase separation morphology (Figure 2-15) which can be identified by 2D-FFT analysis of the morphology.

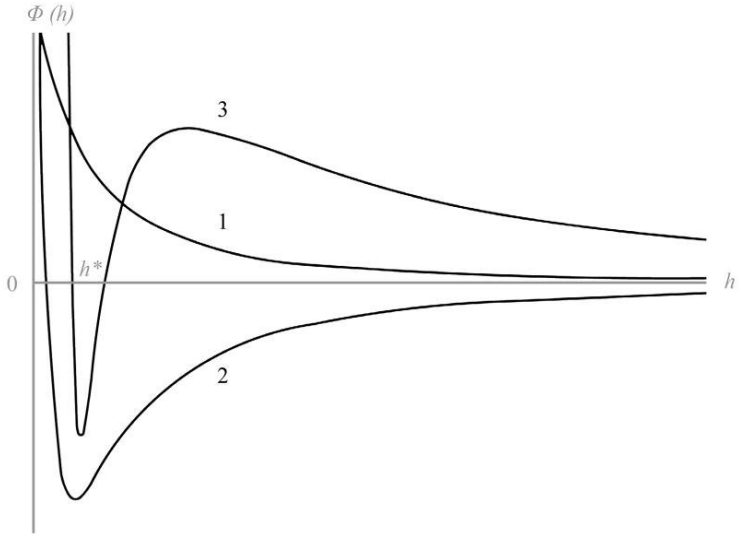

Figure 2-14. Shows the effective interface potential $\Phi(h)$ as a function of film thickness h for stable (1), unstable (2) and metastable (3)

Finally, curve 3 represents a system that is metastable; that is at low film thicknesses where $\Phi''(h_o) < 0$, spinodal dewetting can occur, but at larger film thicknesses it is stable against spinodal dewetting.

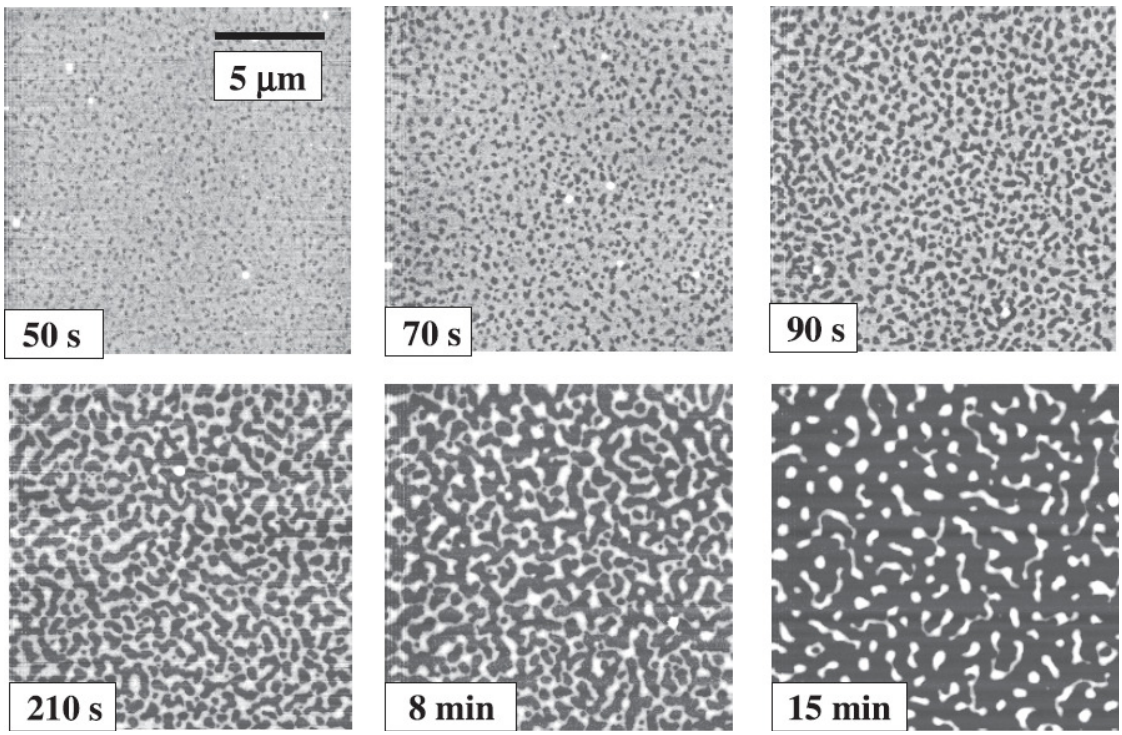

Figure 2-15. Spinodal dewetting occurring over a 15 minute period on a 3.2 nm PS film on silicon. Image taken from Seemann [33]

A second dewetting mechanism known as nucleation dewetting [35] can cause dewetting to occur on stable, metastable and unstable films either by nuclei defects such as dust particles/surface heterogeneities (heterogeneous) or by localised thermal instabilities (homogeneous). Nucleation dewetting can occur in parallel or at a different time frame to spinodal dewetting as the two processes are independent.

For heterogeneous nucleation (Figure 2-16), because the dewetting is initiated by surface defects the initial surface ruptures occur over a small time frame. Unlike spinodal dewetting however a characteristic length in the morphology does not exist. Homogeneous nucleation differs in that it has a continuous breakout of holes on the surface throughout the time frame, caused by the local fluctuations in thermal energy allowing the liquid to overcome the potential barrier for nucleation of a dry spot, leading to the formation of a hole. Also note that the time difference between full dewetting of the film via spinodal and nucleation mechanisms is in the order of magnitude.

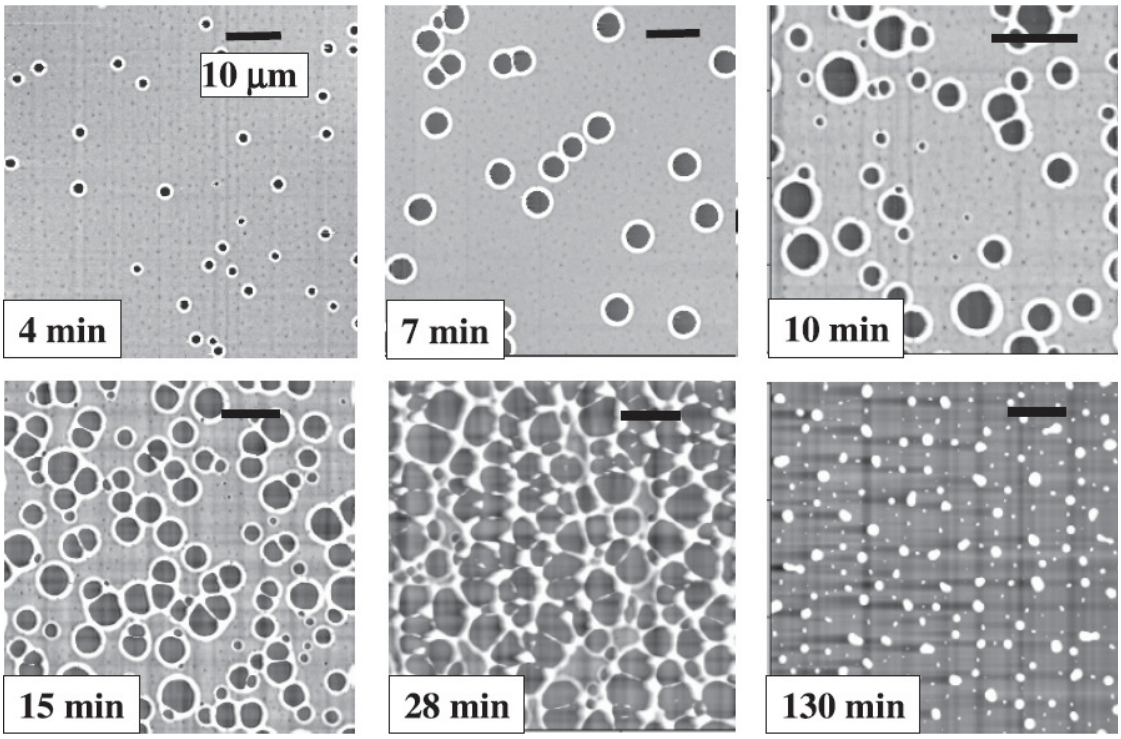

Figure 2-16. Heterogeneous nucleation dewetting occurring over a 130 minute period on a 12.8 nm PS film on silicon. Image taken from Seemann [33]

In Figure 2-17 a 2D-FFT of the spinodal dewetting image has been included to show the spatial correlation of the holes. The scale bar shows the "dimensional difference" between the different dewetting mechanisms.

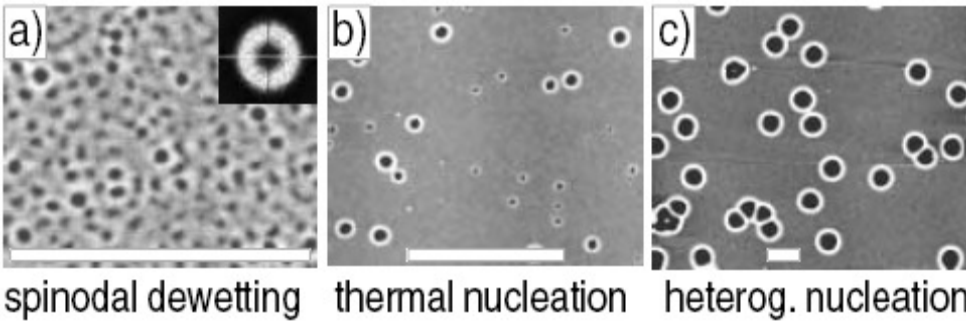

Figure 2-17. Shows AFM images of dewetting PS films of different thicknesses on different substrates. Scale bar represents 5 µm. Image taken from Seemann [33]

2.5. Atomic Force Microscopy

The atomic force microscope was first reported by Binnig, Quate and Gerber [36] of IBM in 1986 and followed on from their work on scanning tunnelling microscopy (STM) [37], for which they were awarded the Nobel Prize for Physics. It was suggested as a means of studying non-conducting surfaces on an atomic scale, combining the principles of the STM and a stylus profilometer, and imaging by effectively "feeling" the sample surface.

The major components of a modern AFM are given in Figure 2-18. The most important part is the tip, which makes the physical contact with the surface of the sample. The tip is usually made of silicon or silicon nitride, which is harder and hence more wear resistant. Typically tips have a micrometer scale pyramidal shape with a nanometer size apex radius. The tip is connected to a cantilever which allows the tip to move in relation to the topography of the sample. A laser beam is directed onto the backside of the cantilever at the tip end and its reflection is directed onto a photodiode detector with four quadrants. The intensity of light in each quadrant gives information on the position of the cantilever and hence the tip. This information is then sent to a controller where a feedback mechanism registers a deflection of the cantilever and manipulates the displacement between the tip and the sample so that the deflection is constant. This is achieved by using piezoelectric crystals which can be utilised either as the sample stage or, in the case of our schematic, as the cantilever mount. When a voltage is applied across it, a controlled expansion/contraction occurs in the piezoelectric crystal. This motion is very reproducible and precise and allows the crystal to be deformed with the accuracy of atomic dimensions, giving an AFM the ability to perform very precise measurements of the sample topography. An image of the sample is achieved by raster scanning i.e. scanning line by line in the X and Y directions (again by using piezoelectric crystals to control the movement). The Z height data is calculated by taking the varying voltage applied to the Z axis piezoelectric crystal to maintain a constant deflection and scaling it with the known calibrated ratio of voltage to distance of the piezoelectric crystal.

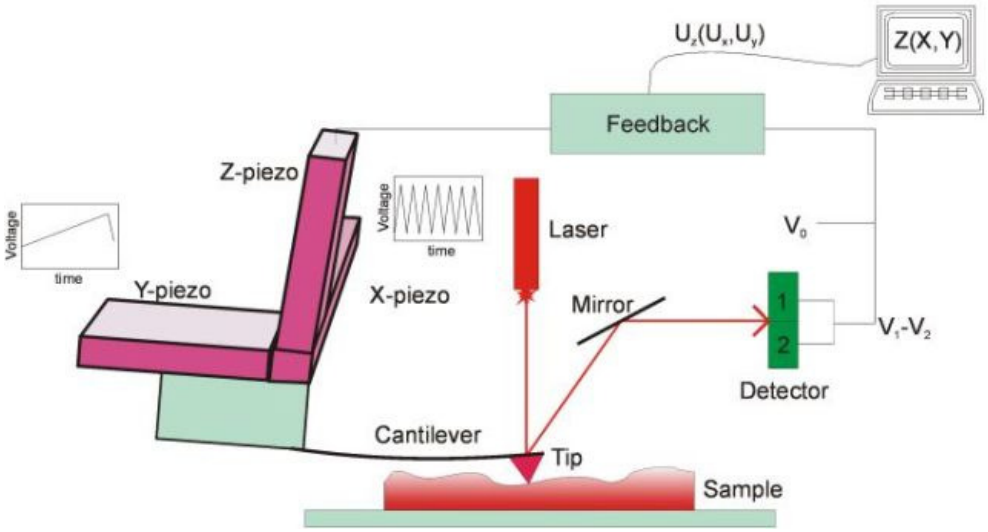

Figure 2-18. Schematic diagram of an atomic force microscope.

This mode of operation is referred to as contact mode AFM: the cantilever/tip is maintained at a constant deflection and moved along the surface. This is one of the simplest methods of imaging using AFM techniques, however is has several drawbacks. The tip can exert considerable force on the sample surface. For soft samples such as polymers or biological specimens, the tip-force may cause an irreversible deformation of the surface so that the topography information becomes ambiguous or inaccurate. Similarly the frictional and lateral forces generated by the dragging of the tip also have a large magnitude. As such any weakly adsorbed material on the substrate will simply be dragged along the surface, rendering contact mode ineffective for the imaging of delicate samples. To overcome such difficulties, it was suggested in 1987 that a non-contact (NC) mode [38] could be employed whereby the tip is not in constant contact with the surface but rather vibrates near the surface at its resonance frequency.

Intermittent contact (IC) mode AFM, also known as Tapping mode™ was introduced in 1993 and differs only slightly from NC mode in that at the extreme of each oscillation the tip touches the surface very briefly. As the tip is brought close to the sample surface in IC mode, the characteristics of the cantilever vibration (e.g. amplitude, resonance frequency) change due to the tip-sample interaction and the feedback mechanism adjusts the tip-sample separation in order to maintain a constant

amplitude of vibration. A recent development of tapping mode AFM gives the ability to detect shifts in phase angles of vibration when the oscillating cantilever interacts with the sample surface. The detection of phase angle shifts provides enhanced image contrasts for heterogeneous surfaces.

Given the size of the particles to be imaged in the present study, one of the most important AFM artefact effects to consider is tip convolution. This occurs due to the shape and the finite sharpness of the tip. At the nanometer scale the tip shape can be approximated by an effective tip radius R_{TIP}. The conical or pyramid shape of a tip means that the side of the tip will make physical contact before the tip end, resulting in the imaged particle appearing wider than it really is, as shown in Figure 2-19.

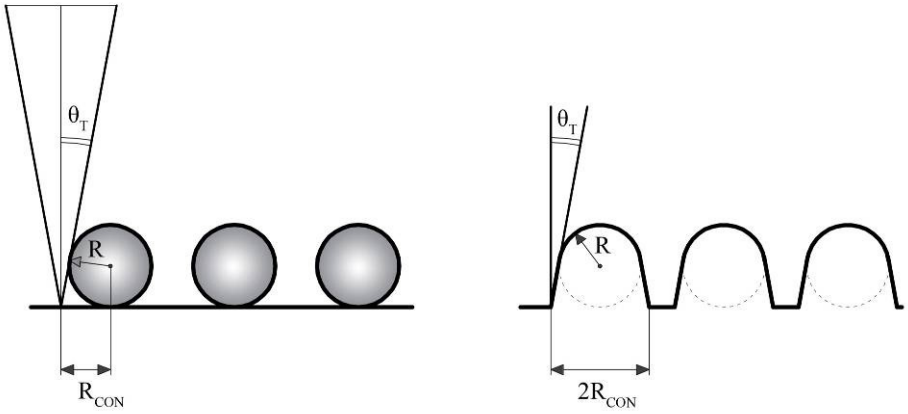

Figure 2-19. Schematic of the physical interaction between the conical AFM tip and the surface topography, and the resultant image profile in the case of $R_{TIP} << R$.

In the case where the tip radius R_{TIP} is much smaller than the feature curvature radius R we observe that the apparent object lateral width becomes $2R_{CON}$, from Equation 2-13, where θ is the cone half angle.

$$R_{CON} = R\left(\cos\theta + \sqrt{\cos^2\theta + (1+\sin\theta)\left(-1+\frac{\tan\theta}{\cos\theta}\right) + \tan^2\theta}\right) \qquad \textbf{2-13}$$

The corresponding surface profile imaged in these conditions results in the topography of the feature being broadened by $2(R_{CON}–R)$ while the apparent height, $2R$, will be accurately measured.

In the case where the tip radius R_{TIP} is approximately equivalent to the feature curvature radius R (Figure 2-20) we see that the both the lateral width and apparent topography height for particles with a spacing smaller than $2R_{TIP}$ have been skewed.

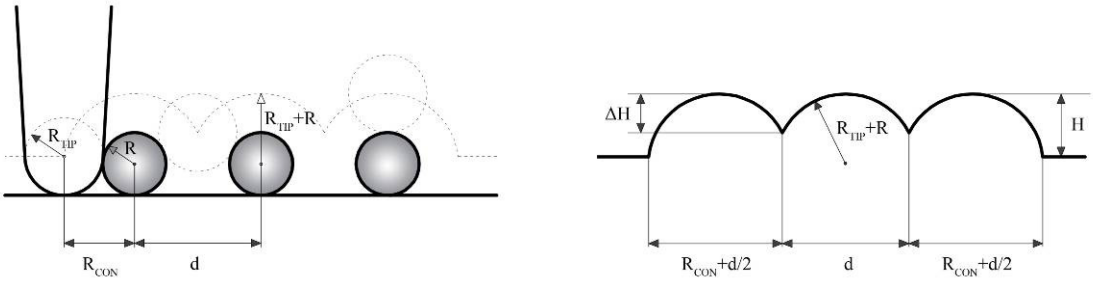

Figure 2-20. Schematic of the physical interaction between the conical AFM tip and the surface topography, and the resultant image profile in the case of $R_{TIP} \approx R$. The dotted line represents the tip trajectory as to tracks across the surface topography.

The apparent curvature of the particles is now $R_{TIP}+R$, and the apparent lateral width varying between d for enclosed particles and $R_{CON}+d/2$ for particles at the extremities; where R_{CON} is given by Equation 2-14

$$R_{CON} = 2\sqrt{R_{TIP}R} \qquad \textbf{2-14}$$

If the minimum distance between features $d–2R$ is less than the tip diameter $2\ R_{TIP} > d-2R$, then during the tip passing between them, it will penetrate as deep as ΔH as given in Equation 2-15. This is an important consideration, as a finite tip size means that it may not always be able to penetrate into the recesses of the topography accurately.

$$\Delta H = R\left(1-\sqrt{1-\frac{(d/2)^2}{(R_{TIP}+R)^2}}\right) \qquad \textbf{2-15}$$

These theoretical examples stress the importance of accurately matching the tip size to the topography of the sample. While we expect that some degree of blunting will occur throughout our experiments we endeavour to use clean, sharp tips for each set of experiments in order to avoid excessive convolution of the images that can be avoided if possible.

2.6. References

[1] B. G. Y. Xia, Y. Yin, Y. Lu, Advanced Materials 12 (2000) 693-713.
[2] Z. Adamczyk, Particles at Interfaces, Volume 9: Interactions, Deposition, Structure, Academic Press, 2006.
[3] D. H. Everett, Basic Principles of Colloid Science, 1988.
[4] J. Goodwin, Colloids and Interfaces with Surfactants and Polymers: An Introduction, 2004.
[5] R. J. Hunter, Foundations of Colloid Science, Oxford University Press, 2001.
[6] J. N. Israelachvili, Intermolecular and surface forces, Academic Press, New York, 1992.
[7] B. Derjaguin, and Landau, LD, Acta Physicochim. (USSR) 14 (1941) 633-662.
[8] R. M. Pashley, Journal of Colloid and Interface Science 80 (1981) 153-162.
[9] S. E. Pratsinis, Progress in Energy and Combustion Science 24 (1998) 197-219.
[10] W. Stöber, A. Fink, E. Bohn, Journal of Colloid and Interface Science 26 (1968) 62-69.
[11] D. L. Green, J. S. Lin, Y. F. Lam, M. Z. C. Hu, D. W. Schaefer, M. T. Harris, Journal of Colloid and Interface Science 266 (2003) 346-358.
[12] T. I. Suratwala, M. L. Hanna, E. L. Miller, P. K. Whitman, I. M. Thomas, P. R. Ehrmann, R. S. Maxwell, A. K. Burnham, Journal of Non-Crystalline Solids 316 (2003) 349-363.
[13] M. Qhobosheane, S. Santra, P. Zhang, W. H. Tan, Analyst 126 (2001) 1274-1278.
[14] F. Ostendorf, C. Schmitz, S. Hirth, A. Kuhnle, J. J. Kolodziej, M. Reichling, Nanotechnology 19 (2008) 305705.
[15] B. Amir Parviz, D. Ryan, G. M. Whitesides, Advanced Packaging, IEEE Transactions on 26 (2003) 233-241.
[16] J. H. Fendler, Chemistry of Materials 13 (2001) 3196-3210.
[17] I. Soten, G. A. Ozin, Current Opinion in Colloid & Interface Science 4 (1999) 325-337.
[18] S. G. Zhang, Nature Biotechnology 21 (2003) 1171-1178.
[19] G. M. Whitesides, B. Grzybowski, Science 295 (2002) 2418-2421.
[20] A. S. Dimitrov, K. Nagayama, Langmuir 12 (1996) 1303-1311.
[21] J. Aizenberg, P. V. Braun, P. Wiltzius, Physical Review Letters 84 (2000) 2997-3000.
[22] R. Rajagopalan, R. Q. Chu, Journal of Colloid and Interface Science 86 (1982) 299-317.
[23] C. A. Johnson, A. M. Lenhoff, Journal of Colloid and Interface Science 179 (1996) 587-599.
[24] N. D. Denkov, O. D. Velev, P. A. Kralchevsky, I. B. Ivanov, H. Yoshimura, K. Nagayama, Langmuir 8 (1992) 3183-3190.
[25] P. A. Kralchevsky, N. D. Denkov, Current Opinion in Colloid & Interface Science 6 (2001) 383-401.
[26] R. Micheletto, H. Fukuda, M. Ohtsu, Langmuir 11 (1995) 3333-3336.
[27] P. Jiang, T. Prasad, M. J. McFarland, V. L. Colvin, Applied Physics Letters 89 (2006) 011908-011903.

[28] C. P. Martin, M. O. Blunt, P. Moriarty, Nano Letters 4 (2004) 2389-2392.
[29] E. Rabani, D. R. Reichman, P. L. Geissler, L. E. Brus, Nature 426 (2003) 271-274.
[30] A. Vrij, J. T. Overbeek, Journal of the American Chemical Society 90 (1968) 3074–3078.
[31] A. Sharma, G. Reiter, Journal of Colloid and Interface Science 178 (1996) 383-399.
[32] A. Sharma, R. Verma, Langmuir 20 (2004) 10337-10345.
[33] R. Seemann, S. Herminghaus, K. Jacobs, Physical Review Letters 86 (2001) 5534-5537.
[34] R. Xie, A. Karim, J. F. Douglas, C. C. Han, R. A. Weiss, Physical Review Letters 81 (1998) 1251-1254.
[35] U. Thiele, M. G. Velarde, K. Neuffer, Physical Review Letters 87 (2001) 016104.
[36] G. Binnig, C. F. Quate, C. Gerber, Physical Review Letters 56 (1986) 930.
[37] G. Binnig, H. Rohrer, C. Gerber, E. Weibel, Physical Review Letters 50 (1983) 120.
[38] Y. Martin, C. C. Williams, H. K. Wickramasinghe, Journal of Applied Physics 61 (1987) 4723-4729.

Chapter 3: Silica Nanoparticles on Mica – Adsorption and Drying Effects

3.1. Abstract

We used dip-coating and droplet evaporation methodologies of silica colloid suspensions to adsorb and deposit silica nanoparticles on mica surfaces. The samples were imaged by atomic force microscopy in intermittent contact mode. This system allowed us to investigate the role of capillary forces and particle mobility on the self-organisation process and structuring of nanoparticles on surfaces. We observed the formation of close-packed nanoparticle chains and monolayer islands that grew in lateral size, reaching a continuous cellular network and ultimately approaching total coverage of the substrate with increasing colloidal concentration. Our findings point towards irreversible adsorption of the nanoparticles but with weak surface interactions facilitating lateral mobility of the adsorbed nanoparticles. Fractional surface coverage measurements show a dependence of the particle adsorption density on the colloidal suspension volume fraction. This was attributed to compression of the Debye length due to the affect of high volume fraction of nanocolloidal macro-ions having a similar effect to increases in electrolyte concentration. Lateral mobility during adsorption was confirmed by the existence of fractional surface coverage values for the highest volume fractions that were greater than the theoretical jamming limit for two-dimensional random sequential adsorption of monodisperse hard spheres, suggesting that particles in our system were able to reconfigure on the surface to enhance particle density. Lateral capillary energies were evaluated and a critical minimum particle separation distance to ensure that self assembly would occur between neighbouring particles was established. This value was found to be in good agreement with previous studies of similar systems. We also imaged partially dried samples which left an ultrathin film of the fluid on the mica surface. AFM topography and phase imaging revealed that the adsorbed nanoparticles were enveloped within the liquid and subjected to capillary and convective forces leading to close packed structures. Furthermore, we investigated thicker films deposited using droplet evaporation. The resulting formations showed predominantly amorphous configurations with some localised ordering due to the effects of evaporation kinetics and volume fraction changes during drying.

3.2. Introduction

Self assembled, highly ordered, ultrathin crystalline films of colloidal particles are of much research interest [1]. The ability to produce a thin film of highly ordered particles quickly from simple, economical materials has attracted much attention from various areas of industry. These include the semiconductor industry, where the pursuit of ever smaller chip die sizes requires the move from top-down to bottom-up fabrication [2, 3]; the production of photonic band gap materials [4] for the telecommunications industry; biomedical lab-on-a-chip devices and biosensors [5] which are also dependent on advances in nanometer scale structures. Colloidal silica particles with well-defined diameters (few nm to μm) can be manufactured at an industrial scale in large quantities. One advantage of using silica particles is that their native surface chemistry provides the necessary repulsive force to maintain colloidal dispersion by negative electrostatic charge [6] due to the dissociation of the exposed silanol groups in water. This provides a simple colloidal system for experimental investigations of self assembly and self organisation phenomena without the need for additional chemical alteration of the colloidal surface. Silica colloidal particles are mainly produced using two processes; fuming [7] and the Stöber sol-gel process [8, 9]. While fumed silica provides higher production rates in quantities of particles, the Stöber production process has been subject to extensive research and now represents a production method that has been fine tuned and offers the opportunity for additional functionalisation of the silica particles surface chemistry [10, 11].

While long range ordering of nanoparticles has been achieved by self-assembly at the liquid-air interface [12], long-range ordered structuring directly at the solid-liquid interface has been successful only for larger colloidal particles (closer to the micrometer scale) [13]. Self assembly [14] of particles at the solid-liquid interface has been investigated using different processes associated with gravitational [15], magnetic [16], convective [17] and hydrodynamic or capillary forces [18]. Capillary forces are induced by the formation of the liquid meniscus between neighbouring particles [17] generating an attractive force that draws them tightly together during the final stages of sample drying. This process facilitates the construction of ordered

monolayers of colloidal particles, which allows for more exotic structures when combined with templates or other methods of particle confinement [19].

Research into the behaviour of colloidal particles on solid surfaces is usually focused on investigations of their adsorption behaviour or the final structuring and patterns associated with drying effects. Regarding colloidal adsorption, Adamczyk *et al.* have conducted extensive studies of irreversible and strong adsorption of oppositely charged particles using a monodisperse colloidal system [20, 21]. These studies covered aspects including diffusion controlled adsorption kinetics [20] with both theoretical modelling using random sequential adsorption (RSA) and experimental aspects of the adsorption process. We note however that research on systems of particles and substrate with similar charge is sparse, with only a few systems having been investigated using rather irregular and polydisperse alumina grains on mica [22, 23]. Such systems were described as irreversible (i.e. no desorption) but with lateral mobility due to the weak adsorption of the particle to the substrate. A study of such enhanced lateral mobility systems especially at high surface coverage's is lacking in current literature. From the perspective of drying effects, the majority of research has been focused on the capillary force mechanism and its effect on particle structuring. Early studies of capillary forces used experimental setups that were reminiscent of the Langmuir-Blodgett technique, by depositing colloidal particles of micrometer size on a vertical substrate via convection and subsequent capillary forces [13, 18]. These studies led to the mathematical quantification of these interparticle capillary forces induced by the evaporating menisci [24, 25], laying the foundations for better understanding of drying effects. Simple dip coating is a well-established industrial process which has potential for applications in bottom-up nanomanufacturing [19, 26]. While the final structures of colloidal particles are usually attributed to hydrodynamic and capillary forces, direct observation of their effects during drying has not been accomplished and their connection to the adsorption process has not been determined. In order to achieve long range highly ordered monolayer assemblies of *nanocolloids*, it is important to understand further the interplay between nanoparticle surface *mobility* and *capillary forces* on the resulting nanostructures.

We present in this chapter the behaviour of colloidal silica nanoparticles adsorbed/deposited on mica substrates both by dip coating and droplet evaporation methods. We investigated the fine structure of the nanoparticle assemblies using atomic force microscopy (AFM) techniques. For the dip coated samples (the main objective of our study) we investigated how the lateral mobility of our system affects the fractional surface coverage and compare our findings with other systems where the particles are immobile after adsorption. We then explore the origins of the interconnecting network structure of chained colloidal silica nanoparticles that exhibited some ordering and expanded in width with increasing concentration until achieving high surface coverage of the substrate and relate this to the interplay of attractive lateral capillary forces, adsorption density and particle lateral mobility. We also took AFM snapshots of the actual process of drying mediated self assembly of the silica nanoparticles as they came under the influence of capillary forces of the ultrathin liquid film. To the best of our knowledge this is the first time that this is achieved. For the droplet coated samples we looked into thicker film formations and discuss the origins of the overall dense but mainly amorphous film structure of nanoparticles with patches of localised order.

3.3. Materials

The silica colloidal suspension was soured from Dr Andrew Schofield of Edinburgh University and prepared using the Stöber sol-gel process [9]; in which the hydrolysis and condensation of Tetraethyl orthosilicate (TEOS) forms silicon dioxide nanoparticles dispersed in an ethanol-ammonia solution [a ratio of 1 part 25% ammonia (diluted with water) to 10 parts ethanol]. The silica particles were evaluated in size to be approximately 120 nm in diameter using dynamic light scattering (DLS) techniques. The concentration of the original suspension was 600 g/L (volume fraction $\phi = 3.16\times10^{-1}$). We prepared 6 g/L ($\phi = 3.16\times10^{-3}$), 60 g/L ($\phi = 3.16\times10^{-2}$), 120 g/L ($\phi = 6.32\times10^{-2}$) and 300 g/L ($\phi = 1.58\times10^{-1}$) dilutions of the original colloidal suspension by volume fraction with ethanol-ammonia solution. The mica sheets used were sourced from Fisher (Leicestershire, United Kingdom). When submersed into the ethanol-ammonia solution, the surfaces of both the silica nanoparticles and the mica substrate have a negative charge. For the silica this is due to the dissociation of silanol groups in the presence of water, and for the mica a net negative charge is generated by the uneven charge distribution of potassium ions on the cleaved surfaces [27]. The particle ζ-potential was evaluated using a Malvern Zetasizer (Worcestershire, United Kingdom) and measured to be -45.9mV.

3.4. Experimental Methodology

The colloidal suspension was stored in a refrigerator at 4 °C to inhibit coagulation and sedimentation of colloidal particles while in storage. Samples for imaging were prepared in two different manners, dip coating and droplet evaporation. The mica (pre-cut 11 mm squares) was freshly cleaved using a scalpel along the lateral plane of the sheet. This procedure was carried out inside a fume cupboard to minimise airborne pollutants from contaminating the surface [28]. Before samples were prepared the colloidal suspension was agitated for 30 seconds to ensure even distribution of the colloidal density throughout the suspension.

Dip coated samples were prepared by placing the freshly cleaved mica into a vial of the colloidal suspension for a period of 30 minutes (kinetics studies have shown that this is sufficient time for maximum monolayer adsorption for each concentration used), fully submerged in an upright position with clean stainless steel forceps to minimise contamination of the colloidal suspension. The vial was placed at room temperature/pressure in a sealed box to avoid contamination from airborne particles. Once the required incubation time was up, the sample was removed and gently rinsed with a 10:1 ethanol:ammonia solution to remove any unabsorbed colloidal particles. This process was found not to affect the amount of adsorbed particles so adsorption of the silica nanoparticles can be considered irreversible. A nitrogen jet was used to dry any remaining ethanol:ammonia solution from the surface of the sample. Samples were then placed in a glass covered Petri dish and put in an oven for 1 hour at 60 °C to ensure that the sample was free of any traces of the solution. Samples were then either imaged immediately or sealed with parafilm until required. For a selection of samples, the nitrogen jet drying step was not exhaustive and the remaining ethanol:ammonia solution was partially removed. The surfaces were imaged immediately so that the thin films of the colloidal suspension could be examined before complete drying had occurred. These samples were subsequently dried as per normal and imaged immediately or sealed with parafilm until imaged later.

Droplet evaporation samples were created by applying 0.16 ml of the colloidal suspension from a pipette onto the freshly cleaved mica substrate, then placing this into a large drying box to avoid heterogeneous particles from contaminating the sample at room temperature/pressure. The colloidal suspension wetted the entire area the substrate and was pinned to the edges of the mica square creating a wetting film that became globally thinner while drying slowly. These were left until the suspension had evaporated (approximately 4-5 hours at room temperature), after which the sample was placed in a glass covered Petri dish and left in an oven for 1 hour at 60 °C to ensure the complete evaporation of any trace of ethanol:ammonia

solution. Samples were then imaged immediately or sealed with parafilm until imaged later.

3.5. Measurements

Imaging was done using a PicoSPM AFM (Agilent Technologies, CA, USA) operating in tapping mode (intermediate contact with the sample) using cantilevers (Mikromasch, Tallinn, Estonia) with a nominal spring constant and resonant frequency of 40 N/m and 170 kHz, respectively. Their nominal tip radius was quoted as 10 nm. We operated in a light tapping mode, where the contact amplitude approached the free oscillation amplitude of the cantilever, to minimise tip sample interaction forces. The cantilevers were oscillated at 5% below their natural resonance frequency. For post processing of the AFM images Scanning Probe Image Processor (SPIP, Image Metrology, Hørsholm, Denmark) was used. All images presented in this study were post-processed by simple flattening unless otherwise stated. The vast majority of the samples prepared have shown homogenous structures, apart from the clusters and structures at the fine nanometer scale and the images shown in this chapter are representative of the concentration of the colloidal suspension and conditions of sample preparation for every occasion unless otherwise stated.

3.6. Results

3.6.1. Dip Coating of Silica Colloidal Suspension on Mica

With the 6 g/L silica colloidal suspension, in the AFM image presented in Figure 3-1 we find a mixture of isolated particles, short chains and small clusters of particles covering the surface. Particle clusters are of a monolayer structure with tight packing evident and occasional hexagonal structuring in isolated areas. The height profile in Figure 3-1 shows that the measured particle height is approximately 80 – 90 nm, suggesting a particle diameter smaller than that estimated by the DLS. We suspect that this may be due to inaccurate measurements from the DLS measurements, where the colloidal suspension may not have been sufficiently diluted to achieve an accurate result. Due to convolution effects causing the broadening of the apparent particle area, the fractional surface coverage, θ, was calculated by counting particle numbers and multiplying by the colloidal 2D area (πR^2, R = 85 nm) and divided by the area of the corresponding image. This process was carried out for four images and averaged. The resultant fractional surface coverage for the 6 g/L ($\phi = 3.16\times10^{-3}$) samples is 0.16±0.03. A full list of fractional of surface coverages can be found in Table 3-1.

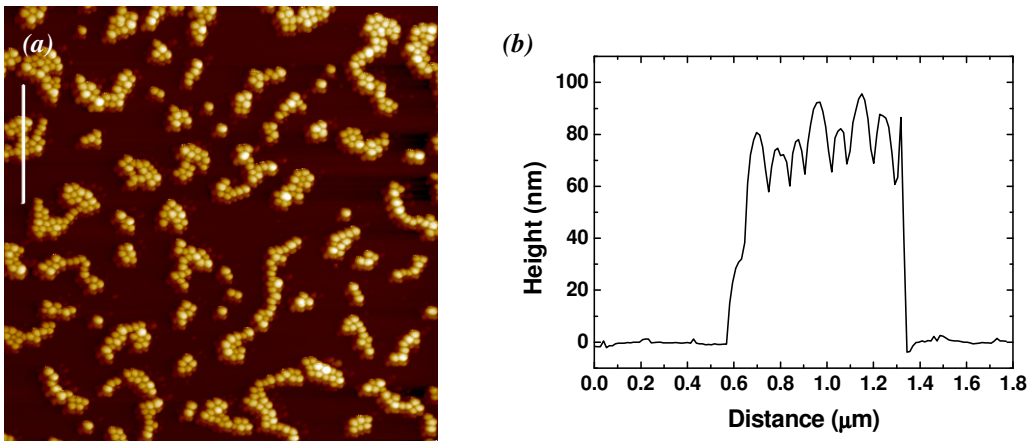

Figure 3-1. (a) 6.6 × 6. 6 μm^2 topography scan of silica particles; sample incubated for 30 minutes (concentration 6 g/L); (b) height profile corresponding to the white line on the topography.

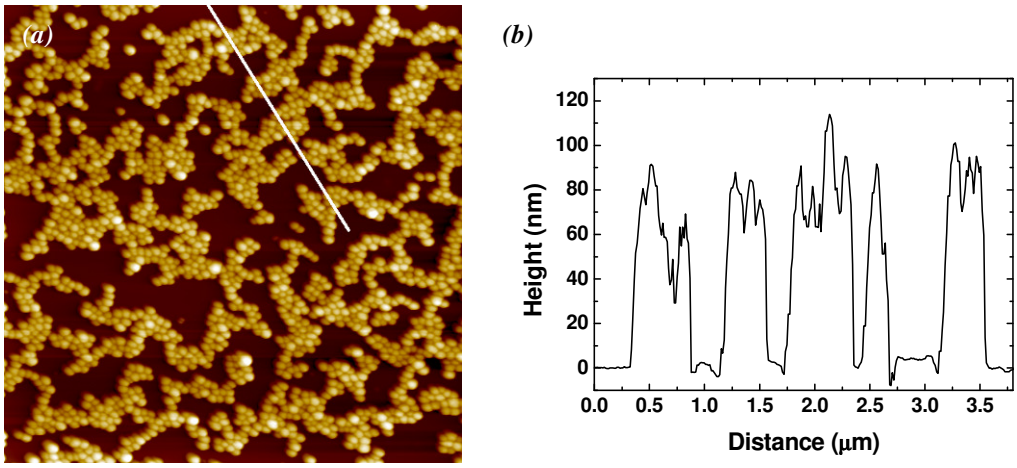

Figure 3-2. (a) 6.6 × 6.6 μm^2 topography scan of silica particles; sample incubated for 30 minutes (concentration 60 g/L); (b) height profile corresponding to the white line on the topography.

AFM results in Figure 3-2 correspond to the 60 g/L ($\phi = 3.16\times10^{-2}$)concentration of the colloidal suspension. The fraction surface coverage increased to 0.37±0.026 of the imaged area and the structuring of the particles has become more interconnected, with the emergence of wider particle chains and the occasional isolated particles. We also note that the particles still form tight close packed structures where particle number densities allow.

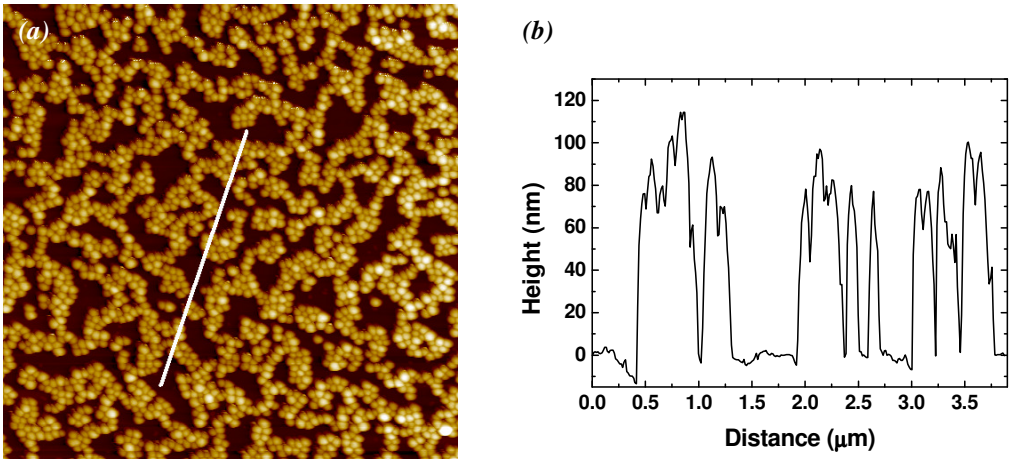

Figure 3-3. (a) 6.6 × 6.6 μm^2 topography scan of silica particles; sample incubated for 30 minutes (concentration 120 g/L); (b) height profile corresponding to the white line on the topography.

Figure 3-3 shows that with a 120 g/L ($\phi = 6.32\times10^{-2}$) colloidal suspension, we find the particle structures have begun to form an expansive interconnected network across the sample surface with the fractional surface coverage increasing to 0.46±0.023. The silica colloidal particles are still organised in a monolayer with close packed structuring apparent.

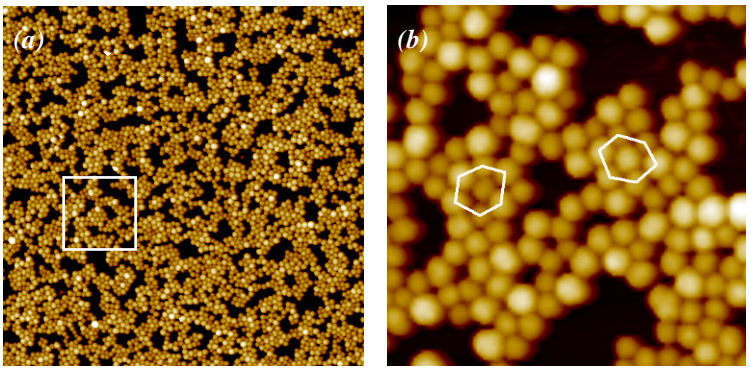

Figure 3-4. (a) 6.6 × 6.6 µm^2 topography scan of silica particles; sample incubated for 30 minutes (concentration 300 g/L); (b) zoom showing hexagonal structuring of the silica particles. Z range is 140 nm.

Figure 3-4 corresponding to the 300 g/L ($\phi = 1.58\times10^{-1}$) colloidal concentration shows that the silica particles are arranged in a dense network structure of high fractional surface coverage (0.52±0.019). Particles show a higher level of close packed configurations; hexagonal structuring becoming evident due to the increased amount of adsorbed material, as indicated on the zoomed image (Figure 3-4b).

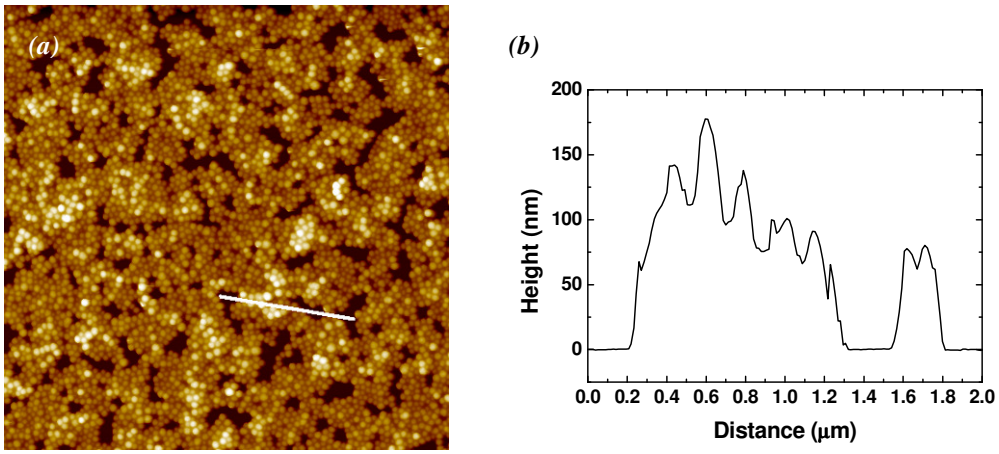

Figure 3-5. (a) 6.6 × 6.6 μm^2 topography scan of silica particles; sample incubated for 30 minutes (concentration 600 g/L); (b) height profile corresponding to the white line on the topography showing occasional particle bilayering.

Figure 3-5 shows the topography and height profile for an incubation time of 30 minutes of the undiluted 600 g/L ($\phi = 3.16\times10^{-1}$) colloidal suspension. We observe the structuring of the particles approaching a continuous film with some bilayer coverage, as shown in the height profile. The fractional surface coverage is 0.60±0.015.

3.6.2. AFM Snapshots during Drying

During the preparation of our samples, we were fortuitous enough to image a sample where incomplete drying of the sample surface had occurred, the results of which are shown in Figure 3-6. The topography image shows a smooth but ruptured thin (liquid) layer surrounding nanoparticle structures; the simultaneously taken phase image provides us with a much clearer visualisation of the nanoparticles still enveloped in the broken thin film of the suspension liquid.

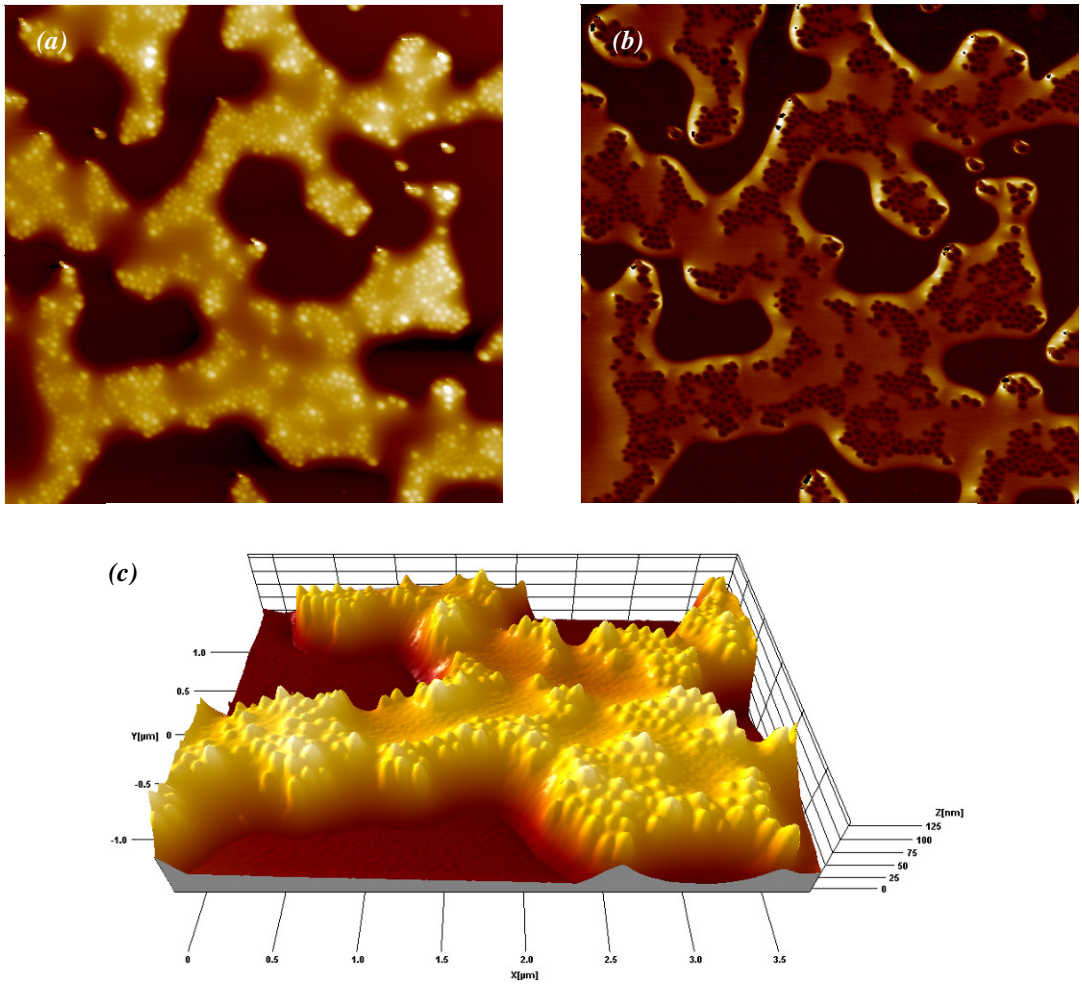

Figure 3-6. (a) 6.6 × 6.6 µm^2 topography scan (Z range is 150 nm) of nanoparticles still enveloped within the suspension liquid (incubation 30 minutes, concentration 120 g/L); (b) corresponding phase image accentuating the highly structured nature of the nanoparticles in the liquid film (phase voltage range ≈ 6.4 V). (c) 3D representation of the topography with xyz scale shown.

This is due to the enhanced contrast of phase imaging resulting from the differences in mechanical/adhesive properties of the silica nanoparticles and the surrounding medium [29, 30]. These images showed a system where the nanoparticles had begun to cluster into well defined close packed structures near the edge of the broken liquid film, with many exhibiting ordered (hexagonal) configurations. Height profiles of the particles (Figure 3-7b) suggest a diameter of approx. 85 nm, which is in agreement with previous height profiling of the particle diameter size in fully dried samples.

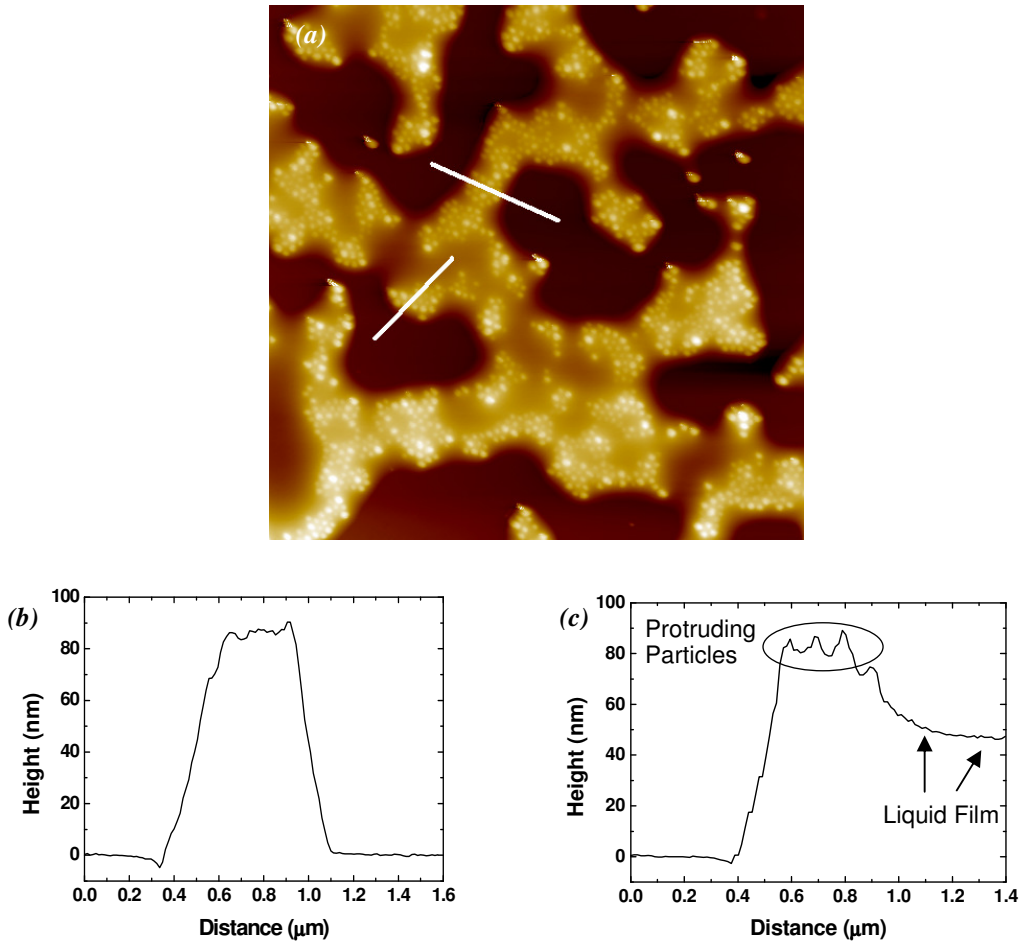

Figure 3-7. (a) 6.6 × 6.6 µm^2 topography scan of nanoparticles still enveloped within the suspension liquid (incubation 30 minutes, concentration 120 g/L), (b) height profile corresponding to the upper white line on the topography indicating the particle size and (c) height profile corresponding to the lower white line on the topography showing the difference in liquid film height and the particle height.

Height profiles of the liquid film at a distance from the particles, Figure 3-7c, show that its thickness is approximately 50 nm, and as such lower than the size of the

particles it surrounds. We see that at the immediate vicinity of the nanoparticles the liquid film thickness increases smoothly, with only the top of the particles protruding out of the liquid.

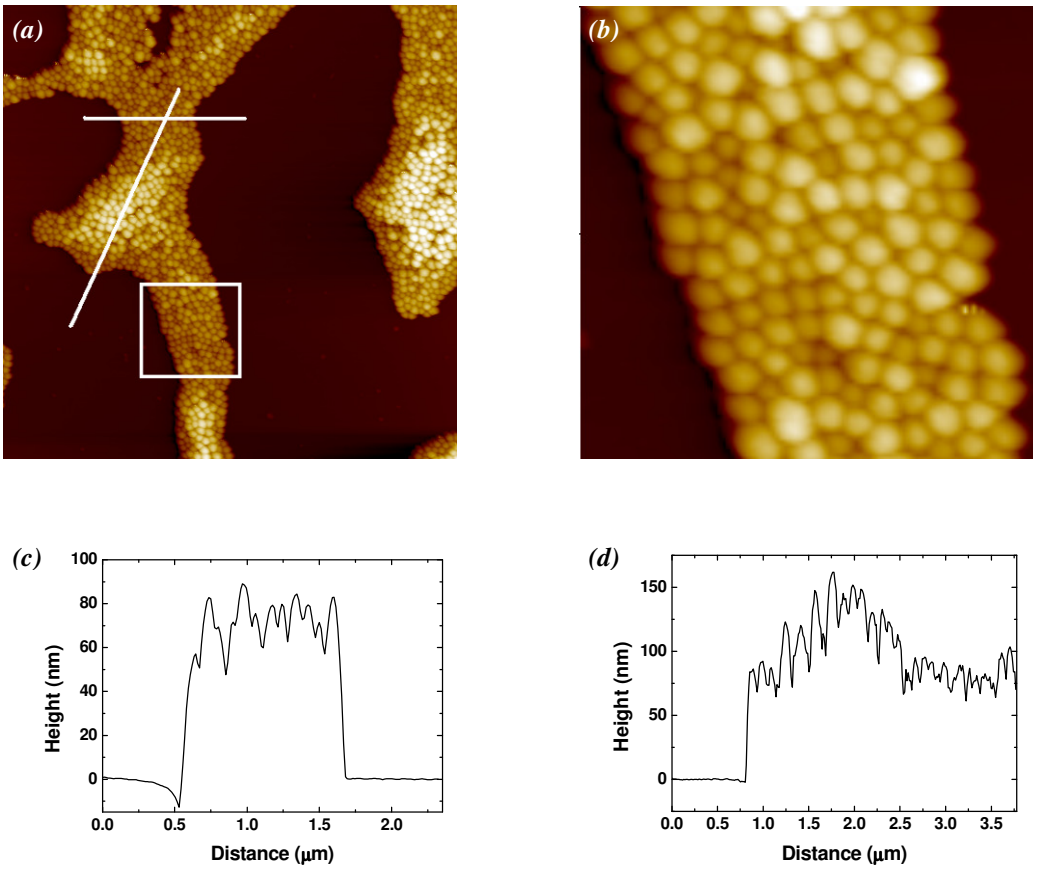

Figure 3-8. (a) 6.6 × 6.6 µm^2 topography scan of silica particles; sample incubated for 30 minutes (concentration 120 g/L); (b) zoomed section shows the close packed nature of the particles in more detail; (c) height profile corresponding to the upper white line on the topography shows that the particles are in a monolayer structure in this region; (d) height profile corresponding to the lower white line on the topography shows that the particles are in a bilayer structure in this region. Z range is 200 nm.

When partially dried samples were allowed to completely dry in accordance with the sample preparation methodology, the colloidal particles, rather than forming a well distributed monolayer network like that of Figure 3-3, have formed larger dense structures of the particles and large voids of empty mica substrate surrounding them (Figure 3-8a,b). Figure 3-8c shows a height profile of the close packed structure that suggests that the particles are in a monolayer configuration with a film height of

approximately 80-90 nm. We also see evidence of some bilayering in other regions of the sample image (Figure 3-8d).

3.6.3. Fractional Surface Coverage Results

Table 3-1 and Figure 3-9 show the calculated values and plot of the fractional surface coverage at a given concentration. The error bars in Figure 3-9 are indicative of the deviation in particle coverage between the measured images.

Table 3-1. Table of colloidal suspension concentrations and their corresponding fractional surface coverage on the substrate.

Colloidal Suspension Concentration (g/L)	Volume Fraction (ϕ)	Fractional Surface Coverage (θ)
600	3.16×10^{-1}	0.60±0.015
300	1.58×10^{-1}	0.52±0.019
120	6.32×10^{-2}	0.46±0.023
60	3.16×10^{-2}	0.37±0.026
6	3.16×10^{-3}	0.16±0.030

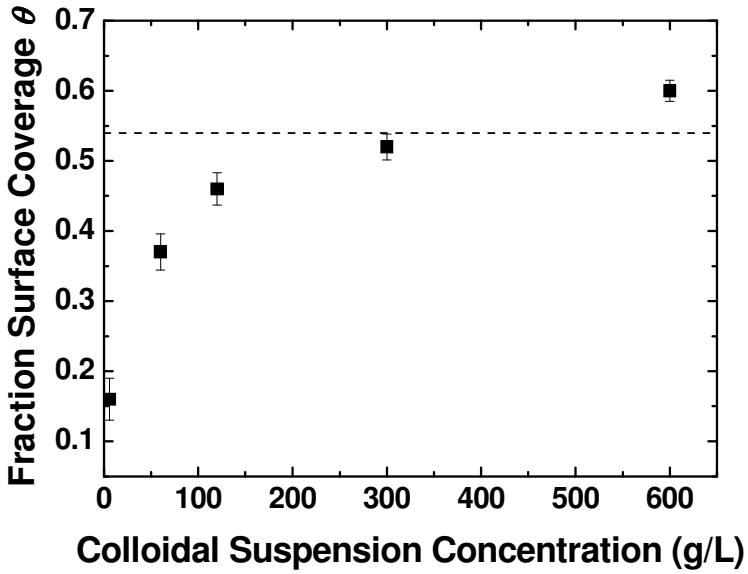

Figure 3-9. Graph plotting fractional surface coverage against colloidal suspension concentration with dashed line representing theoretical jamming limit for RSA of hard spheres.

In Figure 3-9 we observe the non linear rate of increasing adsorption with increasing concentration. The amount of adsorbed material is initially low, rising with increasing concentration and eventually approaching a plateau as the concentration is

increased to 600 g/L. A dashed line has been included to represent the theoretical jamming limit for two-dimensional RSA of monodisperse hard spheres θ_{JAM} = 0.547 [31].

3.6.4. Droplet Evaporation: Thicker Films

AFM images of the droplet evaporation samples (Figure 3-10a) indicate the formation of a multilayer film onto the mica surface. Height profiling (Figure 3-10b) shows that the colloidal film is quite flat, with height variation across the surface significantly smaller than the particle diameter.

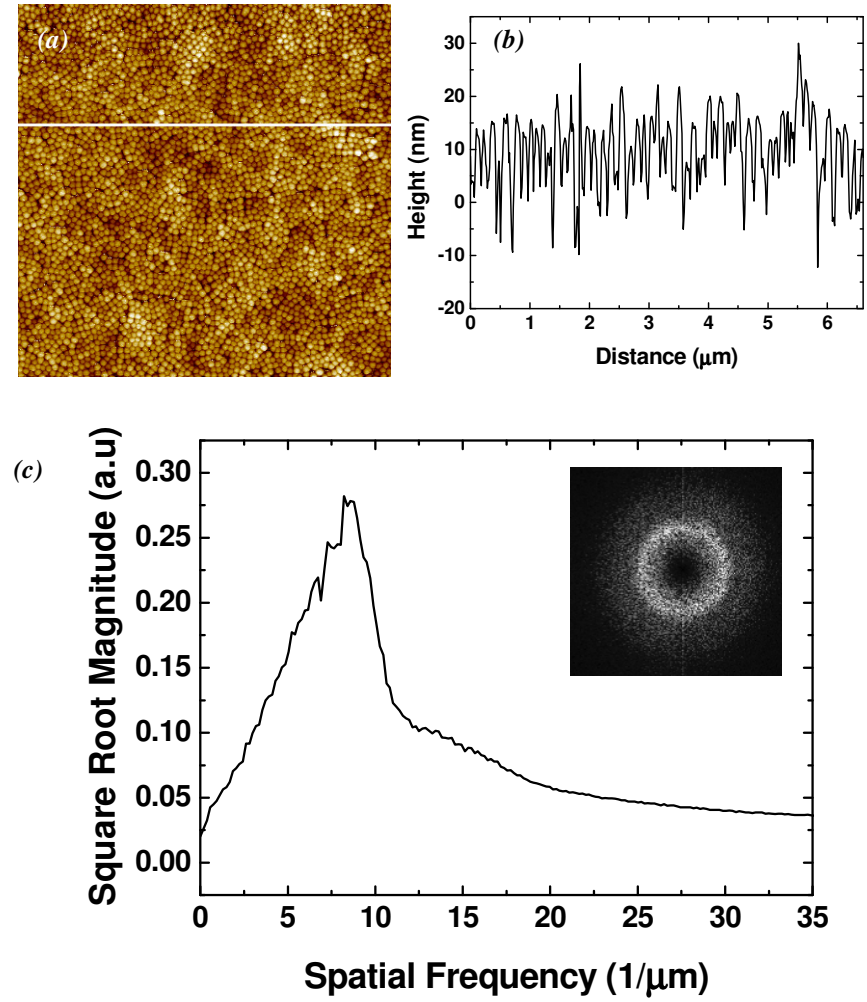

Figure 3-10. (a) 6.6 × 6.6 μm^2 topography scan of the droplet evaporation sample of the silica colloid suspension with (b) height profile corresponding to the white line on the topography showing minor variation in height over the surface of the sample and (c) its corresponding 2D-FFT. Peak corresponds to a characteristic length of 121 nm.

We performed a 2D fast Fourier transform (2D-FFT) on the 6.6 × 6.6 μm^2 topography scan (Figure 3-10) to check for the existence of any ordering in the structure of the silica nanoparticles of the droplet evaporation sample. To enhance

the contrast of weaker complex Fourier components a square root has been applied to the amplitude values. This revealed an isotropic ordering with a characteristic length between neighbouring particles of approx. 120 nm. This finding suggests a polycrystalline or dense amorphous configuration due to the existence of a characteristic length of the same order but greater than that of the particle diameter.

Looking at the 3 × 3 μm^2 topography scan (Figure 3-11a) we see that the appearance is mainly amorphous (silica spheres appear to have flat edges; this is a tip convolution effect rather than a physical property of the particle). Closer examination of the images shows some local ordered structuring of the nanoparticles into hexagonal packing (Figure 3-11b) and several sites of square packing (Figure 3-11c).

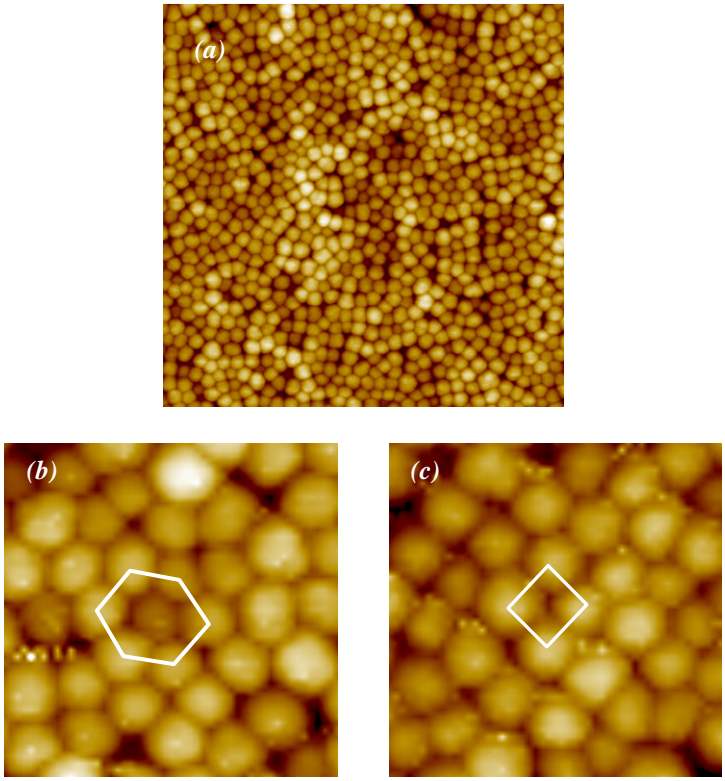

Figure 3-11. (a) 3 × 3 μm^2 topography scan of the droplet evaporation sample of the silica colloid suspension; zoomed sections showing (c) hexagonal and (d) square packing structures in the deposited film. Z range is 140 nm for all images.

3.7. Discussion

3.7.1. Dip-Coated Samples

Our dip coated samples, which are the main theme of our study, represent a system where the particles on the substrate have been adsorbed rather than deposited, as we have rinsed the substrates with the ethanol:ammonia solution after incubation to ensure that none of the particles are present due to simple deposition. The adsorption of the nanoparticle may be considered as an irreversible process. On approach to the vicinity of the surface the colloidal particle will either be repelled due to the electrostatic repulsion between the liked charge of the silica and the mica substrate or attracted due to the establishment of van der Waals interactions, becoming adsorbed to the surface. Thus the particles are weakly adsorbed but still unable to desorb from the substrate [23].

From Figure 3-9 we note that the fractional surface coverage increases with increasing colloidal concentration. For the lowest volume fraction samples we calculated the fractional surface coverage to be θ = 0.16. This number is in good agreement with particle coverage where very low electrolyte concentration has been used [32]. This suggests that the Debye length for our low volume fraction samples is comparable with that of a low electrolyte system. It is well known [33, 34] that colloidal concentration can affect the Debye length of the electrostatic double layer (EDL) at high particle volume fractions (this is especially true for nanocolloids). For our system the colloidal suspension consists of colloidal nanoparticles and their corresponding counter-ions. As each particle is effectively a 'macro-ion', in low concentrations the number of macro-ions is significantly less than the corresponding counter-ions; however at high volume fractions the macro-ion concentration becomes increasingly dominant and begins to contribute to Debye screening [33, 34]. As the range of volume fractions for our system range from $\phi = 3.16\times10^{-3}$ for the 6 g/L to $\phi = 3.16\times10^{-1}$ for the 600 g/L; the difference in the Debye length is calculated to be in the order of a factor of 5. For low ϕ the Debye length is ≈ 200 nm, while at high ϕ this has been reduced to ≈ 40 nm. This is significant variation in the EDL shell size

for the size of our particles (85 nm). At low volume fractions, the relatively unscreened EDL limits attractive van der Waals interactions between the particle and substrate, restricting particle adsorption. Conversely at higher volume fractions, the Debye length is reduced and interparticle repulsions are weakened by EDL screening. Thus, the silica particles are able to adsorb more densely onto the mica substrate attaining higher fractional surface coverage. This effect is intensified at the surface where the localised particle concentration is higher than in the bulk suspension due to the adsorption; facilitating even higher adsorption densities due to the reduced electrostatic repulsion until the system reaches a maximum coverage.

We also note that the 600 g/L sample has achieved a fractional surface coverage that is greater than the theoretical jamming limit for two-dimensional RSA of monodisperse hard spheres θ_{JAM} = 0.547 [31]. The RSA model defines a nonequilibrium process in which particles adsorb irreversibly onto a surface and remain immobile. Subsequent particles cannot overlap with adsorbed particles. However, on our systems a larger packing density has been achieved, which further elucidates that the silica spheres in our system must possess lateral mobility, facilitating particle reorganisation at the surface. Such reorganisation allows for greater packing densities than those found for fixed adsorption particles.

We found that with increasing colloidal suspension concentration, the films 'evolved' from isolated chains of a few particles (Figure 3-1) to thicker interconnected chains (Figure 3-3) that progressively broadened into a continuous mesh that ultimately approached total coverage of the substrate (Figure 3-5). The mechanism behind the distinctive patterning of the silica nanoparticles is due to the formation of attractive capillary forces between neighbouring particles during drying. A mechanism for particle structuring through capillary forces was proposed by Kralchevsky *et al.* [35]. As the liquid film thins it approaches a thickness equalling that of the colloidal particles suspended within it. Once particles become partially submerged, deformations of the liquid-gas interface give rise to strong and long-range interparticle capillary forces. A meniscus forms between neighbouring particles, the shape of which obeys the Laplace equation of capillarity and is

determined by the particle separation distance, the thickness of the liquid film and the contact angle of the particle and the surrounding liquid. The attractive force is generated by two capillary effects, the pressure effect caused by hydrostatic pressure in the gas phase being larger than in the liquid phase, especially the liquid trapped between two particles; and the surface force effect which is due to the fact that the slope of the liquid surface with respect the horizon and hence the lateral surface tension force, varies along the contact line.

Theoretical studies have shown that the strength of the lateral capillary attractions increases sharply when the interparticle distance decreases [36]. This would explain why for lower volume fractions we find that there is the presence of isolated particles, while higher volume fractions have more continuous structures. Thill and Spall [22] have constructed an aggregation model to quantify the appearance of both isolated particles and aggregates in their system. They first calculated the minimum separation distance between two particles, L_C, which would allow lateral capillary force to overcome the particle adhesion force. Using this value, they constructed a model where initially a defined number of particles were randomly distributed over a defined area, and then systematically allowed only particles with a separation distance less than L_C to aggregate. From these simulations they were able to ascertain that the fraction of isolated particles is high as soon as the average distance between the particles is larger than L_C. Therefore they were able to estimate a value of L_C based on the ratio of isolated particles, n_i, to the total number of particles adsorbed onto the substrate, n, and the average initial separation distance, D. Using their model the ratio of n_i/n can be used to find the appropriate scaling value for D in order to calculate L_C. In our system the morphology of the structure for the 6 g/L sample is indicative of a system approaching L_C due to the existence of both isolated particles and small clusters. For this sample we calculated the initial separation distance of the adsorbed particles to be 0.37 μm. Using the previously mentioned model we determine that L_C is in the order of 0.39 μm. This is in agreement with simulations [22, 23] of similar systems. It is interesting to note that this distance is comparable to two times the Debye length screening of the EDL suggesting that as expected the particle spacing is a function of the Debye length.

We also performed an energy balance measurement by comparing the attractive van der Waals energy against the lateral capillary energy as a function of particle separation distance *L*. Values for the van der Waals energy between the particles and the substrate were calculated using the surface element integration (SEI) [37] given in Equation 3-1:

$$W_{vdW}^{SEI} = -\frac{A}{6}\left[\frac{R}{D} + \frac{R}{D+2R} + \ln\left(\frac{D}{D+2R}\right)\right] \quad \textbf{3-1}$$

where A is the Hamaker constant for the silica-water-mica, calculated using the Liftshitz theorem to be 7.754×10^{-21} J, R is the particle radius and D is the separation distance (0.4 nm for a particle in "contact" with the surface). The SEI provides a more precise determination of the interaction energy than the sphere – surface equation in figure 2-2 by accurately modelling the effects of particle curvature of smaller particles. The van der Waals interaction energy was calculated to be -31.8 k_BT. To calculate the lateral capillary interactions we use the model in Figure 2-10 and equation 3-2 :

$$W_{CAP} \approx 2\pi\sigma r_c^2(\sin^2\psi_c)R/(L-2R) \quad \textbf{3-2}$$

where σ is the surface tension of the liquid (72 mN/m), r_c is the radius of the three-phase contact line at the particle surface ($r_c = [h(2R\text{-}h)]^{1/2}$), ψ_c is the mean meniscus slope angle at the contact line ($\psi_c = \arcsin(r_c/R) - \theta_c$, where θ_c is the contact angle of the bulk liquid (22°)), h is the height of the liquid layer from the top of the particle (15 nm), R is the particle radius (42.5 nm) and L is the distance between the particles. Using our earlier estimations of the critical interparticle distance, we evaluate the capillary energy at a particle separation distance L_C to be $W_{CAP} \approx 1.6\times10^3\ k_BT$ (Figure 3-12). The calculated van der Waals interactions are of several orders of magnitude lower, to the extent that they are of little influence to the capillary energy over large separation distances. Thus there is a discrepancy in the calculated values. We suggest that the silica particle interaction with the mica substrate cannot be fully accommodated with just model van der Waals attractions

for perfectly spherical particles, there may be surface irregularities on the silica surface, or polar interactions, all of which would lead to a larger attractive interaction energy between the particle and the substrate than our calculation. Even with this in mind the calculated capillary energy is excessive, suggesting that the capillary energy model used may in fact be overestimating the effective capillary energy between the particles. We note that while verification of the capillary model for micrometer particles had been performed [17], no such validation exists for nanoscale systems.

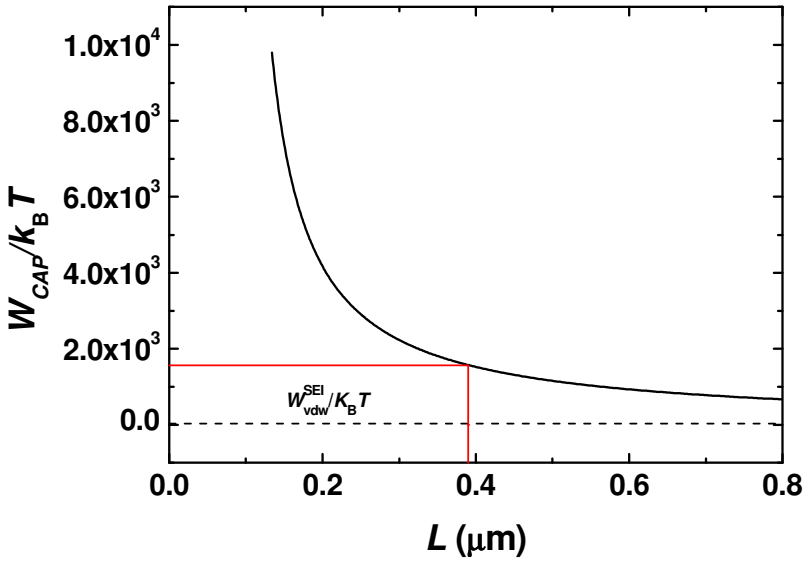

Figure 3-12. Graph of capillary energy (W_{CAP}/k_BT) as a function of interparticle distance L. The red line indicates the estimated L_C for our system and the dashed line represents the calculated value for van der Waals interaction energy (W_{vdW}/k_BT).

The existence of a critical separation distance L_C has an important impact on the morphology of our system. The low average interparticle separation distances at low fractional coverage will result in isolated particles due to their separation distance being greater than L_C; then at higher fractional coverage, we would expect $d << L_C$ resulting in stronger lateral capillary forces, leading to more ordered structuring. Comparing a low fractional coverage sample, θ_{LOW}, (Figure 3-1) to a high fractional coverage sample, θ_{HIGH}, (Figure 3-4) this behaviour can be clearly observed. As previously discussed, the morphology of θ_{LOW} exhibits isolated particles, short

lengths of chained particles and small clusters. Conversely θ_{HIGH} exhibits a continuous structure devoid of isolated particles within which patches of dense packed colloidal particles can be observed. We note however that the possibility of dewetting effects/instabilities influencing the resulting nanopatterns as the liquid film approaches nanometer thickness cannot be excluded [38]; as it has been shown such instabilities could happen even if thermodynamically one would expect complete wetting at all thicknesses [39]. Therefore fractional surface coverage can be used to dictate the morphology of a sample using self assembly via lateral capillary forces.

The lateral mobility due to the weak attractive force between the silica nanoparticle and the mica surface also plays an important role in the final configuration of the silica nanoparticles. In one set of experiments Liu *et al.* [40] used gold nanoparticles on a functionalised substrate and facilitated lateral mobility by charge reversal of the nanoparticles. The resultant patterning was attributed to the increase in lateral diffusion on the substrate, resulting in aggregation of the particles into hexagonal lattice domains. These particular assembled structures of nanoparticles bear striking resemblance to those of our on samples seen in Figure 3-4 and Figure 3-5. In contrast, work by Johnson [32] with positively charged latex particles on mica show an altogether different particle structuring. Because of the electrostatic attraction between the particles and the mica surface, irreversible adsorption of the latex particles occurred, with the electrostatic attraction rendering the adsorbed particles immobile. This *lack* of lateral mobility on the surface of the mica during the drying phase resulted in no close pack structuring of the particles. Comparing these two systems we see that the similar charge between the nanoparticles and the mica of our experimental setup has been an important factor in enabling the capillary forces to successfully form close packed structures which would have otherwise not existed in a dissimilar charge based setup. To the best of our knowledge this is the first time that a systematic investigation of the growth of a monolayer structure of colloidal nanoparticles on a surface of the same charge has been performed.

Figure 3-6 represents a sample where incomplete removal of the bulk suspension liquid has led to a partially dried sample surface, resulting in a thin film of

suspension liquid remaining on the surface of the sample. Figure 3-7 confirms that the particle height is equivalent with the estimated particle diameter indicating that the colloidal particles were not merely suspended in the liquid film but adsorbed onto the surface of the mica. Figure 3-7c indicates that the surrounding thin film of liquid was lower than the particle height at approximately 50 nm. The fact that all particles are encapsulated within the liquid film is suggestive that the particles have been swept up by the receding film and their protrusion out of it indicates that capillary forces exist between these neighbouring particles as menisci will exist between them. The phase image gives a clear representation of the particle configuration while still enveloped in the thin liquid film. We observe the particles beginning to cluster into small patches that display close packing, rather than dispersing throughout the liquid film in an even distribution of isolated particles. A higher percentage of the particles were present at the edge of the liquid film rather than in the middle. We suspect that, as the liquid film ruptures, nanoparticles are effectively pinned to the edge of the droplet forming a 'nucleus'. Particles close to the location of this nucleus cause deformations in the liquid-gas interface creating liquid meniscus bridges between them. Evaporation from these menisci causes the local curvature and hence local sucking capillary pressure to increase. This has a net effect of drawing in liquid from the surrounding film where the pressure is higher. A convective influx is established, which facilitates mass transportation of the colloidal nanoparticles within the bulk of the liquid film, leading to the migration of particles to the edges of the thin film where they are assembled under the influence of lateral capillary forces. To the best of our knowledge this is the first time that an AFM image of nanoparticles under the influence of convective/capillary effects in an evaporating thin film has been achieved.

Figure 3-8 shows the final patterns of a system where incomplete removal of the bulk suspension has led to a partially dried sample surface that was subsequently allowed to fully dry out. The presence of this excess ethanol:ammonia solution on the surface of the sample for longer times during drying has encapsulated a large number of silica particles as it wets the surface. Thus, the laterally mobile particles have migrated under the influence of convection influx and swept along in the receding

film. This allowed for large numbers of particles to be relocated towards the film edge, resulting in both larger structures and greater voids on the mica surface. Although the samples shown in Figure 3-3 and Figure 3-8 were created using the same concentration and submersion times, the disparity in their final colloid structuring highlights the significance of drying kinetic effects. While the final configuration of the sample with a relatively long drying time led to the formation of large dense structures surrounded by empty voids (Figure 3-8), in systems with rapid drying (from a nitrogen jet) we effectively maintained the distribution of the particles relatively close to their final adsorption locations (Figure 3-3). The network structures are quite narrow and well spread out; a result of a limited time frame for extensive convection influx and capillary driven self assembly to occur over. This system is representative of the majority of our dip coated samples which were subjected to rapid drying.

3.7.2. Droplet Application Samples

Having explored monolayer nanoparticle behaviour we turned our attention to thicker multilayered deposited films achieved by using droplet application of the colloidal suspension and slow drying.

The film of particles was measured to be quite flat (Figure 3-10), with the variance in height less than that of the measured particle diameter. This suggests that the film is typically laminar in its layering at these scales ($6.6 \times 6.6\ \mu m^2$). Lack of any substrate reference point to make a film thickness measurement meant that we are unable to determine if there was any bias for deposition at either the edge or centre of the sample area, which would have indicated a transportation of the solid material to the extremities of the sample substrate, in a process similar to the coffee stain effect [41].

Further investigation of the film particle structuring was achieved by carrying out 2D-FFT analysis (Figure 3-10). The 2D-FFT measurements of the topography revealed an isotropic order with a characteristic distance between particles of approximately 120 nm. The existence of a characteristic length larger than the particle diameter suggests that there was a predominantly amorphous deposition (with some localised ordered structuring, Figure 3-11, that we will discuss later). We propose two possible mechanisms that have led to this predominantly amorphous structure. As our system is based on a colloidal suspension of ethanol:ammonia, evaporation rate at room temperature/pressure would be relatively quick, creating strong hydrodynamic forces within the evaporating suspension that could ultimately rupture the film at an early stage leading to an amorphous deposited structure of the nanoparticles. Such evaporative effects were observed by Adachi et al. [42] where rapid solvent evaporation was performed, creating instabilities in the film growth leading to breaks and rupturing of the films structuring. Dynamic changes in the concentration may also adversely affect the film structure. At very high volume fractions the Debye length can become increasingly compressed until interparticle van der Waals attraction causes the formation of colloidal particle aggregates, leading to disorganised structuring [43]. The stock colloidal suspension

concentration (600 g/L) resulted in a very condensed deposition on the sample substrate and, furthermore, as the droplet evaporated the concentration increased making the likelihood of nanoparticle aggregation effects possible and affecting the crystallinity.

In Figure 3-11 we find localised ordering of the nanoparticles, including some hexagonal packing (Figure 3-11b) and several sites of square packing (Figure 3-11c). We suspect that these formations have occurred due to a combination of capillary forces drawing the particles close together and imperfections in underlying layers of colloidal particles adversely affecting the packing order. The occurrence of capillary forces between the particles has facilitated a close packing formation of the colloids leading to the structures we observed in localised areas. Imperfections in underlying layers induced distortions in subsequent layers, restricting the formation of long range crystalline structures. It is interesting to note that rather than areas of hexagonal packing structures being evident we observed several sites of simple square packing over the imaged area. We suspect that the underlying film has limited the lateral mobility of the particles by pinning them in the undulations on the surface of the underlying deposited film (an effect reminiscent of substrate patterning induced self-assembly) resulting in the formation of the observed structures.

3.8. Conclusions

By using dip coating and droplet application of silica nanocolloidal suspension on mica and AFM imaging we have provided an insight into the nanoparticle mechanisms of both adsorption and structuring upon drying. We have observed an array of adsorption/deposition and self assembly patterns that we have interpreted using current theory of colloidal behaviour.

The adsorption of silica nanoparticles on mica was found to be irreversible but possess lateral mobility due to the weak attractive force between the silica nanoparticle and the mica substrate. High volume fractions, ϕ, have been shown to affect the Debye length of the EDL shell on the colloidal particle, leading to higher adsorption with increasing ϕ. Furthermore, it was found that the fractional surface coverage, θ, for the highest ϕ was larger than the theoretical jamming limit for two-dimensional RSA of monodisperse hard spheres $\theta_{JAM} = 0.547$. This result confirmed that our system possessed lateral mobility, which in this case has facilitated denser particle adsorption than that for truly irreversible RSA.

The chain and closed packed structures observed is an indirect evidence of capillary force structuring. The minimum separation distance between two particles which would allow lateral capillary force to overcome the particle adhesion force leading to particle structuring was found to be in good agreement with similar studies of weakly adsorbed particles. However, the calculations using the widely accepted capillary model was found to overestimate the capillary energy which suggests that a new model might have to be devised for the nanoscale. Moreover, our AFM phase imagery of the "dynamic" drying system provided excellent direct experimental evidence of the capillary and convective forces that led to the final structuring of nanoparticles. These images provide invaluable experimental proof of theoretical ideas on the final drying behaviour of nanofluid films on surfaces. Furthermore, we showed that rapid drying resulted in homogenous well-spread drying patterns while slow drying produced larger structures separated by large empty areas across the

sample surface. Exploration of thicker films of the silica nanoparticles using droplet evaporated samples showed evidence of both dense amorphous structuring and localised closed packed ordering of nanoparticles originating from drying kinetics effects.

3.9. References

[1] S. Maenosono, T. Okubo, Y. Yamaguchi, Journal of Nanoparticle Research 5 (2003) 5-15.
[2] J. V. Barth, G. Costantini, K. Kern, Nature 437 (2005) 671-679.
[3] D. Mijatovic, J. C. T. Eijkel, A. van den Berg, Lab on a Chip 5 (2005) 492-500.
[4] G. Subramanian, V. N. Manoharan, J. D. Thorne, D. J. Pine, Advanced Materials 11 (1999) 1261-1265.
[5] O. D. Velev, E. W. Kaler, Langmuir 15 (1999) 3693-3698.
[6] S. H. Behrens, D. G. Grier, Journal of Chemical Physics 115 (2001) 6716-6721.
[7] S. E. Pratsinis, Progress in Energy and Combustion Science 24 (1998) 197-219.
[8] W. Stöber, A. Fink, E. Bohn, Journal of Colloid and Interface Science 26 (1968) 62-69.
[9] D. L. Green, J. S. Lin, Y. F. Lam, M. Z. C. Hu, D. W. Schaefer, M. T. Harris, Journal of Colloid and Interface Science 266 (2003) 346-358.
[10] T. I. Suratwala, M. L. Hanna, E. L. Miller, P. K. Whitman, I. M. Thomas, P. R. Ehrmann, R. S. Maxwell, A. K. Burnham, Journal of Non-Crystalline Solids 316 (2003) 349-363.
[11] M. Qhobosheane, S. Santra, P. Zhang, W. H. Tan, Analyst 126 (2001) 1274-1278.
[12] T. P. Bigioni, X. M. Lin, T. T. Nguyen, E. I. Corwin, T. A. Witten, H. M. Jaeger, Nature Materials 5 (2006) 265-270.
[13] A. S. Dimitrov, K. Nagayama, Langmuir 12 (1996) 1303-1311.
[14] G. M. Whitesides, B. Grzybowski, Science 295 (2002) 2418-2421.
[15] P. N. Pusey, W. Van Megen, P. Bartlett, B. J. Ackerson, J. G. Rarity, S. M. Underwood, Physical Review Letters 63 (1989) 2753-2756.
[16] K. J. Mutch, V. Koutsos, P. J. Camp, Langmuir 22 (2006) 5611-5616.
[17] P. A. Kralchevsky, N. D. Denkov, Current Opinion in Colloid & Interface Science 6 (2001) 383-401.
[18] N. D. Denkov, O. D. Velev, P. A. Kralchevsky, I. B. Ivanov, H. Yoshimura, K. Nagayama, Langmuir 8 (1992) 3183-3190.
[19] J. Aizenberg, P. V. Braun, P. Wiltzius, Physical Review Letters 84 (2000) 2997-3000.
[20] Z. Adamczyk, Journal of Colloid and Interface Science 229 (2000) 477-489.
[21] Z. Adamczyk, B. Siwek, M. Zembala, Colloids and Surfaces 62 (1992) 119-130.
[22] A. Thill, O. Spalla, Langmuir 18 (2002) 4783-4789.
[23] O. Spalla, S. Desset, Langmuir 16 (2000) 2133-2140.
[24] P. A. Kralchevsky, K. Nagayama, Langmuir 10 (1994) 23-36.
[25] Z. C. Zhou, Q. Li, X. S. Zhao, Langmuir 22 (2006) 3692-3697.
[26] M. Shimomura, T. Sawadaishi, Current Opinion in Colloid & Interface Science 6 (2001) 11-16.
[27] G. C. Qi, Y. L. Yang, H. Yan, L. Guan, Y. B. Li, X. H. Qiu, C. Wang, Journal of Physical Chemistry C 113 (2009) 204-207.
[28] J. N. Israelachvili, N. A. Alcantar, N. Maeda, T. E. Mates, M. Ruths, Langmuir 20 (2004) 3616-3622.

[29] I. Schmitz, M. Schreiner, G. Friedbacher, M. Grasserbauer, Applied Surface Science 115 (1997) 190-198.
[30] J. Tamayo, R. Garcia, Langmuir 12 (1996) 4430-4435.
[31] J. Feder, Journal of Theoretical Biology 87 (1980) 237-254.
[32] C. A. Johnson, A. M. Lenhoff, Journal of Colloid and Interface Science 179 (1996) 587-599.
[33] J. Goodwin, Colloids and Interfaces with Surfactants and Polymers: An Introduction, 2004.
[34] W. B. Russel, D. A. Saville, W. R. Schowalter, Colloidal Dispersions, Cambridge University Press, Cambridge, 1989.
[35] P. A. Kralchevsky, V. N. Paunov, N. D. Denkov, I. B. Ivanov, K. Nagayama, Journal of Colloid and Interface Science 155 (1993) 420-437.
[36] P. A. Kralchevsky, V. N. Paunov, I. B. Ivanov, K. Nagayama, Journal of Colloid and Interface Science 151 (1992) 79-94.
[37] S. Bhattacharjee, M. Elimelech, Journal of Colloid and Interface Science 193 (1997) 273-285.
[38] C. P. Martin, M. O. Blunt, E. Pauliac-Vaujour, A. Stannard, P. Moriarty, I. Vancea, U. Thiele, Physical Review Letters 99 (2007).
[39] B. F. Macdonald, R. J. Cole, V. Koutsos, Surface Science 548 (2004) 41-50.
[40] S. T. Liu, T. Zhu, R. S. Hu, Z. F. Liu, Physical Chemistry Chemical Physics 4 (2002) 6059-6062.
[41] R. D. Deegan, O. Bakajin, T. F. Dupont, G. Huber, S. R. Nagel, T. A. Witten, Nature 389 (1997) 827-829.
[42] E. Adachi, A. S. Dimitrov, K. Nagayama, Langmuir 11 (1995) 1057-1060.
[43] D. A. Barros, C. Hisano, R. Bertholdo, M. G. Schiavetto, C. Santilli, S. J. L. Ribeiro, Y. Messaddeq, Journal of Colloid and Interface Science 291 (2005) 448-464.

Chapter 4: Silica Nanoparticles on Mica – Size Effects

4.1. Abstract

We present the investigation of the structuring behaviour of negatively charged colloidal silica nanoparticles of diameter 10 nm, 50 nm and 100 nm adsorbed on mica substrates by dip coating methods. Imaging of the samples was performed using atomic force microscopy (AFM). The 10 nm particles exhibited significant levels of adsorption for all the concentrations and incubation times used, and formed intricate 2D cellular networks and thick amorphous films with increasing concentration. The 50 nm particles showed very limited particle adsorption at low concentrations, and the presence of isolated clustering at intermediate concentrations. At high concentrations the formation of dense, almost monolayer, amorphous films was observed. The 100 nm particles showed almost nonexistent adsorption at low concentrations, with isolated dispersed adsorption at intermediate concentrations. At high concentrations well ordered structures of hexagonal close packing, as well as more dispersed close packed clusters were seen to form across the mica substrate. We observed both volume fraction effects, where high colloidal concentration has resulted in reduced Debye length and subsequent increased particle adsorption at the substrate; and kinetics effects where diffusion and adsorption rates have shown adsorption amounts to be a function of both concentration and particles size. Particle structuring was observed to be a particle size dependent behaviour. The highly crystalline monolayers of the high concentration 100 nm particle samples were attributed to the formation of strong lateral capillary forces due to the short interparticle distances from high adsorption densities. For the 2D cellular structures of the 10 nm particles, comparisons drawn with the final stages of dewetting and 2D-FFT measurements suggested a spinodal-like dewetting mechanism. Finally the 50 nm particle structures at intermediate concentrations were analysed using Voronoï tessellation, the results of which suggested some underlying ordering. We surmise that this particle size may be subject to a mixture of structuring due to capillary forces and subsequent disordering from dewetting forces leading to the lack of well defined structuring. For structuring we investigated the effectiveness of convective and capillary forces as a function of particle size and discuss dewetting phenomenon in the case of 10 nm.

4.2. Introduction

As industry strives to improve efficiency and reduce costs of manufacturing ever smaller devices; it has begun to approach the physical limits of what top down manufacturing techniques can achieve. This has lead to the viability of bottom up techniques to being investigated as an alternative manufacturing technique [1, 2]. Self assembly [3-7] is a major component of this type of manufacturing. It allows disordered systems of pre-existing components to form organized structures or patterns without external assistance. The structures created are determined by the local interactions between the components. To exploit self assembly techniques at an industrial level, researchers have turned their attention to the biological systems where complex life forms are spontaneously self assembled from simple building blocks [8]. Attempts to mimic these processes in the lab have resulted in the formation of different kinds of nanometer sized structures. These nanostructures were shown to be viable in a number of applications including photonics [9], biosensors [10], the semiconductor industry [3, 10] and quantum dot technology [11]. Colloidal particles have been widely used as a stock material in constructing nanostructures due to their modifiable physicochemical properties [12, 13]. This has fuelled research into the behaviour of colloidal particle in suspension [15, 16], their subsequent deposition or adsorption [17-19] onto a surface and their final structuring during drying [14-22]. Silica colloidal particles [23] have been used extensively in research due to their native surface chemistry providing an effective negative electrostatic repulsion through the dissociation of the exposed silanol groups in water [24], maintaining colloidal stability. This provides a simple colloidal system for studying colloidal behaviour as it does not require any additional chemical alteration of the colloidal surface to provide an effective electrostatic or steric repulsion for colloidal stabilisation [13].

Previous research into the behaviour of colloidal particles on solid surfaces can be divided into three main areas; transportation within the suspension, adsorption onto fixed surface and drying effects. Transportation of colloidal particles to a fixed

surface is dominated by convection and diffusion within the colloidal suspension. Colloidal diffusion studies using the Stokes-Einstein equation to evaluate Brownian behaviour highlight the relationship between particle size and its relaxation time (i.e. the time it takes a particle to diffuse its own radius) [25]. Particle adsorption is governed by the colloidal-surface interactions which operate over short distances. Adamczyk *et al.* has conducted extensive studies covering many aspects of *strong and irreversible* adsorption of particles (caused by electrostatic attraction between opposite charged particles and surfaces) [17, 19] and diffusion controlled adsorption kinetics [26] covering both theoretical and experimental aspects of the adsorption process. In these cases the irreversibly adsorbed particles influence the localised adsorption behaviour limiting the maximum fractional coverage. We note that research on systems of particles and substrate with similar charge is very sparse. We have begun to investigate the enhanced surface particle mobility of systems using silica particles manufactured using the Stöber-gel process deposited on mica in chapter 3 and found that the electrostatic repulsion between the similarly charged colloidal particles and substrate facilitated the capillary structuring of ordered structures; as well as resulting in an increased particle adsorption density. This behaviour was attributed to the role of capillary and convective forces during rapid drying of the nanoparticles which has also been observed in other systems such as polymers and soft colloids [27-29]. Better understanding of the weak adsorption behaviour would facilitate a better understanding of the initial nanoparticle adsorption density, which in turn could be exploited via attractive capillary forces to produce highly ordered structures of colloidal nanoparticles. This is paramount for maximising the potential of self assembling nanoparticles, a process crucial to the nanotechnology industry. Another major factor in the effectiveness of capillary forces is particle size. While mathematical studies of interparticle capillary forces induced by the evaporating menisci exist [25, 36], experimental studies in the effects of particle size on self assembly behaviour are limited, mostly involving a polydisperse system of colloidal particles [37, 38]. Dimitrov conducted a study of latex particles ranging from 79 nm to 2 μm in diameter [20], but only presented well ordered crystalline structures for particles greater than 300 nm. A limiting factor encountered in his experiments was film rupturing due to dewetting phenomena. The

study of the dewetting phenomenon has been performed mainly using model systems such as amorphous polymer films (in order to minimise evaporation/drying effects of liquids and because relaxation times are longer) [30]. Application of detwetting mechanisms to form patterns with colloidal solutions of nanoparticles (nanofluids) has started to be utilised only very recently. Studies by Moriarty [31, 32], Rabani [33] and Thiele [36, 37] have shown the formation of 2D cellular configurations that exhibit some level of ordering and structure for nanoparticles of a few nanometers in size. However, research into how dewetting behaviour affects the self assembly of larger nanoparticles is uncommon. While there are several different, separate studies of self assembly of nanoparticles of various diameters, there is no study where the same system of nanoparticles with differing sizes is investigated systematically under the same conditions. A better understanding of the dependence of *nanoparticle size* on surface *adsorption* and subsequent *self assembly* upon drying is needed in order to fully exploit the applications of nanoparticles in industry.

In this chapter, we present the investigations into the behaviour of negatively charged colloidal silica nanoparticles of diameter 10 nm, 50 nm and 100 nm adsorbed on mica substrates by dip coating methods. We investigated the fine structure of the nanoparticle assemblies using atomic force microscopy (AFM) techniques. Adsorption behaviour was discussed in terms of volume fraction and kinetics effects while particle structuring was analysed in detail. For the 10 nm particles we have observed intricate 2D cellular networks forming at intermediate concentrations. The 50 nm particles produced an array of different formations of relatively low coverage until at high concentration where they formed dense, almost monolayer, amorphous films. The 100 nm particles were observed to form well ordered structures of hexagonal close packing, as well as more amorphous clusters at high concentrations. We discuss the origins of the size-dependent behaviour.

4.3. Materials

All colloidal samples used in this study were aqueous dispersions of amorphous, non porous fumed silica colloidal particles of a concentration of 50 g/L ($\phi = 2.27\times10^{-2}$) purchased from Polysciences Inc. (Baden-Württemberg, Germany). Three particle diameter sizes were chosen for the experiments; 100 ± 30 nm, 50 ± 10 nm and 10 nm particles with a broad distribution in size. Particles were supplied nonfunctionalised and suspended in deionised water from the manufacturer. 11 mm square mica sheets supplied by Fisher (Leicestershire, United Kingdom) were used for sample substrates and metal mounting discs. All water used in the experiments was ultrapure water with a resistivity of 18.2 MΩ-cm at 25°C. The colloidal samples were further diluted by factors of 10 to make secondary and tertiary dispersions of 5 g/L ($\phi = 2.27\times10^{-3}$) and 0.5 g/L ($\phi = 2.27\times10^{-4}$) using ultrapure water. The suspensions were refrigerated at 4°C for storage purposes. Particle ζ-potentials were evaluated using a Malvern Zetasizer (Worcestershire, United Kingdom) and for the three colloidal sizes were measured to be -41.5mV for the 100 nm particles, -37.9 mV for the 50 nm particles and -19.2 mV for the 10 nm particles.

4.4. Experimental Methodology

Mica sheets were freshly cleaved by running a scalpel along the lateral plane of the sheet. This was performed inside a fume cupboard to minimise airborne pollutants from contaminating the surface. The colloidal suspensions were agitated for 30 seconds to minimise any sedimentation that may have occurred. All samples were prepared by fully submerging the freshly cleaved mica in an upright position into a vial of the colloidal suspension using clean stainless steel forceps to minimise contamination. This was then placed in a sealed box at room temperature/pressure, again to avoid airborne particles from contaminating the sample or the suspension in the vial. Once the required incubation time had elapsed, the sample was removed and gently rinsed with fresh ultrapure water and dried with a nitrogen jet to remove the water from the surface of the substrate. The sample was then placed in a glass

covered Petri dish and put in a drying oven for 1 hour at 60°C to ensure that the sample was completely free of any liquid. The mica was then mounted onto a metal sample disc with double sided adhesive tape. Light pressure was applied to the edges of the mica to secure it. Prepped samples were stored in a dry desiccator under vacuum to ensure no moisture would build up on the sample surface whilst in storage.

4.5. Measurements

Imaging was done using atomic force microscopy on a Veeco Multimode/Nanoscope IIIa AFM (Santa Barbara, CA, USA) under soft tapping mode™ regime (the cantilever tip makes intermediate contact with the surface) using silicon nitride cantilevers from Windsor Scientific Ltd (Berkshire, United Kingdom) with a resonance frequency of approximately 300 MHz, and a spring constant of 42 N/m. The nominal tip radius was quoted by the manufacturer as <8 nm. The cantilevers were operated at approximately 5% lower than their resonance frequency and the resonating tip was lowered close enough to the surface to cause the tip to make intermittent contact with the surface. Raster scans of areas of interest were performed at various sizes. All scans were performed in air at room temperature. The tip of the silicon nitride cantilevers usually acquires a negative charge due to moisture in the atmosphere forming acidic silanol groups on the tip surface; this inhibits contamination of the tip end with the charged colloidal particles [34, 35]. For post processing of the AFM images Scanning Probe Image Processor (SPIP) from Image Meteorology (Hørsholm, Denmark) was used. Except where stated all images were post-processed by simple flattening alone. The surface coverage and volume of adsorbed material were calculated using grain analysis in SPIP. Calculations of the adsorbed area and volume of material were calculated directly from the AFM images and consequently the deduced adsorbed amounts suffer from convolution effects, as discussed in chapter two. Voronoï analysis was carried out using our own code written in Matlab from The Mathworks (Natick, MA, USA).

The images presented are representative of the concentration and conditions of sample preparation for every occasion unless otherwise stated. Deconvolution was not possible for all images (due to particles of different radii and multilayer adsorption) so we have used the apparent area and volume coverage taken directly from the AFM images. Thus the resulting area and volume coverage data will only be used in a relative rather than absolute context when making comparisons on adsorption behaviour. It should be noted the probe tip is comparable with the size of the 10 nm particles, which will cause the widths of the adsorbed particles to appear greater than their actual diameters. This will result in the apparent surface area and volume coverage to be exaggerated.

4.6. Results

The results are presented in the following manner; increasing particle size, increasing concentration and increasing incubation times.

4.6.1. 10 nm Silica Particles

Figure 4-1 shows the topography scans of samples incubated for 60 minutes, 120 minutes and 24 hours in a colloidal suspension of 10 nm silica nanoparticles of 0.5 g/L concentration.

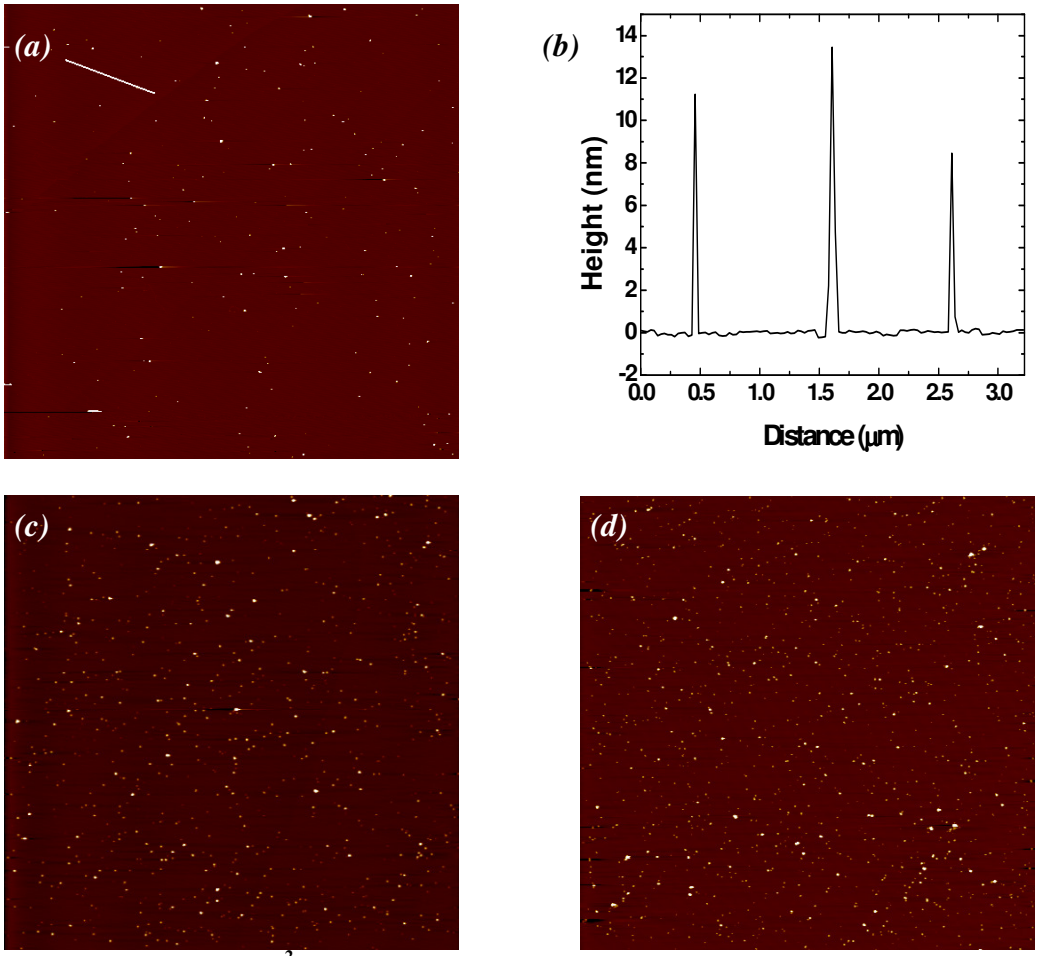

Figure 4-1. 14.9 × 14.9 μm^2 topography scans of samples incubated for (a) 60 minutes with (b) height profile corresponding to the white line. 14.9 × 14.9 μm^2 topography scans for (c) 120 minutes and (d) 24 hours incubation time, all in a 0.5 g/L 10 nm colloidal suspension.

We see that the nanoparticles have adsorbed onto the surface in a largely isolated fashion. Height profiling of the particles confirms that the silica nanoparticles are of the order of 10 nm in diameter. Table 4-1 gives the surface coverage and adsorbed volume of particles as a function of incubation time. We note that the particle surface coverage and adsorbed volume increase with increasing incubation time.

Table 4-1. Comparison of topography properties with respect to increasing incubation times of the 0.5 g/L 10 nm colloidal suspensions.

Incubation Time	Surface Coverage (%)	Adsorbed Volume (μm^3)
60 minutes	0.08	2.08E-3
120 minutes	2.80	2.08E-2
24 hours	6.94	8.44E-2

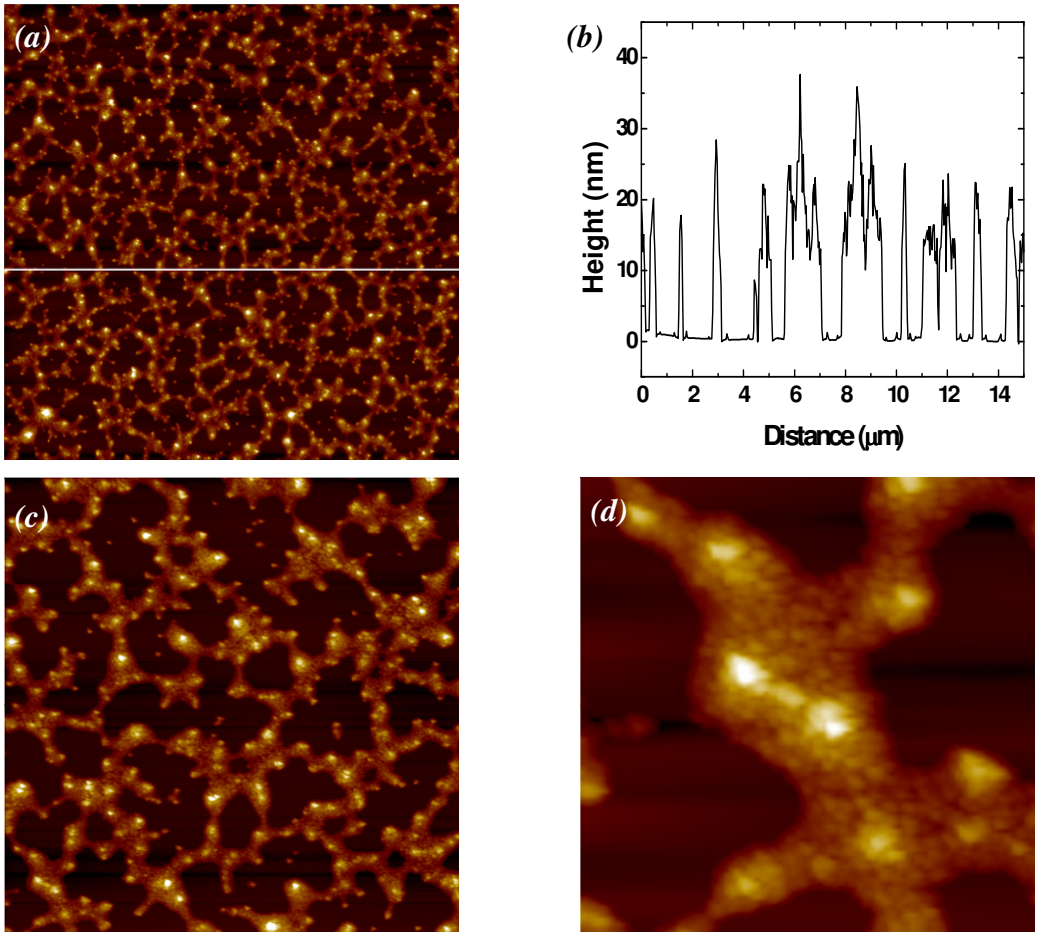

Figure 4-2. (a) 14.9 × 14.9 μm^2 topography scans of samples incubated for 60 minutes in a 10 nm 5 g/L colloidal suspension with (b) height profile corresponding to the white line in the topography image. (c) 6.5 × 6.5 μm^2 topography scan and (d) zoom showing the presence of individual particles of silica.

Figure 4-2 shows the topography of samples incubated for 60 minutes in a 10 nm silica nanoparticle suspension of 5 g/L concentration. The nanoparticles have structured themselves into an interconnected 2D cellular structure, exhibiting linked clusters of colloidal particles and a moderate degree of coverage (38% of the total surface area). A height profile shown in Figure 4-2b gives a good representation of the profile height of the structure. The majority of the coverage is approximately 20 nm in height, with a few larger structures over 40 nm. The individual colloidal nanoparticles appear to be densely packed in an amorphous configuration.

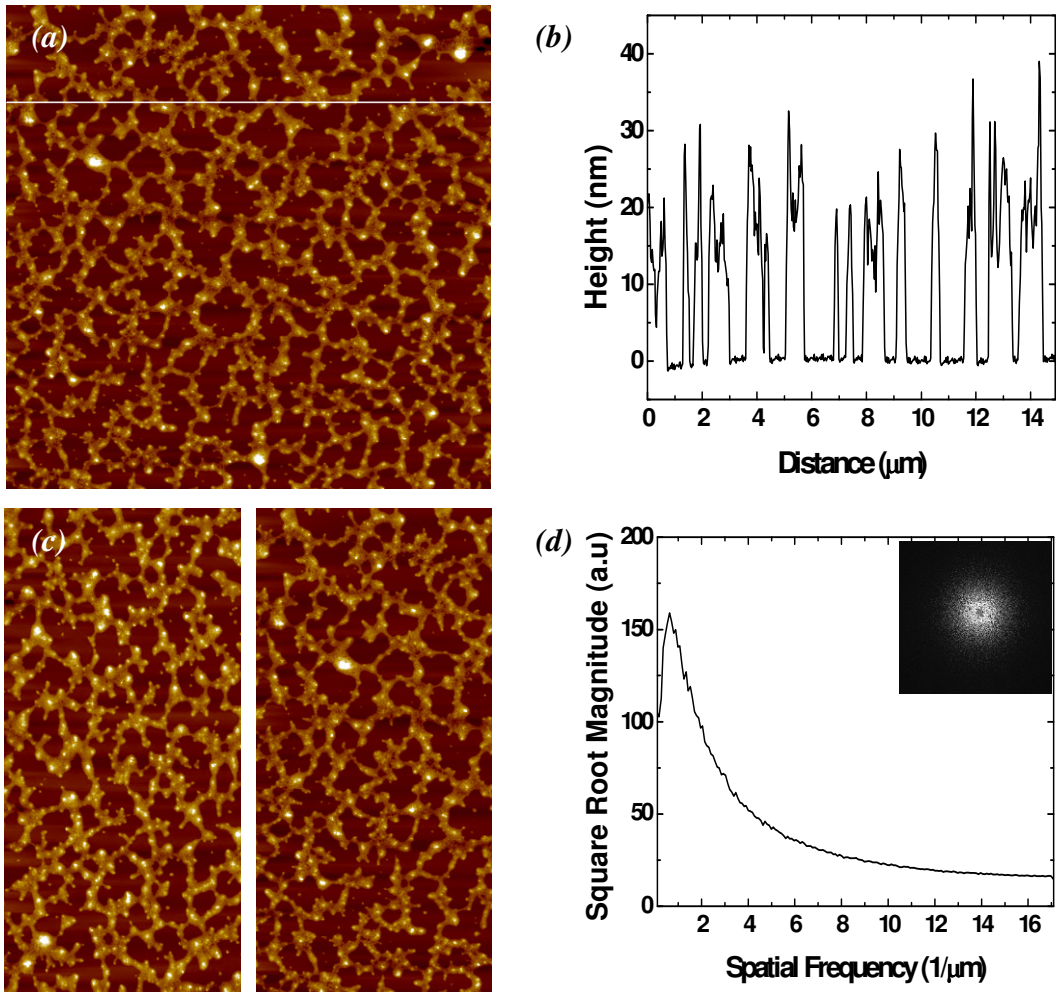

Figure 4-3. (a) 14.9 × 14.9 μm^2 topography scan of samples incubated for 120 minutes in a 10 nm 5 g/L colloidal suspension with (b) height profile corresponding to the white line in the topography image. (c) A comparison between the 60 minute incubation (left) and the 120 minute incubation (right) samples shows similarity between final structuring. (d) Radially-averaged 2D-FFT of (a).

Figure 4-3a shows a typical topography image of samples that were incubated for 120 minutes in a suspension of 10 nm silica nanoparticles of 5 g/L concentration. We note that the patterning has not changed significantly from that of the 60 minute samples (Figure 4-3c). There also appears to be a slight increase in the average Z height of the topography structure, at 25-30 nm. A 2D-FFT of the topography reveals a characteristic length scale to the cellular structure of ≈ 900nm.

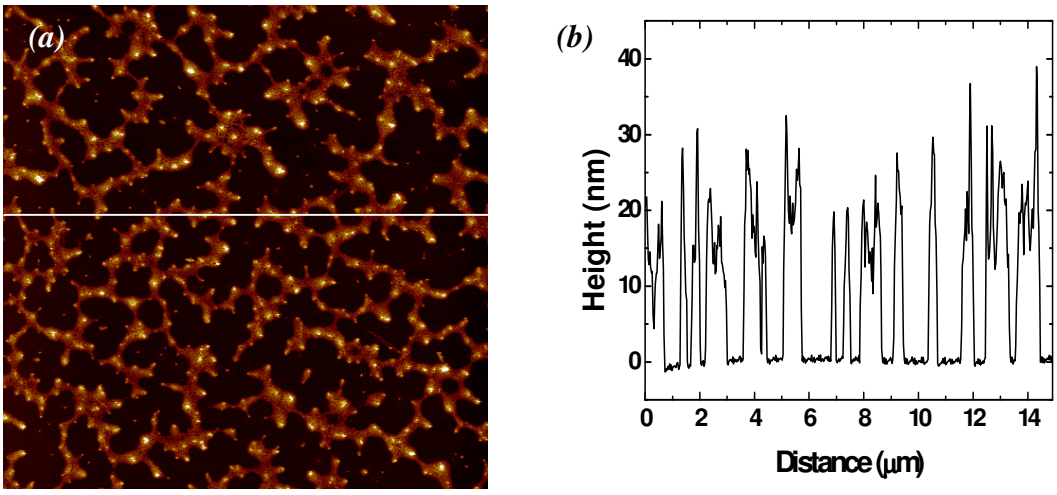

Figure 4-4. (a) 14.9 × 14.9 μm^2 topography scan of sample incubated for 24 hours in a 10 nm 5 g/L colloidal suspension with (b) height profile corresponding to the white line in the topography image.

In Figure 4-4 the topography image of a sample incubated for 24 hours in a suspension of 10 nm silica nanoparticles of 5 g/L concentration shows that the nanoparticles have again configured into a final structure similar to that of the 60 and 120 minute samples. We note however that the interconnected structure appears to be less established, although the average height profile of the formations are comparable with those of the previous samples.

Table 4-2 shows that final particle structure and area coverage are predominantly unaffected by incubation times, however there is a small increase in the adsorbed volume of material on the samples as incubation times increased.

Table 4-2. Comparison of topography properties with respect to increasing incubation times of the 5 g/L 10 nm colloidal suspensions.

Incubation Time	Area Coverage (%)	Adsorbed Volume (μm^3)
60 minutes	38	0.684
120 minutes	41	0.829
24 hours	37	1.123

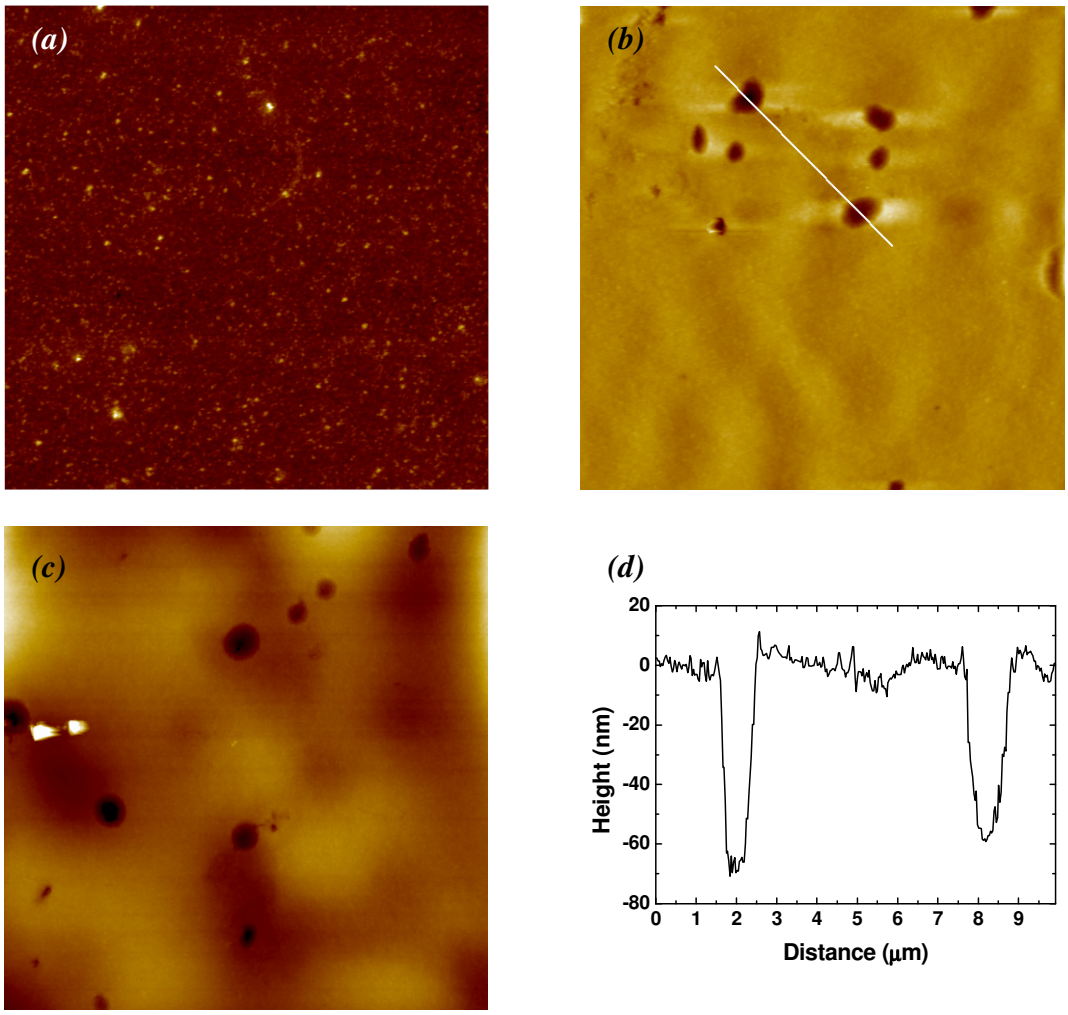

Figure 4-5. 14.9 × 14.9 µm^2 topography images incubated for (a) 60 minutes (Z range approximately 30 nm) (b) 120 minutes (Z range approximately 90 nm) and (c) 24 hours (Z range approximately 200 nm) in a 10 nm 5 g/L colloidal suspension. (d) Height profile corresponding to the white line in the topography image of the 120 minute sample.

Figure 4-5 shows the formation of a continuous film of colloidal particles for all incubation times at a concentration of 50 g/L. The depth of the film on the 120 minute incubation sample suggests it is multilayer, having a thickness in excess of 70 nm (Figure 4-5d). The film structure is relatively smooth, with surface roughness comparable to the colloidal size (Figure 4-6). The 120 minute and 24 hour samples seem to be remarkably similar in their topographical appearance, with the 24 incubation sample have holes of depth ≈100nm. Their similarity suggests a limit of adsorbance has occurred. The presence of the holes also suggests similar phenomena have occurred in their formation.

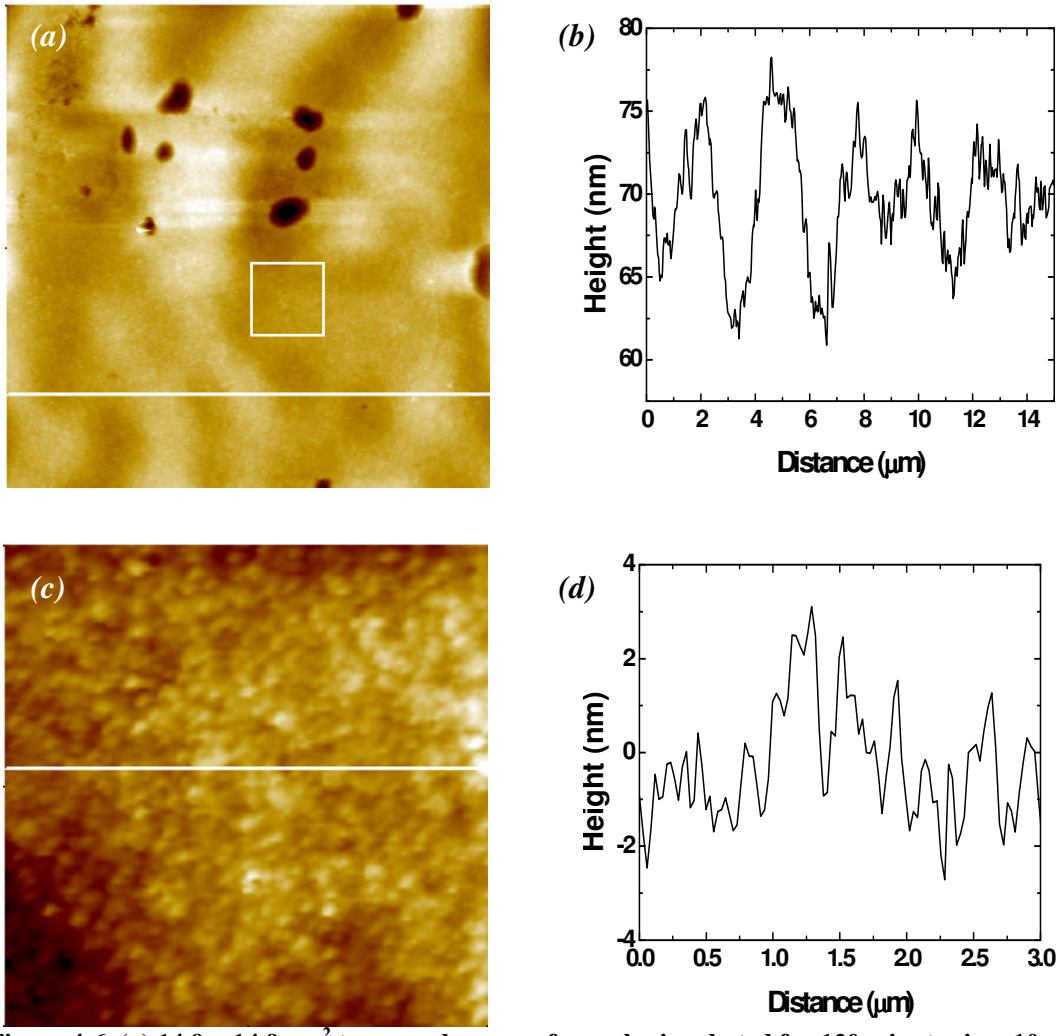

Figure 4-6. (a) 14.9 × 14.9 μm^2 topography scan of samples incubated for 120 minutes in a 10 nm 50 g/L colloidal suspension. (b) Height profile corresponding to the white line in the topography image. (c) Magnified section of the topography corresponding to the white box with (d) height profile corresponding to the white line in the zoomed image.

4.6.2. 50 nm Silica Particles

Figure 4-7 is representative of the colloidal adsorption of the 50 nm silica nanoparticles incubated for 60 minutes, 120 minutes and 24 hours in a 0.5 g/L colloidal suspension. The majority of samples present very low adsorption coverage at this concentration. At 60 minutes most scans were either blank or showed a small number of isolated particles. At 120 minutes incubation time most topography scans revealed several isolated particles and at 24 hours the amount of observed adsorbed material had not noticeably increased.

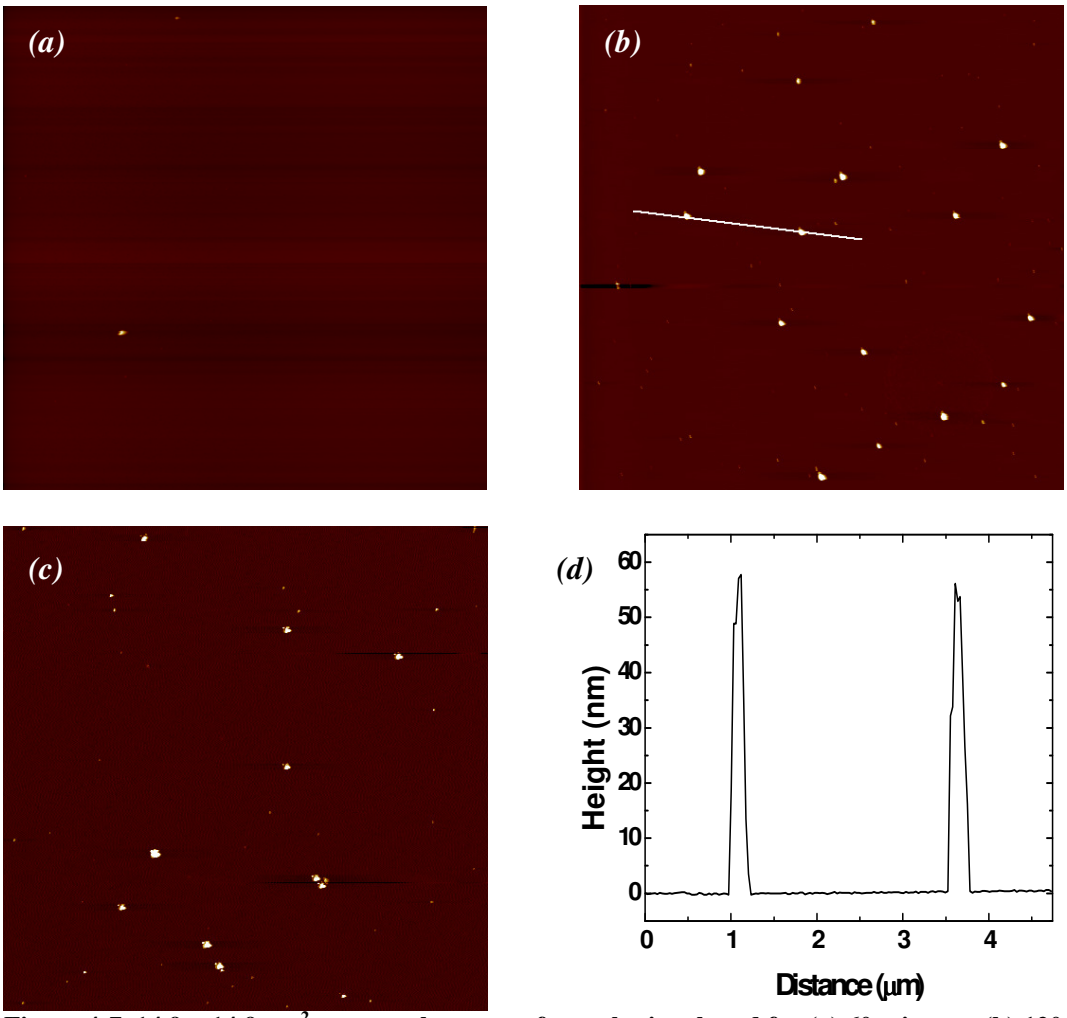

Figure 4-7. 14.9 × 14.9 μm^2 topography scans of samples incubated for (a) 60 minutes, (b) 120 minutes and (c) 24 hours in a 50 nm 0.5 g/L colloidal suspension. (d) Height profile corresponding to the white line in the 120 minutes incubation topography image.

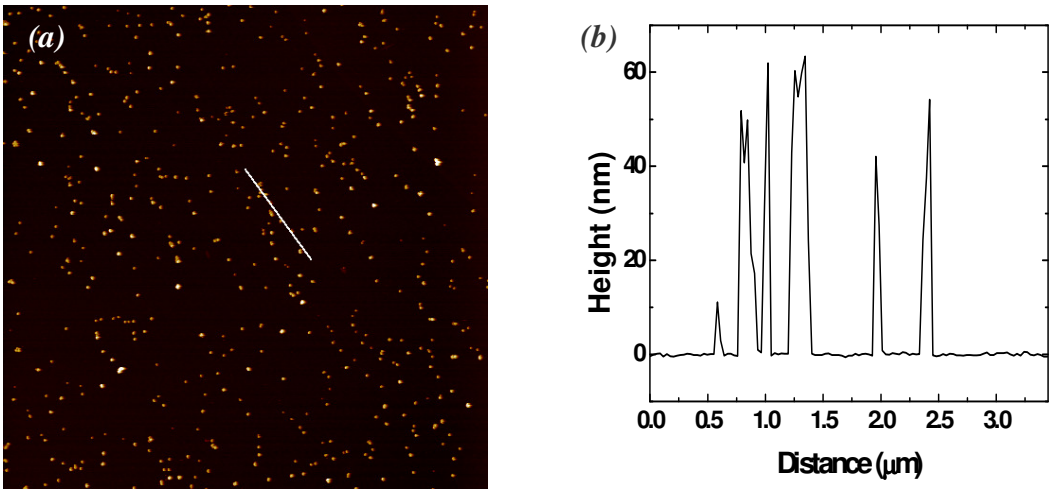

Figure 4-8. (a) 14.9 × 14.9 μm^2 topography scan of a sample incubated for 60 minutes in a 50 nm 5 g/L colloidal suspension with (b) height profile corresponding to the white line.

When the colloidal concentration was increased to 5 g/L (Figure 4-8) we find that the 50 nm colloidal particles incubated for 60 minutes have adsorbed onto the mica substrate in a dispersed manner (3.6% coverage), with almost no clustering evident. Height profiling (Figure 4-8b) measured the particle diameter at approximately 55 nm, within the tolerance of the manufacturers' specifications.

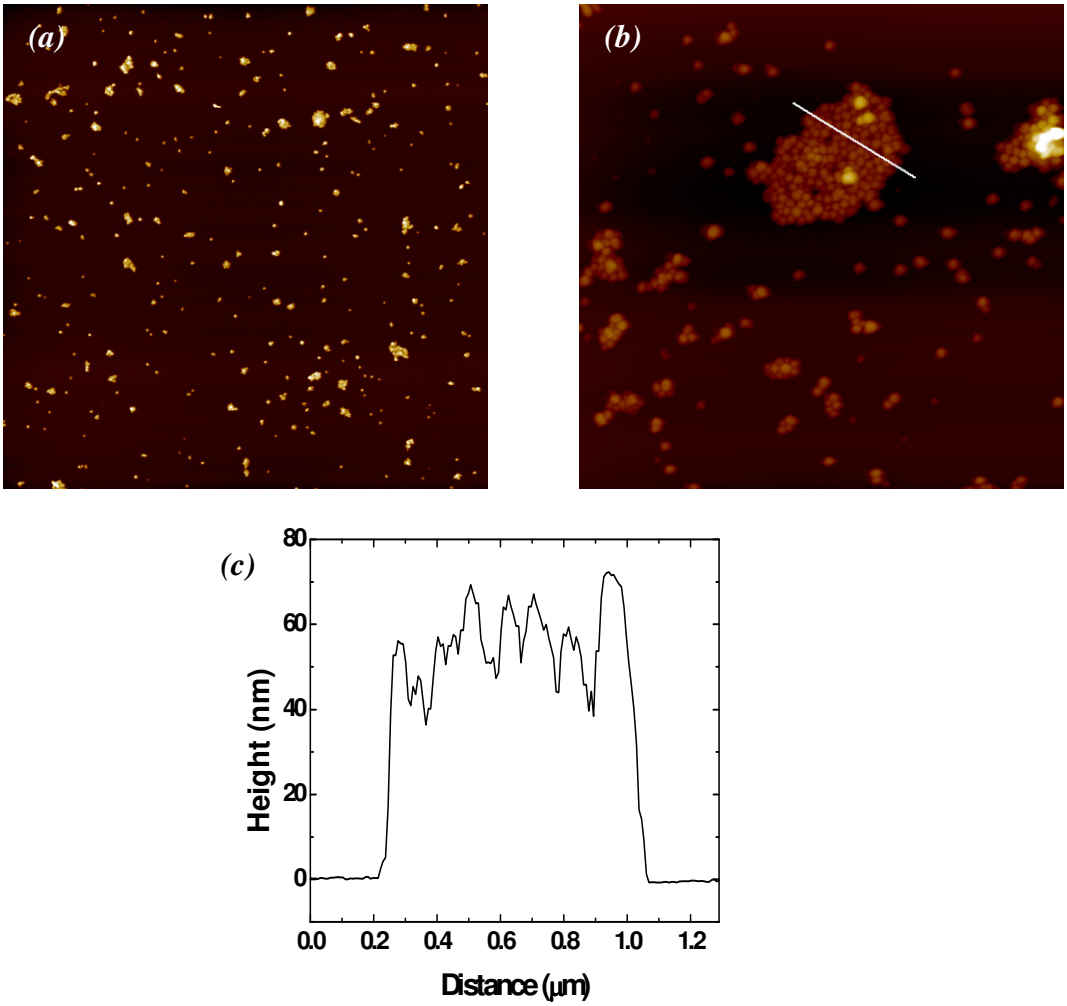

Figure 4-9. (a) 14.9 × 14.9 μm^2 topography scan of a sample incubated for 120 minutes in a 50 nm 5 g/L colloidal suspension. (b) 4 × 4 μm^2 topography scan with (c) height profile corresponding to the white line.

Increasing the incubation time to 120 minutes, we observe in Figure 4-9 that the silica colloidal nanoparticles start to exhibit some clustering on the substrate, with surface coverage still being comparable (3.9% for the 120 minute sample) to that of the 60 minute sample. The cluster structure of the 50 nm particles exhibits a close packed configuration with some indication of limited hexagonal packing. Height profiling of the clusters suggests a monolayer structure.

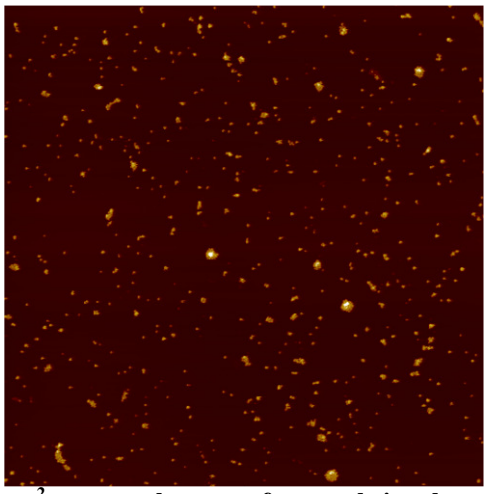

Figure 4-10. A 14.9 × 14.9 μm^2 topography scan of a sample incubated for 24 hours in a 50 nm 5 g/L colloidal suspension. Z range 90 nm.

For the 24 hour incubation time samples in Figure 4-10 we again see that the 50 nm silica colloidal particles are distributed across the surface, with a combination of some localised clustering and isolated particles. The area coverage and adsorbed volume measurements for all three incubation times appear to be similar, as shown in Table 4-3.

Table 4-3. Comparison of topography properties with respect to increasing incubation times of the 5 g/L 50 nm colloidal suspensions

Incubation Time	Area Coverage (%)	Adsorbed Volume (μm^3)
60 minutes	3.6	0.214
120 minutes	3.9	0.261
24 hours	4.0	0.277

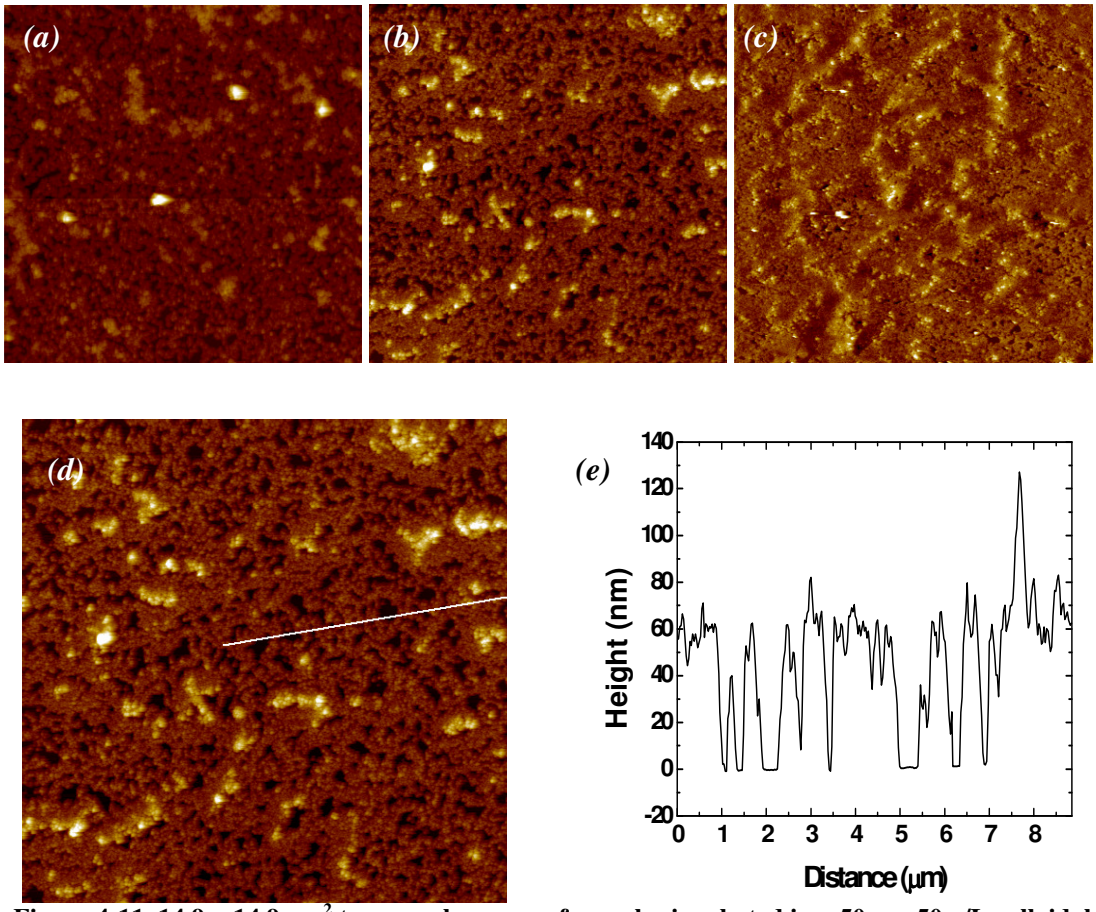

Figure 4-11. 14.9 × 14.9 μm^2 topography scans of samples incubated in a 50 nm 50 g/L colloidal suspension for (a) 60 minutes, (b) 120 minutes and (c) 24 hours. (d) Zoom of the 120 min topography scan with (e) height profile corresponding to the white line.

Figure 4-11 shows that increasing the concentration of the colloidal suspension to 50 g/L resulted in a higher level of coverage for all incubation times, with area coverage approaching 90% for the 24 hour sample. At this concentration we observed the formation of a very dense monolayer film across the substrate, with occasional bilayered particle patches on the topography images. Figure 4-11d shows a magnified image of the labyrinth structure present on the 120 minute incubation sample. There appeared to be little difference in the overall coverage of the 50 nm silica particles regardless of submersion time, as all films were nearly monolayer with small perforations.

4.6.3. 100 nm Silica Particles

As can be seen in Figure 4-12, adsorption of the 100 nm silica nanoparticles incubated in a 0.5 g/L colloidal suspension was almost non existent for all incubation times. For 60 minute incubation times there was no evidence of adsorbed particles on the mica substrate, even over several scans at different locations on the mica. For 120 minute and 24 hour incubation times there was only isolated particle adsorption on the surface of the mica.

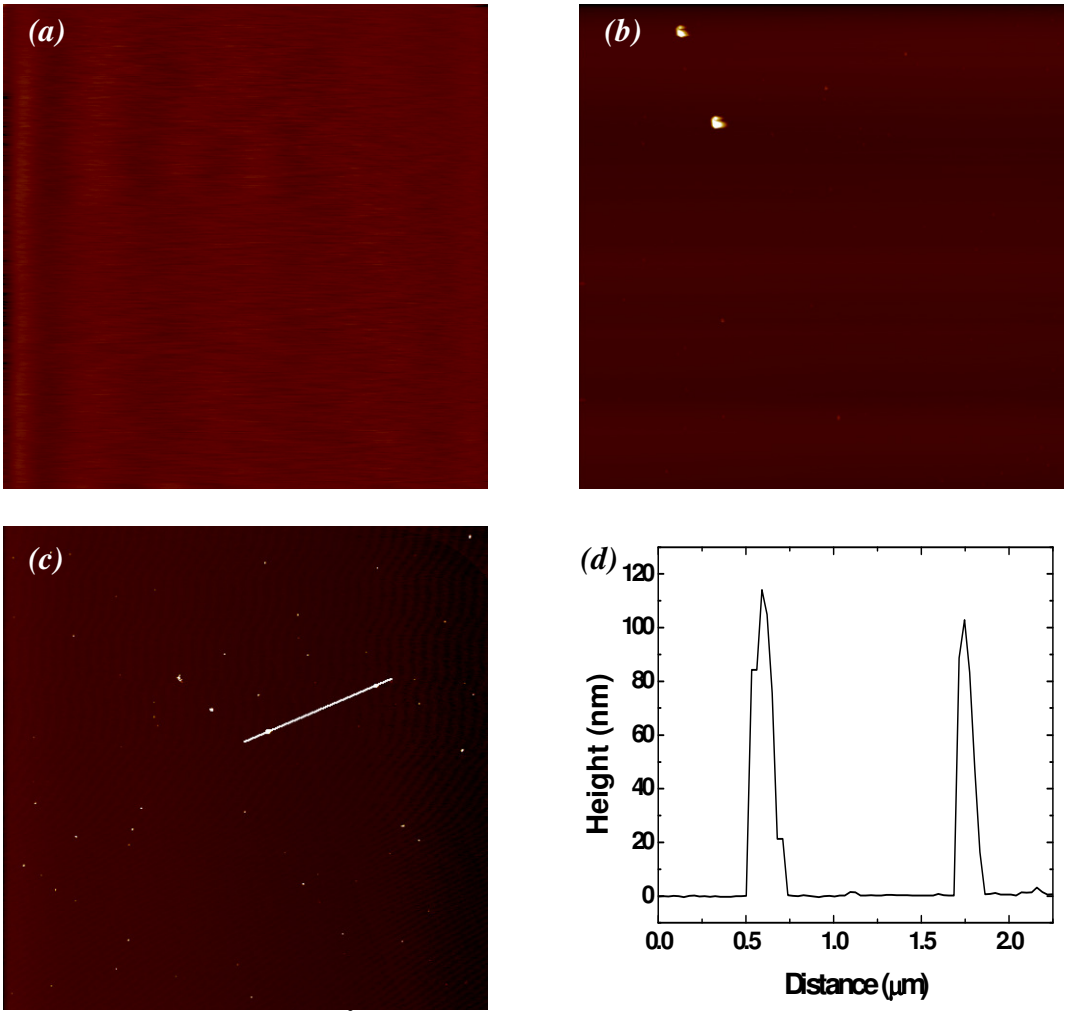

Figure 4-12. 14.9 × 14.9 μm^2 topography scans of samples incubated in a 100 nm 0.5 g/L colloidal suspension for (a) 60 minutes, (b) 120 minutes and (c) 24 hours, with (d) height profile corresponding to the white line in (c). Z range approximately 140 nm for all images.

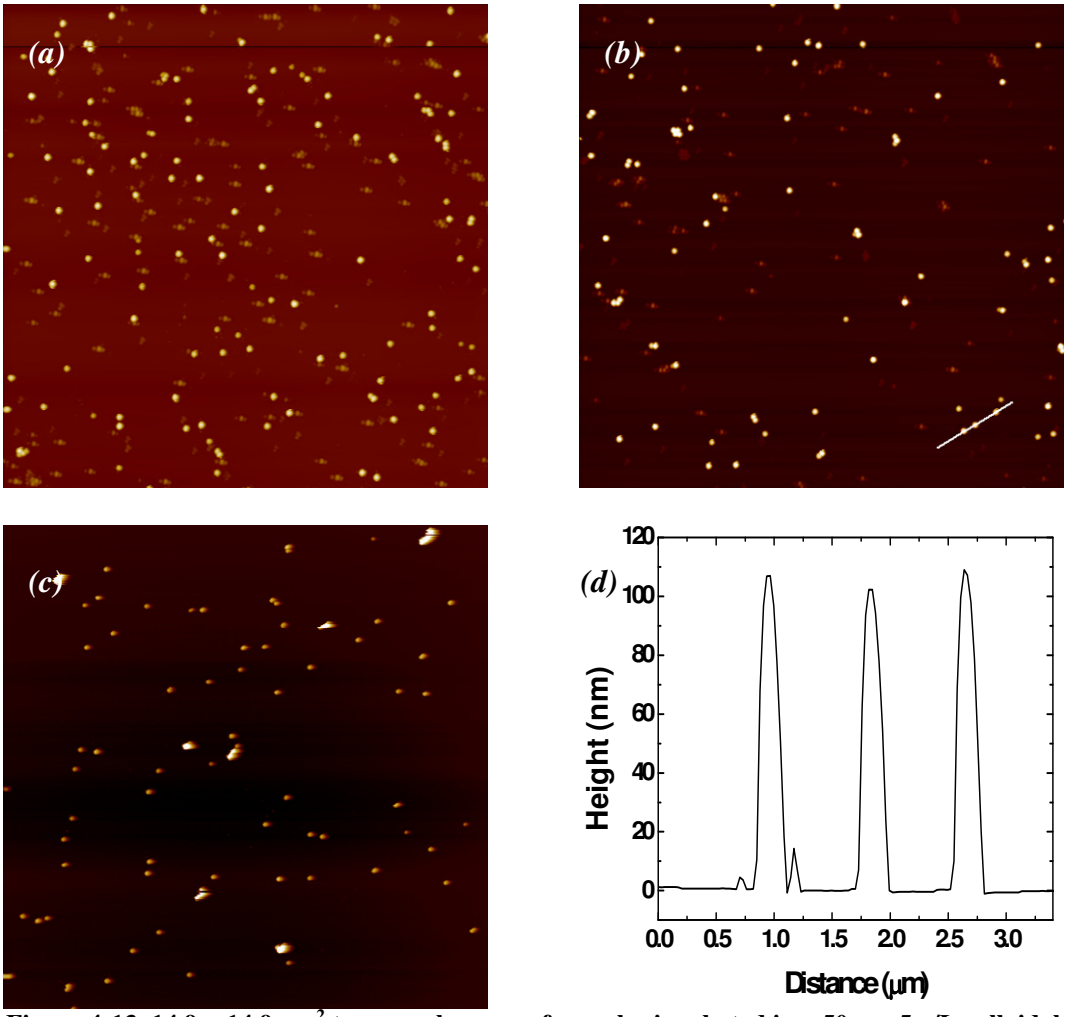

Figure 4-13. 14.9 × 14.9 μm^2 topography scan of samples incubated in a 50 nm 5 g/L colloidal suspension for (a) 60 minutes, (b) 120 minutes and (c) 24 hours. (d) Height profile corresponding to the white line in the 120 minute topography scan.

Figure 4-13 shows that for the 5 g/L colloidal suspension samples the 100 nm nanoparticle adsorption was relatively low (1-2% area coverage), with an isolated particle distribution on the surface of the mica substrate. We note that some minor desorption of the particles from the surface of the mica has taken place, with a small reduction in both the area coverage and adsorbed volume as incubation time increased (Table 4-4).

Table 4-4 Comparison of topography properties with respect to increasing incubation times of the 5 g/L 100 nm colloidal suspensions

Incubation Time	Area Coverage (%)	Adsorbed Volume (μm^3)
60 minutes	1.82	0.165
120 minutes	1.76	0.155
24 hours	1.05	0.110

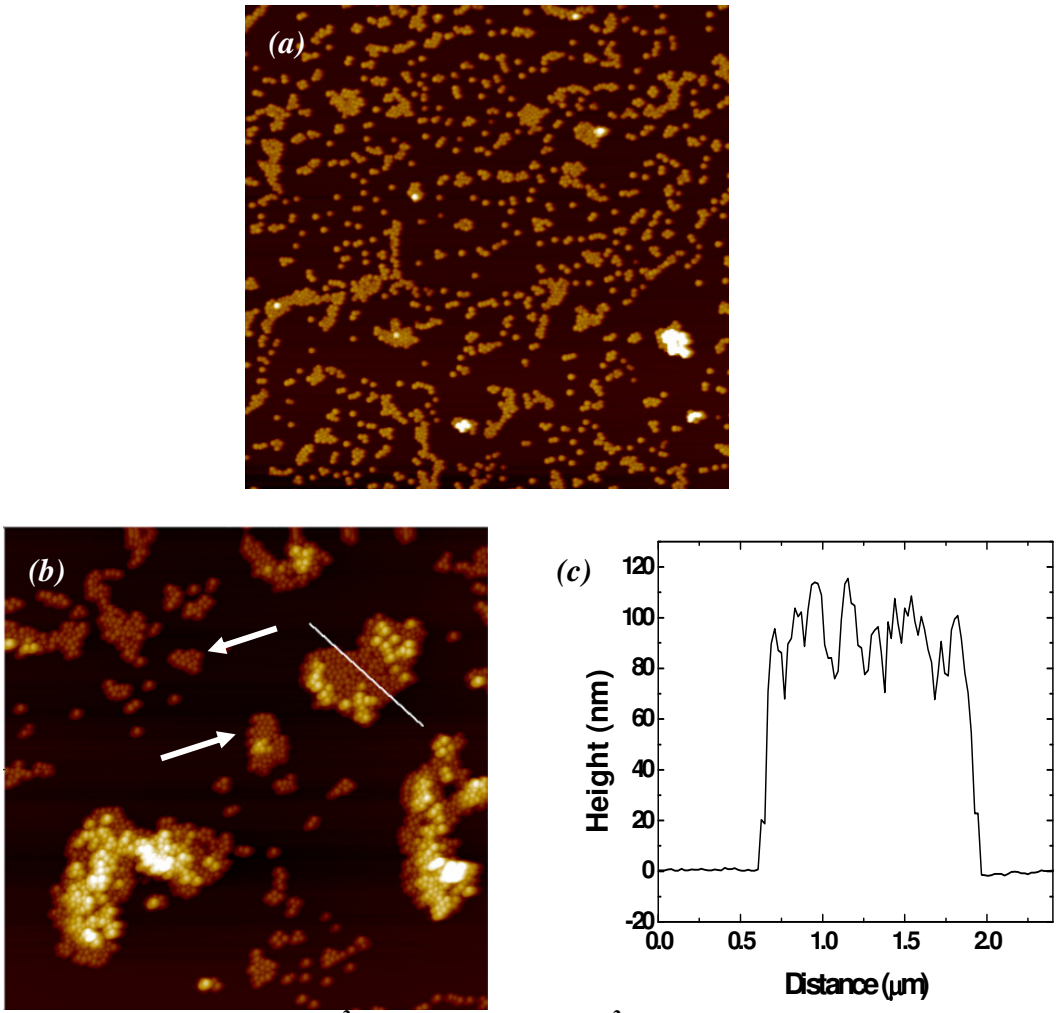

Figure 4-14. (a) 14.9 × 14.9 μm^2 and (b) 10.3 × 10.3 μm^2 topography scans of samples incubated in a 100 nm 50 g/L colloidal suspension for 60 minutes. The Z range is approximately 220 nm for both images. The white arrows indicate crystalline structures assembled on the surface. (c) Height profile corresponding to the white line.

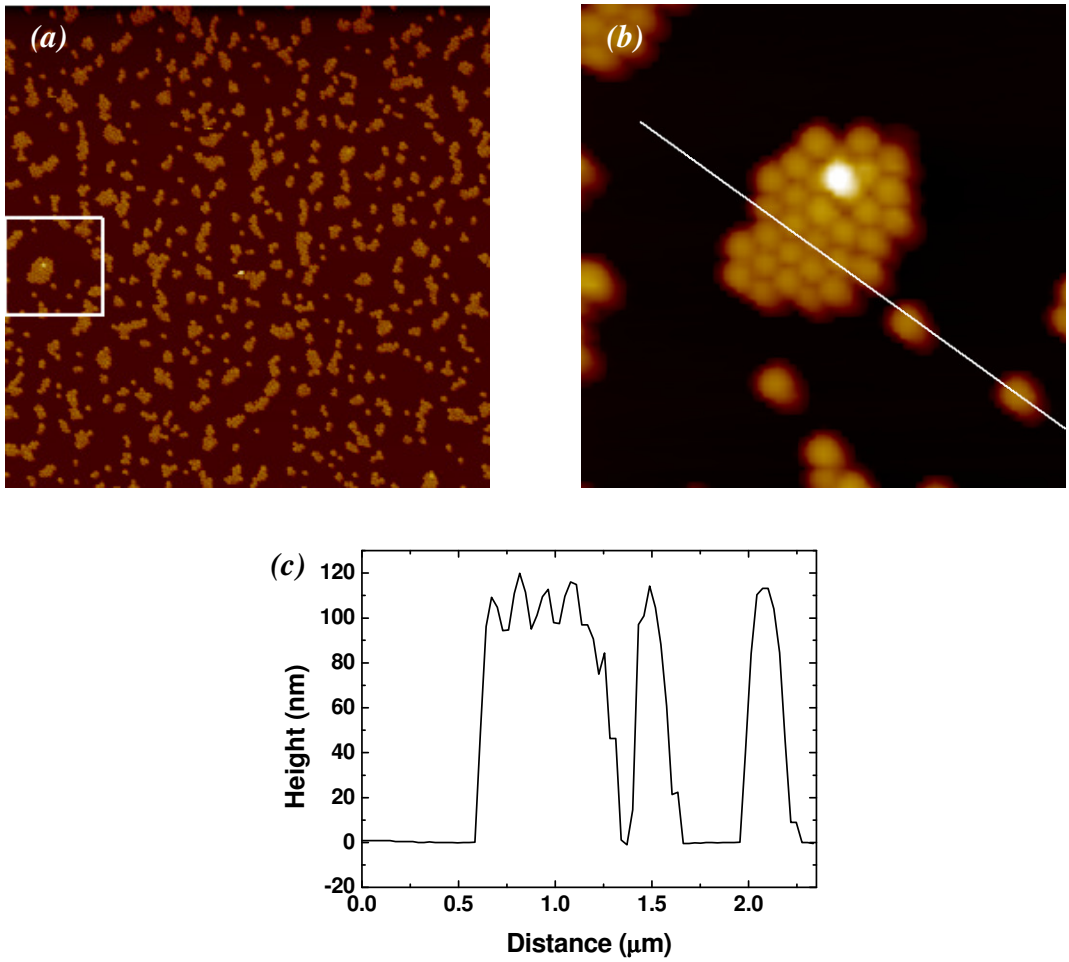

Figure 4-15. (a) 14.9 × 14.9 μm^2 topography scan of a sample incubated in a 100 nm 50 g/L colloidal suspension for 120 minutes. (b) Zoomed section corresponding to the white box with (c) height profile of the white line shown. Z range is approximately 250 nm.

Figure 4-14 shows the mica samples that were incubated in a 100 nm 50 g/L colloidal suspension for 60 minutes and 120 minutes. The particles have begun to form an array of small monolayer clusters of tightly packed particles. As the incubation times increased the structuring of the particles tended towards increased clustering, with a reduction in the number of isolated particles on the 120 minute samples compared to the 60 minute samples (Figure 4-15). We note that with the larger clusters of the silica colloids, the particles have formed close packed hexagonal structures. Figure 4-14b and Figure 4-15b show magnified sections from the 50 g/L concentration samples with height profiles confirming the particle size. The white arrows in Figure 4-14b indicate some of these hexagonally packed clusters observed on the mica substrate.

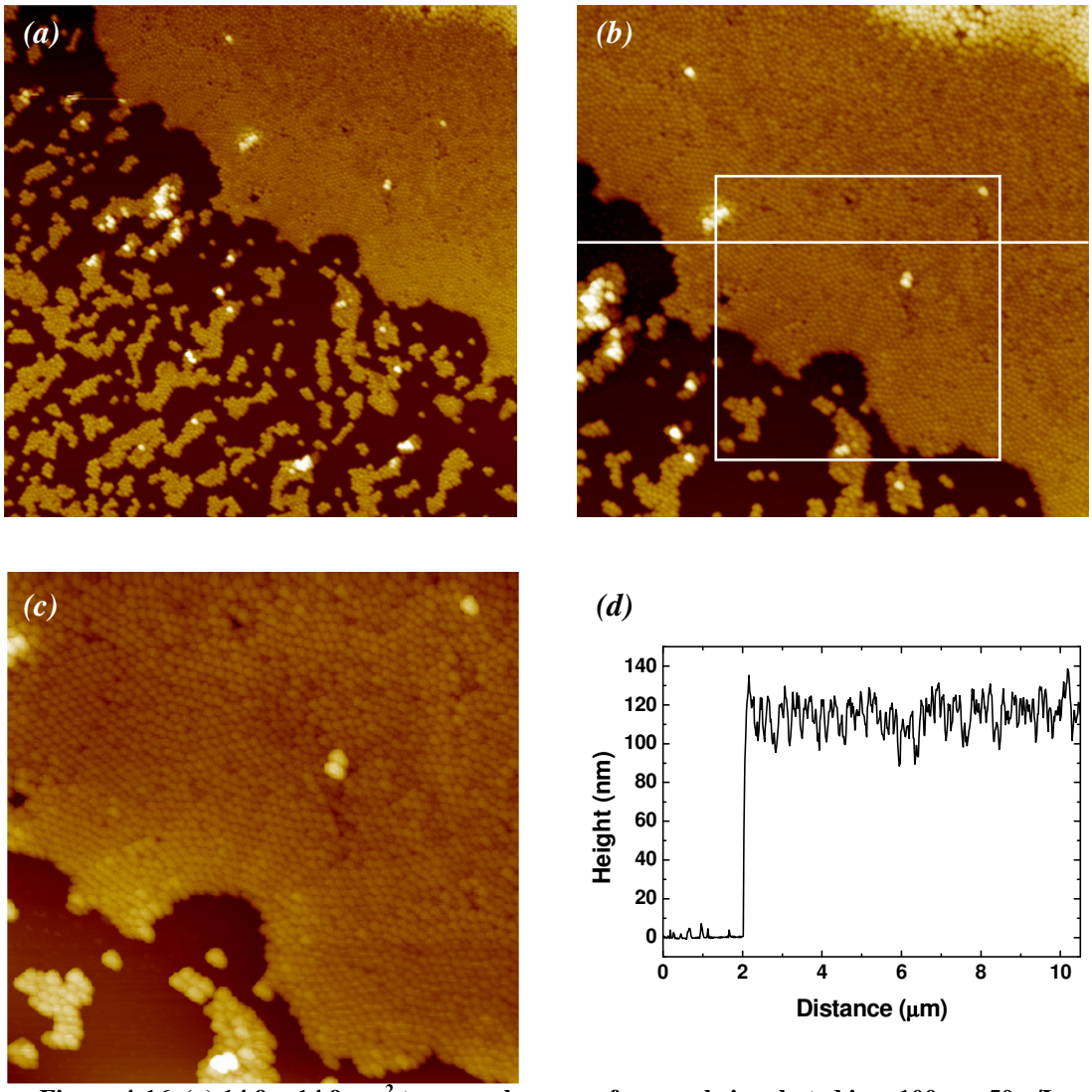

Figure 4-16. (a) 14.9 × 14.9 μm^2 topography scan of a sample incubated in a 100 nm 50 g/L colloidal suspension for 120 minutes. (b) 10 × 10 μm^2 topography of the same area showing grain boundaries in the monolayer. (c) 6 × 6 μm^2 topography scan of the previous topography image area marked with white box showing the finer detail of the crystalline structure. Z range is approximately 220 nm. (d) Height profile corresponding to the white line in the 10 × 10 μm^2 topography scan.

In some of the 100 nm samples that were incubated for 120 minutes we observed the formation of large areas of highly ordered clusters of colloidal particles. Figure 4-16 corresponds to one such 100 nm silica sample incubated for 120 minutes in a 50 g/L colloidal suspension. This sample showed isolated clusters of 100 nm particles and a large continuous monolayer structure. This large area was composed of numerous 2D crystallites of well ordered close packed nanoparticles. These appear to be

hexagonally packed (Figure 4-16c) in their structure, and their orientations vary across the film. Height profiling of the film confirmed a majority monolayer structure with visible bilayering occurring towards the top right of the image (Figure 4-16b).

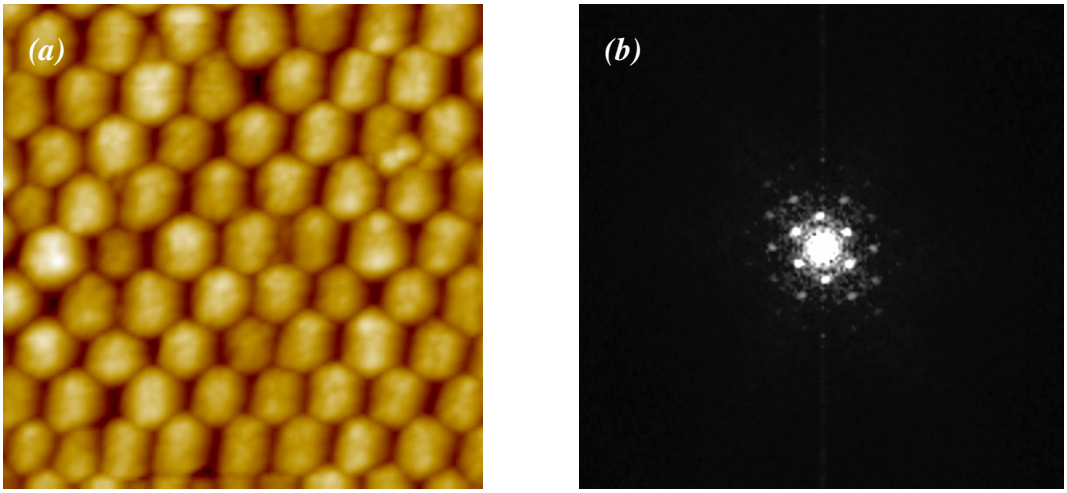

Figure 4-17. (a) Zoomed and flattened section of the crystalline area of the 120 minute topography scan and (b) corresponding 2D-FFT confirming a hexagonal structure with a packing distance of 100 nm.

A 2D-FFT of the structure (Figure 4-17b) revealed that the hexagonal structuring of the particles had a crystal lattice constant of approximately 100 nm indicating that the particles are indeed close packed throughout a given 2D crystallite. In Figure 4-18c, FFT measurements of the micro cluster also confirmed a packing distance of 100 nm.

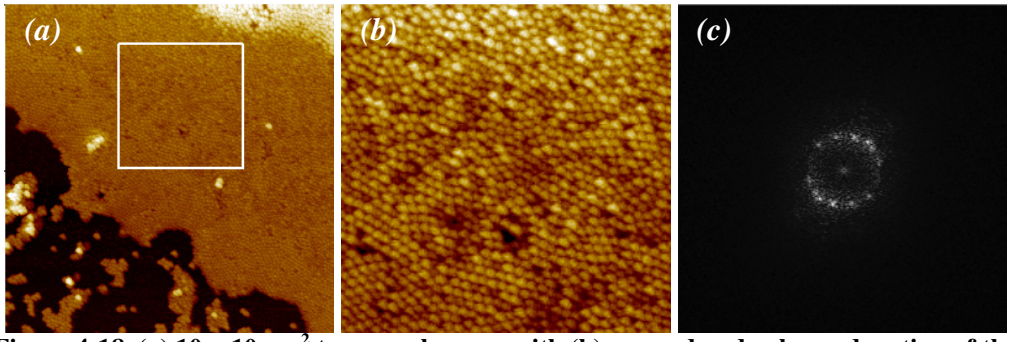

Figure 4-18. (a) 10 × 10 μm^2 topography scan with (b) zoomed and enhanced section of the image and (c) corresponding FFT of the zoomed section. The packing distance is approximately 100 nm.

Increasing the incubation time to 24 hours, we see in Figure 4-19 that the surface of the mica has now been covered with a film of colloidal particles that exhibit a high level of ordering. We observed patches of hexagonally packed particles surrounded by densely packed amorphous areas across the surface of the film. Height profiling of the film voids suggested a film thickness in excess of 200 nm indicating that the film is at least bilayer in its construction.

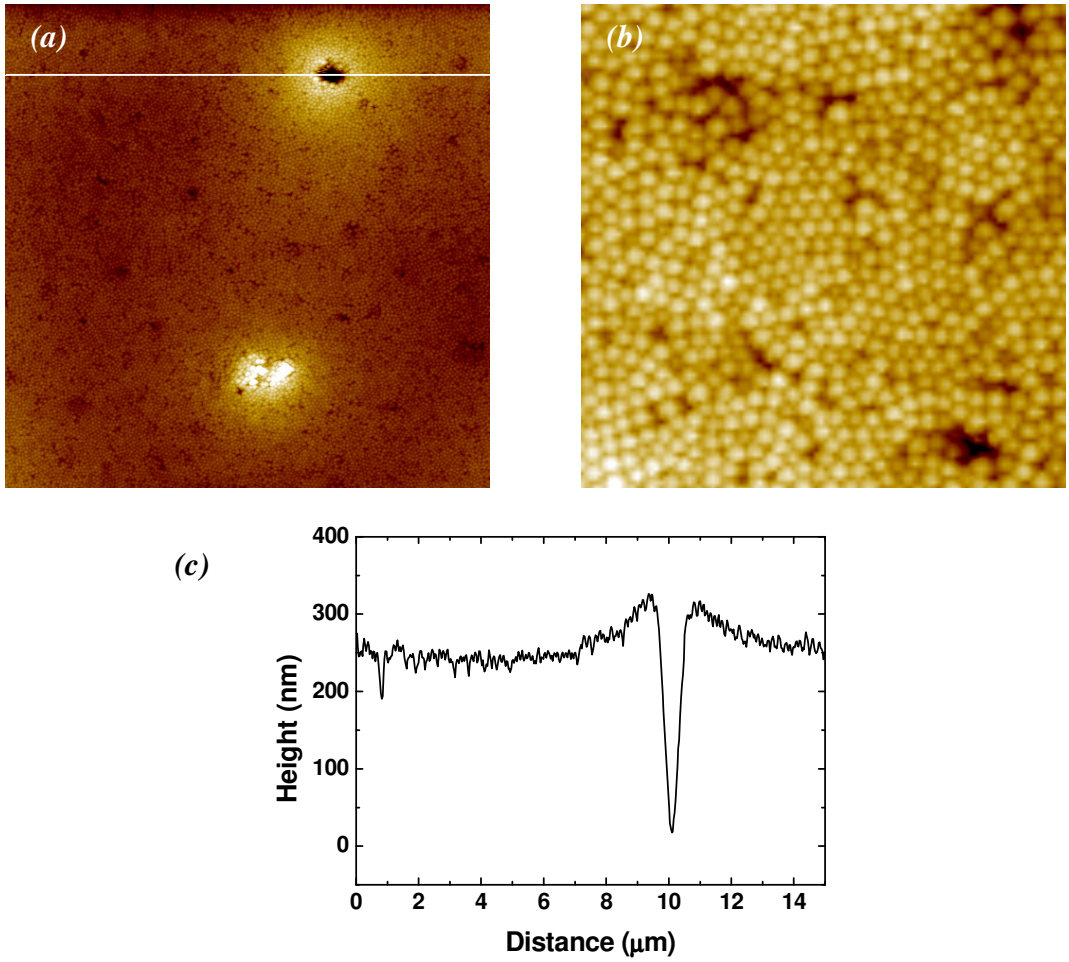

Figure 4-19. (a) 14.9 × 14.9 μm^2 topography scan of a sample incubated in a 100 nm 50 g/L colloidal suspension for 24 hours, with (b) zoom showing areas of hexagonal packing. (c) Height profile corresponding to the white line shown in the topography image (a).

4.7. Sample Overview

Figure 4-20 presents a topography overview of all the colloidal sizes and incubation times for the 0.5 g/L colloidal suspension. There is very little particle adsorption onto the substrate. There is some limited adsorption for longer incubation times and smaller particle sizes, in particular the 10 nm colloidal nanoparticles.

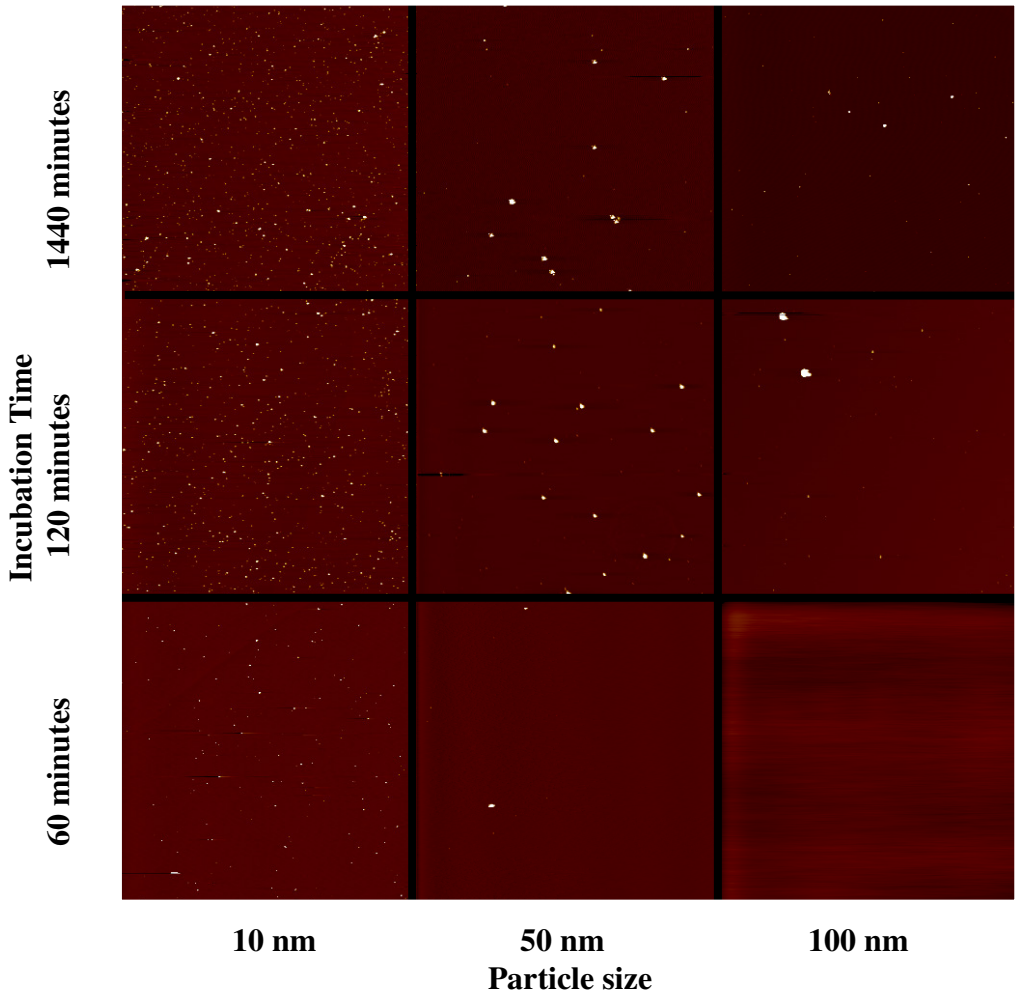

Figure 4-20. An overview of the 0.5 g/L samples in terms of particle size and incubation time. We can clearly see that for the majority of samples there is minimal coverage. All images are 14.9 × 14.9 μm^2.

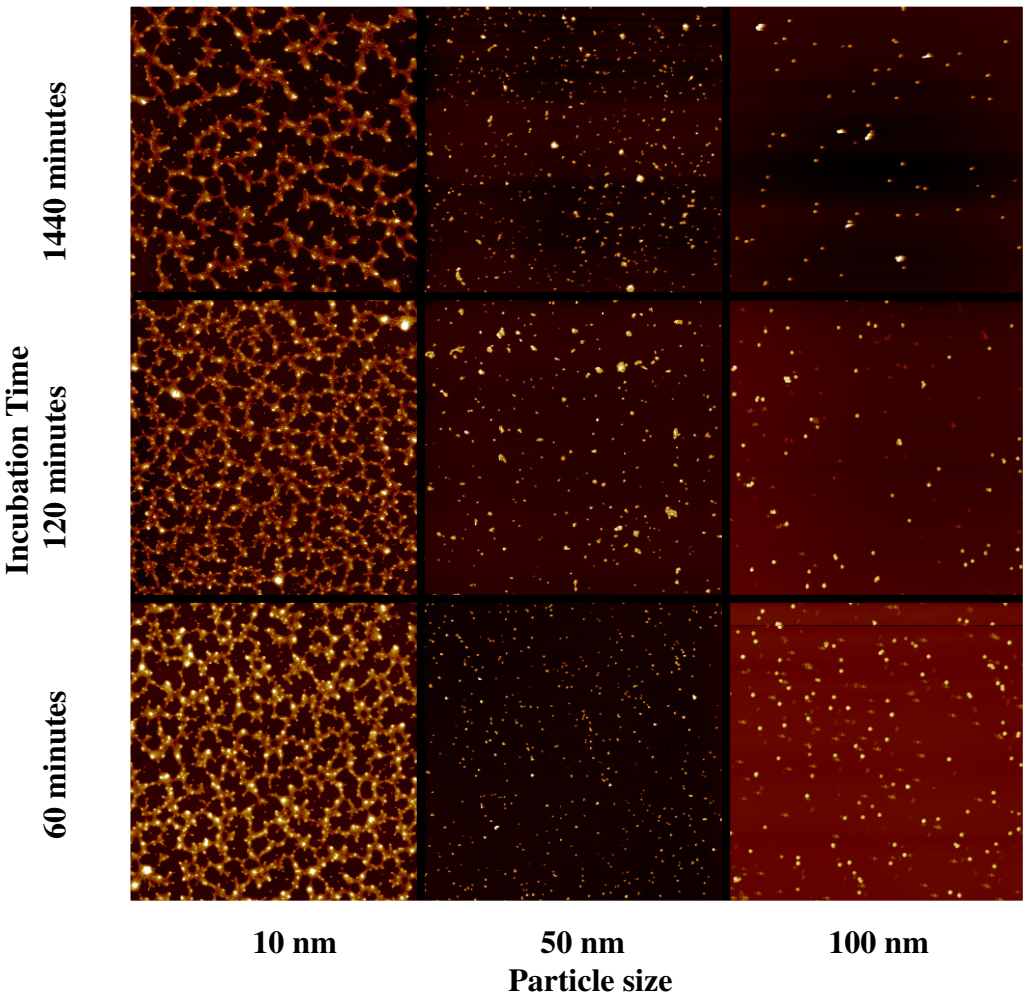

Figure 4-21. An overview of the 5 g/L samples in terms of particle size and incubation time. We observed that the 10 nm particles assembled into a unique 2D cellular structure at this concentration. All images are 14.9 × 14.9μm^2.

With the 5 g/L samples we encounter some interesting particle adsorption and structuring behaviour, most notably with the 10 nm particles. Figure 4-21 shows the 10 nm particles' distinct 2D cellular structuring across all incubation times. The 50 nm nanoparticles seem to configure from disperse, isolated particles at low incubation times, to patches of clustered particles at higher incubation times. Finally the 100 nm particles show isolated particles that are spread out over the substrate and lacking any discernable ordering in their distribution. Volume coverage measurements at this colloidal concentration suggest a relatively constant amount of colloidal material has adsorbed onto the surface for each particle size independent of the incubation period.

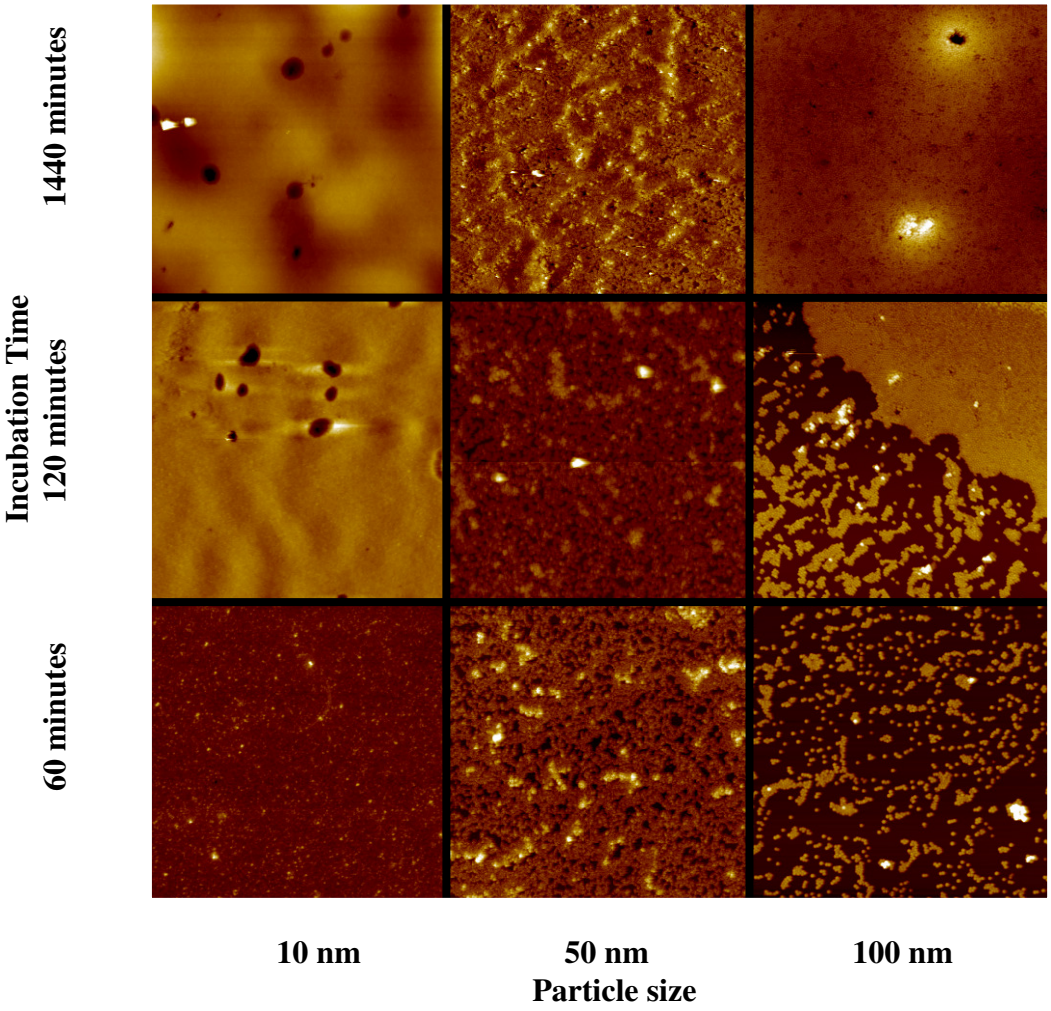

Figure 4-22. An overview of the 50 g/L samples in terms of particle size and incubation time. At this concentration total surface coverage is a dominant feature for the 10 nm and 50 nm particles. The 100 nm particles show increasing area coverage as a function of incubation time. All images are 14.9 × 14.9μm^2.

Figure 4-22 shows that at a concentration of 50 g/L it is the 100 nm nanoparticles that exhibit the most striking behaviour, with some very large, distinct areas of highly crystalline structuring of the nanoparticles. The 50 nm particles have created condensed monolayer films that are mostly amorphous with occasional crystalline structuring for all incubation times. The 10 nm particles have formed dense multilayer films across the substrate with little discernable features for all incubation times.

4.8. Analysis and Discussion

4.8.1. Discussion of Particle Coverage and Adsorption Behaviour

Volume fraction effects

Figure 4-20 to Figure 4-22 illustrate that, with each increase of colloidal concentration used, there is a distinct change in the amount of silica particle material adsorbed onto the surface of the mica substrate. For 0.5 g/L only the 10 nm particles have an appreciable amount of coverage on the sample substrate. For 5 g/L we see the formation of disperse monolayer distributions of particles for 50 nm and 100 nm particles, and the 10 nm particles formed more complex 2D cellular structures. At 50 g/L both the 10 nm and 50 nm samples formed continuous films across the mica substrate, while the 100 nm particles assembled into clusters that, with increasing incubation time, grew in size eventually forming large monolayer films. This is a system where both the silica colloidal particles and the sample substrate (freshly cleaved mica) possess a negative charge when in solution. Due to the similar electrostatic charge, the most likely adsorption mechanism is via short range van der Waals attractive forces. Previously in chapter three we discussed the effect of volume fraction on the Debye length of the electrostatic double layer (EDL). It has been shown [36, 37] that colloidal concentration can affect the Debye length of the electrostatic double layer (EDL) at high particle volume fractions. This compression in the EDL will facilitate attractive van der Waals interactions between the particle and substrate due to the deceased range of the electrostatic repulsion. Moreover, this effect is intensified at the surface where the localised particle concentration is higher than in the bulk suspension due to the localised adsorption; facilitating even higher adsorption densities due to the reduced electrostatic repulsion until the system reaches maximum coverage. From this we can understand the behaviour of the particles at the highest colloid concentration, 50 g/L. As seen in Figure 4-22 the formation of thick multilayer films has occurred for both the 10 nm and 50 nm particles, and bilayering in the 100 nm particles incubated for 24 hours. We attribute this effect to the formation of bilayers due to the second layer of particles being able

to approach the substrate sufficiently close to also establish van der Waals attractive forces, as shown schematically in Figure 2-10.

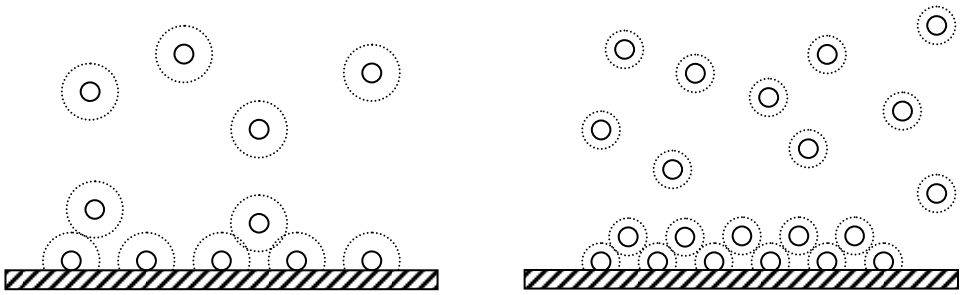

Figure 4-23. Schematic diagram of the effect of electrostatic double layer compression has on the adsorption of colloidal particles. The reduction in the Debye length of the particles on the right due to the increased volume fraction has allowed them to diffuse closer to the surface than the particles of a lower volume fraction, and subsequent longer Debye length (left).

Kinetic effects

Successful adsorption of the silica nanoparticles onto the mica substrate will only occur if a particle has sufficient kinetic energy to overcome the aforementioned repulsive electrostatic force that exist between the mica and the silica colloidal particle, and approach the surface of the mica sufficiently close to become attracted by the van der Waals forces and subsequently adsorbed. This event only occurs for a small portion of particles in the system, as defined by the Maxwell–Boltzmann distribution [38]. At low colloidal the probability of such events is negligible; resorting in only a small percentage of particles successfully adsorbing onto the mica substrate. With increasing concentration of the colloidal suspension the probability of a particle with sufficient kinetic energy colliding and adsorbing on the mica surface increases, as we have observed with the change from 0.5 g/L to 5 g/L and eventually 50 g/L where rapid saturation of the surface area occurs due to the high probability of successful adsorption to the surface. We believe that it is the kinetics effects rather than the volume fraction effects that result to the poor surface coverage of the 0.5 g/L samples, as the decrease in the Debye length from the 0.5 g/L to the 5 g/L colloidal suspension samples would be relatively small, but the increase in the amount of adsorbed material from 0.5 g/L to the 5 g/L is significantly large.

We also note that the volume of material adsorbed scales as a function of particle size at low concentrations. In Figure 4-20 we see that the 10 nm particles adsorb in significantly higher numbers compared to the 50 nm, while adsorption of the 100 nm colloidal particles is almost nonexistent. From this observation it is apparent that the particle size is also a factor in the adsorption behaviour of the nanoparticles. We consider two possible explanations for this. Firstly, we take into account that the colloidal suspensions were diluted by volume fraction. If we consider the volume of one 100 nm particle ($\approx 4\times10^6$ nm^3), and that a 10 nm particle occupies a volume of $\approx 4\times10^3$ nm^3, then for a given volume fraction the *number* of particles differs by several orders of magnitude. This is an important aspect, as it directly connects to our previous discussion on the probability of a particle successfully adsorbing onto the substrate with particle size. As such, even for equivalent volume fractions the probability of adsorption varies with particle size. Secondly, we must consider how the size affects the particle diffusion rate to the surface. Using the Einstein-Smoluchowski equation [39] which calculates the relaxation time (τ_R) it takes a particle to diffuse a distance equal to the particles radius, we can investigate how size affects the diffusion rate of the particle to the surface of the substrate.

$$\tau_R = \frac{6\pi\eta R^3}{k_B T} \qquad \textbf{4-1}$$

where η is the viscosity of the suspension, R is the colloidal particle radius and k_BT is the thermal energy. This equation shows that the diffusion rate of a particle is proportional to the cube of the particle radius. As such we would expect the 10 nm particle to diffuse 1000 times faster than the 100 nm particles. For a system at room temperature ($\approx$ 20 °C) the diffusion times are 4.66 μs for a 10 nm particle and 4.66 ms for a 100 nm particle. Due to the lower particle concentrations of the 0.5 g/L samples, the influence of kinetics effects (i.e. diffusion and probability of adsorption) is most evident at this concentration.

For the samples incubated in a 5 g/L colloidal suspension we find that the volume of material adsorbed onto the surface is relatively constant for all incubation times, indicative of a system in equilibrium. Some minor variation in the area and volume of material adsorbed was observed, although this is likely due to desorption effects.

4.8.2. Discussion of Particle Structuring and Patterns

The 100 nm particles at high concentrations were observed to cluster in well ordered structures, in particular we note that at 50 g/L for all incubation times the particles were observed to form close packed structures, in many instances well ordered hexagonal packing. This behaviour was only observed in a minority of the 50 nm samples and was nonexistent for all 10 nm samples. As this structuring is predominantly found to have occurred with only the 100 nm particles it would appear to be a size dependent phenomenon. We attribute this phenomenon to lateral capillary force effects. As the remaining liquid film dries on a sample, the receding liquid layer eventually breeches the top of the colloidal particles (Figure 2-10). The now partially immersed particles experience an attractive force due to the deformation of the liquid surface and the induced asymmetry of the contact line at the surface of the particle.

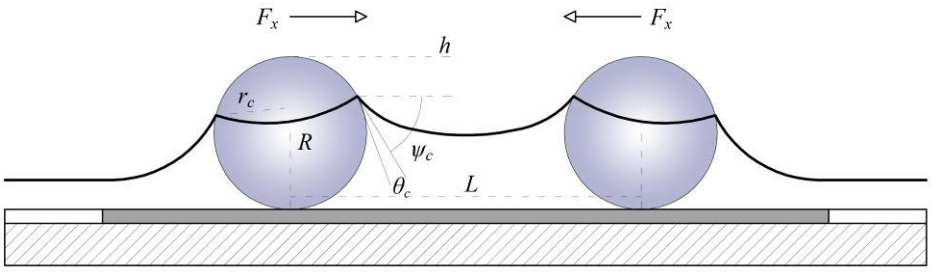

Figure 4-24. Schematic and equation of two spheres partially immersed in a liquid layer on a horizontal solid substrate under the influence of an attractive capillary force. Refer to chapter 2 for details on the parameters.

Denkov *et al.* [21] proposed a mathematical expression of the free energy of capillary interaction which allows us to evaluate the effective capillary energy interaction experienced by the colloidal particles. In chapter three we raised some concerns about the reliability of this model for nanometer sized particles. Nevertheless in the absence of a suitable alternative we have chosen to use it again to perform comparative studies between the effects of capillary interactions for

different sizes particles. The free energy of the capillary interaction, ΔW, can be expressed as:

$$\Delta W \approx 2\pi\sigma r_c^2(\sin^2\psi_c)R/(L-2R) \qquad \textbf{4-2}$$

where σ is the surface tension of the liquid, r_c is the radius of the three-phase contact line at the particle surface ($r_c = [h(2R-h)]^{1/2}$), ψ_c is the mean meniscus slope angle at the contact line ($\psi_c = \arcsin(r_c/R)-\theta_c$, where θ_c is the contact angle of the bulk liquid), h is the height of the liquid layer from the top of the particle ($2R$), R is the particle radius and L is the distance between the particles. Substituting values for the surface tension (0.072 N/m) and contact angle between water and silica (22°) [40] we are able to evaluate the free energy capillary interactions, ΔW, over the range of liquid film thicknesses, h, for a fixed particle spacing. We found that the maximum energy of the capillary action is exerted when the liquid height is equal to the radius of the particle immersed (Figure 4-25).

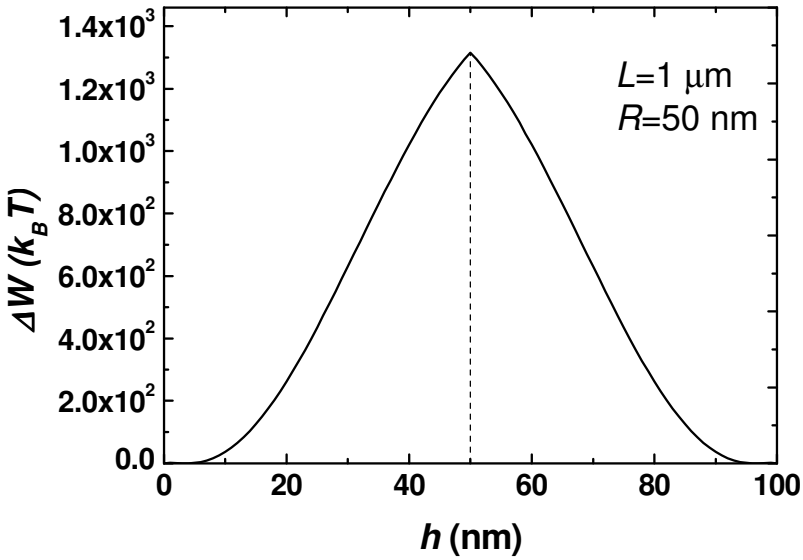

Figure 4-25. Graph of the energy of capillary attraction (ΔW) as a function of the receding liquid layer (h) for a 100 nm particle.

Knowing this we calculated values for the maximum capillary action energy for all three colloidal sizes as a function of increasing particle separation (Figure 4-26).

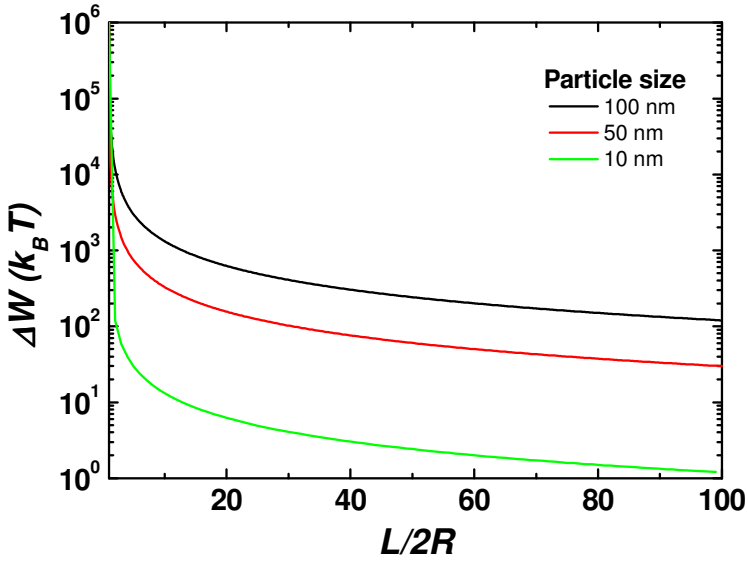

Figure 4-26. Graph of the energy of capillary attraction (ΔW) as a function of the normalised particle separation ($L/2R$) for all particle sizes.

Values for the van der Waals interaction energy between the particles and the substrate were calculated using the surface element integration (SEI) [41] given in Equation 4-3:

$$W_{vdW}^{SEI} = -\frac{A}{6}\left[\frac{R}{D} + \frac{R}{D+2R} + \ln\left(\frac{D}{D+2R}\right)\right] \qquad \textbf{4-3}$$

where A is the Hamaker constant for the silica-water-mica, calculated using the Liftshitz theorem to be 7.754×10^{-21} J, R is the particle radius and D is the separation distance (0.4 nm for a particle in "contact" with the surface). The SEI provides a more accurate determination of the interaction energy than the sphere – surface equation in figure 2-2 by more accurately modelling the effects of particle curvature of smaller particles. Van der Waals interaction energies of -37.3 k_BT for the 100 nm particles, -18.1 k_BT for the 50 nm particles and -3.05 k_BT for the 10 nm were calculated. It is clear that the larger particles will experience an attractive capillary force of several orders of magnitude greater than that of the van der Waals adsorption force, even over large particle separation distances. The 10 nm particles

will however only experience sufficiently strong capillary forces over a shorter range of particle separation distances. As the maximum capillary interaction energy is generated at a liquid film height equal to the particle radius, this means that for a 10 nm particle the induced lateral capillary forces will only reach their maximum in a liquid film of 5 nm. However, experimental studies of aqueous thin film stability on completely wettable surfaces such as freshly cleaved mica have yielded approximate values for film thickness before rupture to be approximately tens of nanometers [16, 42, 43]. Therefore it would be unlikely that the film will reach a thickness suitable for the 10 nm particles to experience effective lateral capillary attraction. It is more likely that it will rupture well before this thickness. Similarly the 50 nm particles may only experience a partially effective lateral capillary force leading to some isolated patches of ordered structuring. The 100 nm particles however are of sufficient size that a stable thin film of liquid can exist between the neighbouring particles to facilitate formation of large areas of well ordered structuring of the particles.

The highly ordered structuring of the 100 nm silica particles was only observed for samples incubated in the highest concentration (50 g/L). At lower concentrations for this incubation time only isolated particles were observed for all incubation times. As our previous discussion showed, the attractive capillary force between neighbouring particles decays rapidly with particle distance. As higher absorption densities of the colloids onto the substrate will lead to, on average, smaller separations between the particles, the amount of adsorbed material on the surface will dictate the magnitude of this capillary interaction, ultimately determining the level of particle ordering. It is only at a concentration of 50 g/L that the 100 nm particles adsorb onto the mica in sufficiently high numbers to facilitate the formation of close packed structuring via lateral capillary forces.

For the 10 nm silica particles incubated in a 5 g/L colloidal concentration, we observed that for all incubation times a distinct 2D cellular network of particles was formed. This microstructure is reminiscent of dewetting morphologies where a thin film of material reaches a critical thickness, ruptures and coalesces into distinct 2D

cellular structures [33, 44, 45]. This cellular structure is evident regardless of incubation time, suggesting that the dewetting process dominates the ordering of the particles at this concentration. As previously stated, the highly hydrophilic nature of both the silica and mica surfaces facilitates the presence of a thin layer of water. If this film reaches a critical thickness then its stability will become compromised. This leads to the film abruptly rupturing in a phenomenon known as dewetting. Dewetting can occur via two mechanisms, spinodal and nucleation dewetting. Spinodal dewetting is caused in a thermodynamically unstable system where thermal fluctuations become amplified until the eventual spontaneous rupture of the thin liquid film. Nucleation dewetting occurs either due to external disturbances (e.g. airborne particles) rupturing the film in localised areas over a short time frame (heterogeneous) or due to local fluctuations in thermal energy allowing the liquid to overcome the potential barrier for nucleation of a dry spot, leading to the formation of a hole, and is characterised by having a continuous breakout of holes on the surface throughout the time frame (homogeneous). As previously mentioned experimental studies of aqueous thin film stability on completely wettable surfaces such as freshly cleaved mica have yielded an approximate value for the minimum film thickness before dewetting to occur in the region of tens of nanometers. Height profiling of the cellular network gives an approximate film thickness of 20-30 nm, well within the range of experimentally evaluated critical film thickness values. In order to elucidate the mechanism by which our samples have dewetted we performed 2D-FFT measurements of the formations (Figure 4-3d) and found the existence of a characteristic length scale to the cellular structure. This attribute is usually associated with dewetting via a spinodal process, due to the amplified thermal fluctuations possessing a characteristic wavelength. Our system however is thermodynamically stable with a negative effective Hamaker constant [25] $A = A_{ll} - A_{sl} = 4 \times 10^{-20} - 7.06 \times 10^{-20} = -3.06 \times 10^{-20}$ J < 0. As such this system should only experience nucleation dewetting, which has no associated characteristic length in its structure. We explain this apparent contradiction by considering a third mechanism of dewetting presented by Sharma and Mittal [46]. They proposed that density variations within the evaporating thin film affected its stability behaviour. Surface instabilities are caused by the fluctuations of local density, which are coupled to the local film thickness and

produce a gradient of the van der Waals force. For the case where the film is considered spinodally stable ($\Phi(h) > 0$) it was shown that these van der Waals gradients could sufficiently induce destabilisation and subsequent dewetting reminiscent of spinodal dewetting. As the film of colloidal suspension thins, the solid content of the colloidal particles may cause localised variations in the density of the suspension due to the high concentration. The colloidal density can be calculated using the equation $\rho_{CS} = \phi\ \rho_C + (1-\phi)\ \rho_L$ where ρ_{CS} is the colloidal suspension density, ρ_C is the colloidal particle (silica) density, ρ_L is the liquid density and ϕ is the colloidal volume fraction. This formula clearly shows how the increase in the colloidal volume fraction (due to the decrease in suspension liquid through evaporation) directly affects the density. Variations in the particle concentration due to random thermal fluctuations would create density variations generating the aforementioned van der Waals gradients leading to the film rupture. An alternative mechanism for spinodal like structuring has been postulated by Moriarty [44] and Tanaka [47] where studies of the viscoelastic phase separation in binary systems have shown that in the latter stages of drying the effective viscosity of the nanocrystal fluid dramatically increased. It was suggested that this phenomenon could provide an alternative mechanism by which spinodal like structuring could occur.

Having observed two extremes in structuring morphology for the 100 nm and 10 nm particles, the 50 nm particle samples appear to lack any distinct characteristics to their structure. We observe that at low concentrations (0.5 g/L) the particles have dispersed randomly across the surface of the mica at very low density. At intermediate concentrations (5 g/L) the particle distribution is a mixture of dispersed single particles and isolated clusters of particles with an amorphous structure. At high concentrations (50 g/L) we see the formation of monolayer and bilayer films of amorphously structured particles that increase in density with incubation time.

In order to ascertain if the 5 g/L samples were indeed randomly dispersed particles we performed statistical measurements. While 2D-FFT techniques have been used to provide evidence and determine characteristic length scales in structures, Voronoï

tessellations were found to indicate the existence of entropically favourable configurations that may exist in the structuring of the samples, providing a statistical measurement of the degree of disorder in the system. There are two significant quantities associated with such tessellations: the variance (μ_2) and the entropy (S) of the distribution of the number of cell sides. The entropy measurement ($S = -\Sigma_n P_n \ln P_n$ where P_n is the probability of a cell having n sides) is based on the work of Rivier and Lissowski [48] who associated the possible distributions of cells in a system with the tendency of a system to configure itself to maximise entropy. As a natural system will tend towards maximising its entropy we are able to determine how close a system is to its most entropically favourable state. In order to provide reference values for these measurements, Voronoï tessellations of completely random (Poisson) distributions have been measured by other groups [49] and provided values of $\mu_2 = 1.78$ and $S = 1.71$. Using our own Matlab routine we evaluated the variance and entropy for the 50 nm samples created using the 5 g/L colloidal suspension for all incubation times. The Voronoï tessellations were constructed by identifying each separate particle and drawing an imaginary line between each particle and its nearest neighbour. A perpendicular bisector is then drawn through these imaginary lines forming a polygon cell surrounding the particle. The number of faces on the polygon corresponds to the number of nearest neighbours that particle has.

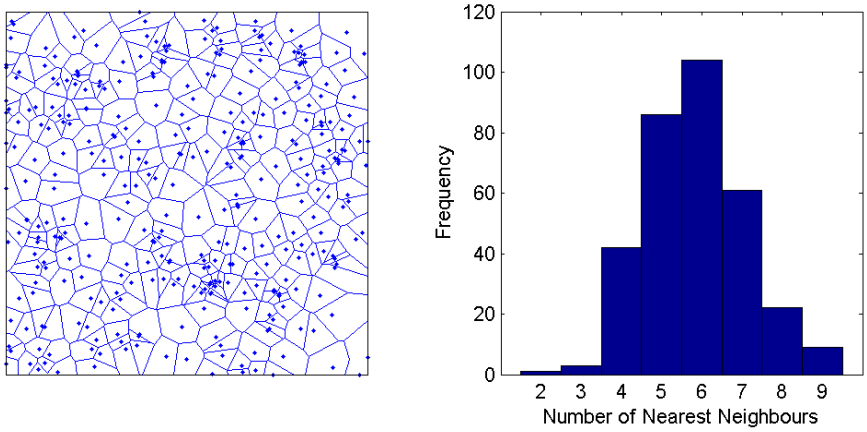

Figure 4-27. Voronoï diagram of a sample that has been incubated for 60 minutes in a suspension of 50 nm 5 g/L silica nanocolloidal suspension. μ_2 = 1.356 and S =1.544.

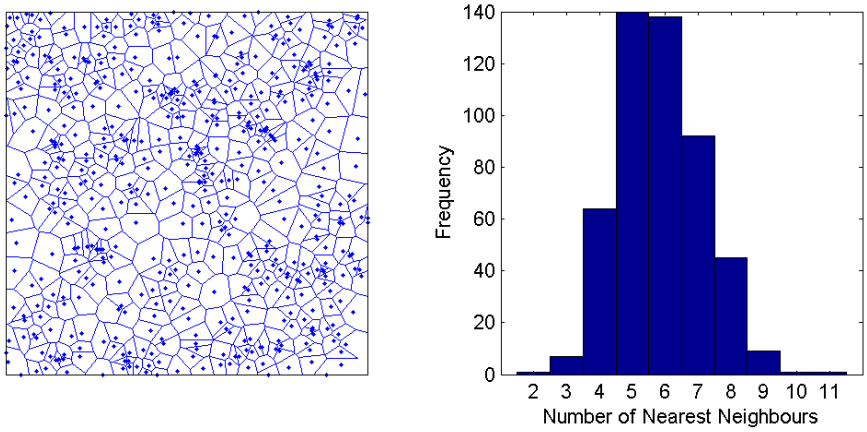

Figure 4-28. Voronoï diagram of a sample that had been incubated for 120 minutes in a suspension of 50 nm 5 g/L silica nanocolloidal suspension. μ_2 = 1.421 and S =1.619.

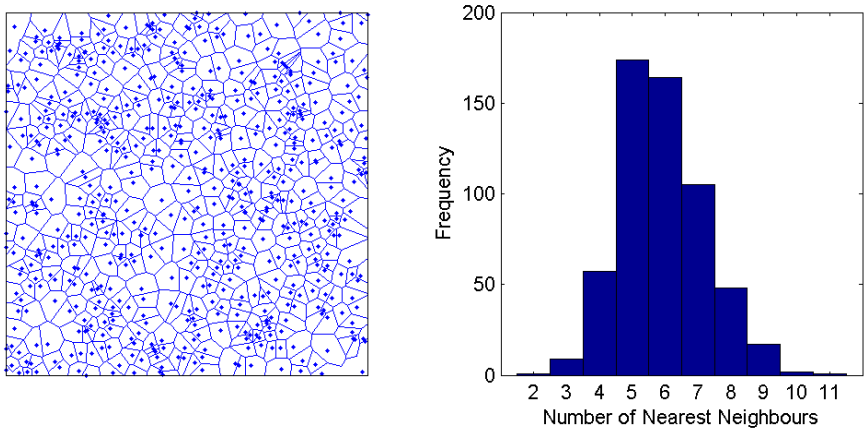

Figure 4-29. Voronoï diagram of a sample that had been incubated for 1440 minutes in a suspension of 50 nm 5 g/L silica nanocolloidal suspension. μ_2 = 1.417 and S =1.602.

Figure 4-27 to Figure 4-29 show the generated Voronoï tessellations and the associated measurements of variance and entropy. All systems exhibit lower than Poisson values for the entropy and variance values suggesting that the distribution of the silica particles on the mica surface is not a random distribution but possess some form of ordering in their structure. This order may be a result of the interplay between different drying effects unique to the 50 nm particles. Our previous discussions have considered both capillary forces and dewetting effects separately due to the size of the nanoparticle being crucial to the resulting structuring mechanism. As the 50 nm particles will experience a maximum attractive capillary force with a film thickness of 25 nm, this thickness is also approaching the critical film thickness of the liquid thin film of water on a mica surface. As we expect the film to rupture within this height range it is likely that the time scale for particle structuring via capillary forces becomes limited, impeding the formation of well ordered structures and leading to some of the more amorphous clusters observed Figure 4-9. It is also possible that the subsequent dewetting may distort any preexisting structure formed by the capillary forces, which may explain why the 50 g/L samples of the 50 nm particles are amorphous in their structure, as opposed to the well ordered structuring of the 100 nm particle for this concentration.

4.9. Conclusions

The adsorption and structuring behaviour of a range of nanocolloidal particles over different colloidal concentrations and incubation periods has been studied using AFM techniques. We observed both volume fraction effects, where high colloidal concentration has resulted in reduced Debye length and subsequent increased particle adsorption at the substrate; and kinetics effects where diffusion and adsorption rates have shown adsorption amounts to be a function of both concentration and particles size.

In terms of particle structuring and formations, we observed particle size dependent behaviour. The 100 nm particles were found to form highly crystalline monolayers at high concentrations, which we have attributed to the effects of attractive capillary forces formed in the final drying stage which created the necessary interparticle forces to draw them together into close packed formations. The 10 nm particles were observed to form 2D cellular structures on samples prepared with the intermediate concentration. The patterning is very similar to that observed in the final stages of dewetting and 2D-FFT measurements suggested a spinodal-like dewetting mechanism. The 50 nm particles did not represent any distinct behaviour, in some preparation configurations we observed clustering that lacked any high levels of structure, in other configurations the particles were distributed unevenly in an isolated fashion. Voronoï tessellation analysis of AFM images provided indications of some order albeit limited. We surmise that this particle size may be subject to a mixture of the capillary and dewetting forces leading to the lack of well structured formations due to the destructive influence of the subsequent dewetting.

4.10. References

[1] M. Shimomura, T. Sawadaishi, Current Opinion in Colloid & Interface Science 6 (2001) 11-16.
[2] D. Mijatovic, J. C. T. Eijkel, A. van den Berg, Lab on a Chip 5 (2005) 492-500.
[3] J. H. Fendler, Chemistry of Materials 13 (2001) 3196-3210.
[4] J. Texter, M. Tirrell, Aiche Journal 47 (2001) 1706-1710.
[5] G. M. Whitesides, B. Grzybowski, Science 295 (2002) 2418-2421.
[6] S. C. Glotzer, M. J. Solomon, N. A. Kotov, Aiche Journal 50 (2004) 2978-2985.
[7] A. Fahmib, A. D'Aleoc, L. De Colad, F. Vogtle, Systems Self-Assembly: Multidisciplinary Snapshots (2008) 1.
[8] N. C. Seeman, A. M. Belcher, Proceedings of the National Academy of Sciences of the United States of America 99 (2002) 6451-6455.
[9] S. H. Im, Y. T. Lim, D. J. Suh, O. O. Park, Advanced Materials 14 (2002) 1367-1369.
[10] P. Hanarp, D. S. Sutherland, J. Gold, B. Kasemo, Colloids and Surfaces a-Physicochemical and Engineering Aspects 214 (2003) 23-36.
[11] P. Guyot-Sionnest, Comptes Rendus Physique 9 (2008) 777-787.
[12] M. Qhobosheane, S. Santra, P. Zhang, W. H. Tan, Analyst 126 (2001) 1274-1278.
[13] M. S. Romero-Cano, A. Martin-Rodriguez, G. Chauveteau, F. J. de las Nieves, Journal of Colloid and Interface Science 198 (1998) 266-272.
[14] N. Rana, S. T. Yau, Nanotechnology 15 (2004) 275-278.
[15] S. Maenosono, T. Okubo, Y. Yamaguchi, Journal of Nanoparticle Research 5 (2003) 5-15.
[16] N. Samid-Merzel, S. G. Lipson, D. S. Tannhauser, Physica A 257 (1998) 413-418.
[17] J. Aizenberg, P. V. Braun, P. Wiltzius, Physical Review Letters 84 (2000) 2997-3000.
[18] P. A. Kralchevsky, N. D. Denkov, Current Opinion in Colloid & Interface Science 6 (2001) 383-401.
[19] P. A. Kralchevsky, K. Nagayama, Langmuir 10 (2002) 23-36.
[20] A. S. Dimitrov, K. Nagayama, Langmuir 12 (1996) 1303-1311.
[21] N. D. Denkov, O. D. Velev, P. A. Kralchevsky, I. B. Ivanov, H. Yoshimura, K. Nagayama, Langmuir 8 (1992) 3183-3190.
[22] K. Nagayama, Colloids and Surfaces a-Physicochemical and Engineering Aspects 109 (1996) 363-374.
[23] R. K. Iler, The chemistry of silica : solubility, polymerization, colloid and surface properties, and biochemistry, Wiley, New York, 1979, p. xxiv, 866 p.
[24] S. H. Behrens, D. G. Grier, Journal of Chemical Physics 115 (2001) 6716-6721.
[25] J. N. Israelachvili, Intermolecular and surface forces / Jacob N. Israelachvili, Academic Press, New York, 1992.
[26] Z. Adamczyk, Journal of Colloid and Interface Science 229 (2000) 477-489.
[27] E. Glynos, A. Chremos, G. Petekidis, P. J. Camp, V. Koutsos, Macromolecules 40 (2007) 6947-6958.
[28] A. Chremos, E. Glynos, V. Koutsos, P. J. Camp, Soft Matter 5 (2009) 637-645.

[29] F. Madani-Grasset, N. T. Pham, E. Glynos, V. Koutsos, Materials Science and Engineering B-Advanced Functional Solid-State Materials 152 (2008) 125-131.
[30] R. Seemann, S. Herminghaus, K. Jacobs, Physical Review Letters 86 (2001) 5534-5537.
[31] C. P. Martin, M. O. Blunt, E. Pauliac-Vaujour, A. Stannard, P. Moriarty, I. Vancea, U. Thiele, Physical Review Letters 99 (2007) 116103.
[32] C. P. Martin, M. O. Blunt, P. Moriarty, Nano Letters 4 (2004) 2389-2392.
[33] E. Rabani, D. R. Reichman, P. L. Geissler, L. E. Brus, Nature 426 (2003) 271-274.
[34] L. Bergstrom, E. Bostedt, Colloids and Surfaces 49 (1990) 183-197.
[35] C. A. Johnson, A. M. Lenhoff, Journal of Colloid and Interface Science 179 (1996) 587-599.
[36] J. Goodwin, Colloids and interfaces with surfactants and polymers: an introduction, John Wiley & Sons, 2004, p. 285.
[37] W. B. Russel, D. A. Saville, W. R. Schowalter, Colloidal Dispersions, Cambridge University Press, Cambridge, UK, 1989.
[38] Z. Adamczyk, Particles at Interfaces, Interactions, Deposition, Structure, Elsevier Academic Press, 2006.
[39] M. A. Islam, Physica Scripta 70 (2004) 120-125.
[40] M. C. Gomes, A. C. Fernandes, B. S. Almeida, R. M. Almeida, Journal of Materials Science 30 (1995) 3893-3896.
[41] S. Bhattacharjee, M. Elimelech, Journal of Colloid and Interface Science 193 (1997) 273-285.
[42] A. S. Padmakar, K. Kargupta, A. Sharma, Journal of Chemical Physics 110 (1999) 1735-1744.
[43] M. Elbaum, S. G. Lipson, Physical Review Letters 72 (1994) 3562-3565.
[44] P. Moriarty, M. D. R. Taylor, M. Brust, Physical Review Letters 89 (2002) 248303.
[45] C. P. Martin, Self-organised Nanoparticle Assemblies: A Panoply of Patterns, Elsevier Science Title, 2008.
[46] A. Sharma, J. Mittal, Physical Review Letters 89 (2002) -.
[47] H. Tanaka, Journal of Physics-Condensed Matter 12 (2000) R207-R264.
[48] N. Rivier, A. Lissowski, Journal of Physics a-Mathematical and General 15 (1982) L143-L148.
[49] S. Kumar, S. K. Kurtz, J. R. Banavar, M. G. Sharma, Journal of Statistical Physics 67 (1992) 523-551.

Chapter 5: Spin Coating Silica Nanoparticles onto Mica

5.1. Abstract

We investigated the viability of spin coating techniques for self assembly of silica nanoparticles into large crystalline structures on mica. For this study we employed silica nanoparticles of diameter 150 nm and deposited them onto freshly cleaved mica using a variety of different colloidal concentrations, accelerations and rotational speeds. The samples were imaged by atomic force microscopy (AFM) in intermittent contact mode. We observed a diverse range of structuring in the colloidal particles. For changes in colloidal concentration we observed particle structuring in a *size dependent* ordering configuration, a phenomenon that was emphasised by the polydispersity of our colloidal suspension. The largest particles formed crystalline close packed structures that were surrounded by increasingly smaller particles which configured into more polycrystalline or amorphous formations. This was due to the effective capillary force being a function of liquid height, causing particles to come under the influence of attractive lateral capillary forces sequentially by size. This phenomenon became increasingly suppressed by increasing colloidal concentration. Variations in the rotational acceleration were found to affect the interparticle spacing distance. 2D-FFT radially averaged profiles of the topography images revealed increasing interparticle spacing with increasing rotational acceleration; from close packed structuring at low accelerations to increasingly spaced packing at high acceleration (>800 rpm/s). We attributed this behaviour to rapid liquid shedding from the increased acceleration of the substrate. With reduced liquid content on the surface of the substrate, the subsequent attractive capillary forces where diminished, resulting in reduced close packed ordering of the colloidal particles. Investigations into the effects of rotational speed using radial distribution functions to quantify the extent of ordering in the structuring of the nanoparticles revealed an optimum spin speed that caused the formation of large, highly crystalline structures on the sample. We attributed this to the relationship between the rotational speed and the liquid film thickness, and hence the magnitude of the capillary forces generated; with slower than optimal speeds resulted in a liquid crystal type structuring due to poor distribution of the particles on the substrate from lack of sufficient shear forces prior to lateral capillary self assembly. Higher than optimal speeds resulted in excessively

thin liquid films limiting the effectiveness of the capillary forces, and the increased shear forces eroding any structuring present, resulting in an increasingly amorphous structure.

5.2. Introduction

In previous chapters we have been exploring the behaviour of silica nanoparticles that have been adsorbed/deposited onto the surface of mica using both droplet and dip coating processes. With larger particles (≈100 nm) we found that under certain conditions highly ordered, close packed formations of a monolayer structure could be produced. The fabrication of structures that possess long range periodicity is of great interest to fields of science and technology in both research and industry. A variety of methods such as gravity sedimentation [1], electrostatic repulsion [2, 3], template assisted assembly [4] and capillary force induced convective self assembly [5-9] have been developed to create colloidal crystals with millimetre or larger domains. Although these processes are suitable to laboratory scale production, they are less useful to industrial process due to the time scales and tedious fabrication processes involved. Several recent studies have demonstrated the spin coating process provides a simple and efficient method for dispersion of small particles onto a substrate [10-14].

The spin coating process for a colloidal suspension occurs in four distinct stages of development, the first two happening in quick succession while the latter two steps proceeding over a much longer time frame. In the first stage, a colloidal fluid is deposited as a droplet onto the substrate. The second stage is the acceleration of the substrate up to the programmed rotational speed, causing the droplet to spread out to form a film that rotates at approximately the same rate as the substrate. Shear induced ordering can occur. It is assumed that, when a given shear stress is applied, a sort of order-disorder equilibrium is established, in which the forward (Brownian motion) and backward (shear-induced ordering) processes balance. Shear has a dual influence on the order in colloidal suspensions. At high shear rates, it can disorder, or melt, a colloidal crystal, but at low shear rates or at low-amplitude oscillatory shear, it can induce order. Shear changes the growth kinetics, i.e., the induction time, density of nuclei, and crystal growth rate. In the third stage when the target speed has been reached, the now spread out film begins to thin globally. This thinning is controlled primarily by centrifugal and viscous shear forces. Finally in the fourth

stage the film becomes sufficiently thin so that evaporation now dominates the behaviour of the film thickness. The transition from the third to fourth stage is dependent on the volatility and other material properties of the suspension liquid. In the case of colloidal suspensions, when the film thickness approaches that of the particle diameter, capillary forces play a dominant role in the particle structuring.

Jiang *et al.* [13, 15, 16] have developed a procedure to prepare thin colloidal silica-polymer composite films based on a spin coating procedure where a colloidal suspension is first dispersed over a silicon wafer and then spin coated in order to induce shear in the thin film of suspension, causing structured ordering of the particles into 3D structures. This is subsequently photopolymerised to provide mechanical stability. Mihi *et al.* [10] experimented with variations of the suspension liquid composition in order to fine tune the volatility during spin coating and induce multilayer ordering of submicrometer silica and functionalised polystyrene colloids. Moon *et al.* [11] explored the effect of shear forces on the crystallinity of 230 nm polymer colloids on silicon wafers. They found that the level for crystallinity could be linked to the rotational speed of the spin coater, leading to the fine tuning of well ordered structures.

In this chapter we explore the application of spin coating techniques of silica colloidal nanoparticles on mica for the formation of well ordered monolayer structures that would have potential industrial and scientific applications in the areas of photonics [12], biosensors [13], the semiconductor industry [14, 15] and quantum dot technology [16]. We used freshly cleaved mica squares onto which we deposited fumed silica particles of 150 nm in diameter suspended in water using spin coating techniques. We chose to vary the colloidal suspension concentration, the rotational acceleration and the rotational speed in order to investigate how these parameters affect the structuring of the colloidal nanoparticles. AFM techniques were used to investigate the fine structure of the resultant samples. We found that at low colloidal concentrations, the configuration of the particles structured in a *size dependent* ordering, a phenomenon that was emphasised by the polydispersity of our samples. At high concentrations (>25 g/L) this phenomenon was found to be suppressed by

the surface particle density and increasingly amorphous structuring occurred. Rotational acceleration was found to affect the interparticle spacing. Using 2D-FFT radially averaged profiles, we found that the interparticle spacing increased, from close packed structuring at low accelerations to increasingly spaced packing at high acceleration (>800 rpm/s). This behaviour was attributed to accelerated liquid shedding, which diminished the effectiveness of the attractive capillary forces and reduced close packed ordering of the colloidal particles. Finally for the rotational speed results we used radial distribution functions to quantify the extent of ordering in the structuring of the nanoparticles. We found the rotational speed to govern the "crystallinity" of the samples, with the appearance of an optimum rotational speed to maximise long range crystal packing of the colloidal particles for our experimental setup. This behaviour was attributed to both the effects of shear stress erosion on the structure and the relationship between the rotational speed and the liquid film thickness, and hence the magnitude of the capillary forces generated.

5.3. Materials

Colloidal samples used in this study were aqueous dispersions of amorphous, non porous fumed silica colloidal particles purchased from Bangs Laboratories, Inc (Fishers, IN, USA). The colloidal nanoparticle diameter was quoted by the manufacturer as 150 nm with a maximum coefficient of variation (CV) of 15%, giving a possible diameter range of 127.5 nm to 172.5 nm. Particles were supplied nonfunctionalised and suspended in deionised water from the manufacturer. 11 mm square mica sheets and metal mounting discs supplied by Fisher (Leicestershire, United Kingdom) were used for preparing sample substrates. All water used in the experiments was ultrapure water with a resistivity of 18.2 MΩ-cm at 25^{o}C. When submersed in water, the surfaces of both the silica nanoparticles and freshly cleaved mica have a negative charge. For the silica this is due to the dissociation of silanol groups in the presence of water, and for the mica a net negative charge is generated by the uneven charge distribution of potassium ions on the cleaved surfaces [17]. The colloidal samples were supplied in 10 ml vials of 50 g/L concentration (volume fraction $\phi = 2.27\times10^{-2}$) from the manufacturer; where needed, these were further diluted by using ultrapure water to create dispersions of 25g/L ($\phi = 1.14\times10^{-4}$), 20 g/L ($\phi = 9.08\times10^{-3}$), 15 g/L ($\phi = 6.81\times10^{-3}$), 10 g/L ($\phi = 4.54\times10^{-3}$) and 5 g/L ($\phi = 2.27\times10^{-3}$). The particle ζ-potential was evaluated using a Malvern Zetasizer (Worcestershire, United Kingdom) and measured to be -47.3mV. For storage purposes the colloidal suspensions were kept in a refrigerator at 4^{o}C to inhibit any microbial growth.

5.4. Sample Preparation

All samples were prepared using a Spin150 spin coater (SPS-Europe, Putten, The Netherlands), with variations of the colloidal concentration, rotational acceleration and speed. The mica squares were secured onto metal mounting disks using an adhesive tab and attached to the spin coater chuck via a vacuum seal. The

mica was cleaved by using tape to remove the top sheet. This procedure was carried out inside a fume cupboard to minimise airborne pollutants from contaminating the surface [18]. Before application of the colloidal suspension, vials were agitated for 30 seconds to ensure an even distribution of the colloidal density throughout the suspension.

Three droplets (approximately 0.16 ml) of the colloidal suspension were deposited onto the freshly cleaved mica via a clean glass pipette. The droplet was observed to wet the entire mica substrate and pinned to the edges of the square. The spin coater hood was closed to avoid heterogeneous particles from contaminating the sample. The droplet was left on the surface of the mica for approximately 30 seconds before initiation of the spin coating program. At low rotational speeds (<800 rpm) the colloidal suspension was observed to build up at the edge of the mica squares, in particular the corners. The magnitude of the build-up was dependent on the acceleration. All samples were spun at 8000 rpm for 6 minutes at the end of their program run to eliminate this excess suspension and dry the samples. Upon completion of the spin coating program samples were removed from the spin coater and placed in a Petri dish inside a desiccator until imaged, to reduce adsorption of water from the atmosphere, due to the highly hydrophilic nature of both silica and mica.

Each set of experimental runs had its own specific spin coating program:

- Program A: The first set of experiments had at a rotational speed of 8000 rpm with a 50 rpm/s acceleration for 520 seconds, resulting in a spin up time of 160 seconds, with 8000 rpm maintained for 360 seconds.

- Program B: The second set of experiments had a rotational speed of 4000 rpm with different rotational accelerations (200 to 1000 rpm/s in 200 rpm/s steps) for 120 seconds followed by 8000 rpm for 360 seconds.

- Program C: The third set of experiments had different rotational speeds (200 rpm to 1000 rpm with 200 rpm steps then 2000 rpm to 8000 rpm with 2000 rpm steps) with a 1000 rpm/s acceleration for 120 seconds followed by 8000 rpm for 360 seconds.

5.5. Measurements

Imaging was done using atomic force microscopy on a Veeco Multimode – Nanoscope IIIa AFM (Santa Barbara, CA, USA) under soft tapping mode™ regime (the cantilever tip makes intermediate contact with the surface). Silicon nitride cantilevers from Windsor Scientific Ltd (Berkshire, United Kingdom) at a resonance frequency of approximately 320 MHz, and a spring constant of 42 N/m were used. The nominal tip radius was quoted by the manufacturer as <8 nm. The cantilevers were operated at approximately 5% lower than their resonance frequency and the resonating tip was lowered close enough to the surface to cause the tip to make intermittent contact with the surface. Raster scans of areas of interest were performed at various sizes. All scans were performed in air at room temperature. The tip of the silicon nitride cantilevers usually acquires a negative charge due to moisture in the atmosphere forming acidic silanol groups on the tip surface; this inhibits contamination of the tip end with the charged colloidal particles [28, 29]. For post processing of the AFM images, the Scanning Probe Image Processor (SPIP) from Image Meteorology (Hørsholm, Denmark) was used. Except where stated all images were post-processed by simple flattening alone.

The samples prepared have shown homogenous structures and the images presented are representative of the concentration and conditions of sample preparation for every occasion unless otherwise stated.

5.6. Results and Discussion

5.6.1. Variation of Colloidal concentration

For the variation in colloidal concentration we started with the lowest concentration of 5 g/L. Figure 5-1 shows the topography image of the spin coated sample displaying individual islands of colloidal formations with well ordered and close packed arrangements seen throughout all structures. We note that for a number of clusters, the particles have arranged in a size dependent manner, with larger particles situated at the centre surrounded by smaller particles. Other clusters have a less size correlated structure with various particle sizes throughout the cluster.

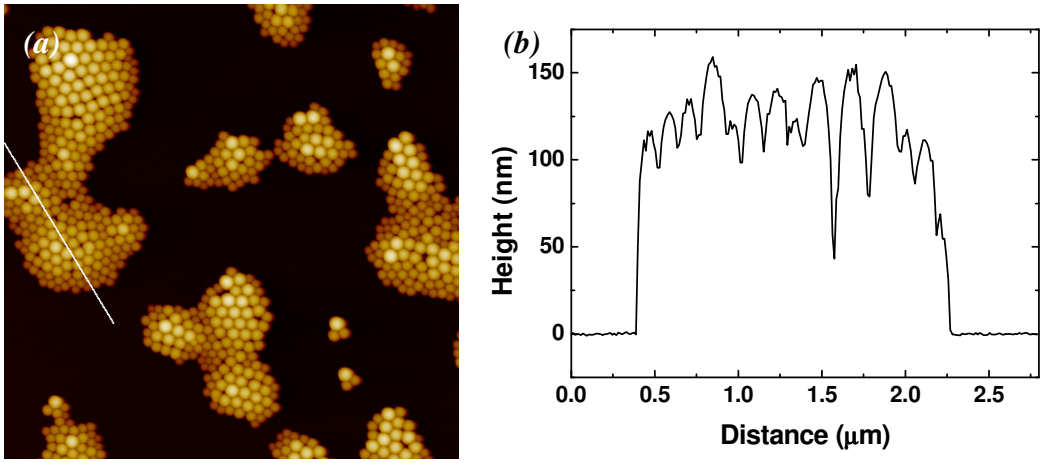

Figure 5-1. (a) 6 × 6 μm^2 topography scan of a colloidal sample prepared using the 5 g/L colloidal suspension and spin coating program A with (b) height profile corresponding to the white line.

Height profiling of the clusters shows a variation in particle height between approximately 120 nm to 160 nm, which are within reasonable agreement with the expected spread of particle diameters.

In Figure 5-2 we have increased the colloidal concentration to 10 g/L and observe that the particles have begun to structure in bigger islands of well defined order, with the larger particles surrounded by increasingly smaller particles in a polydisperse

configuration. While we would associate close packing of colloidal particles with a hexagonal formation, the polydisperse nature of the particles has generated a variety of different packing formations.

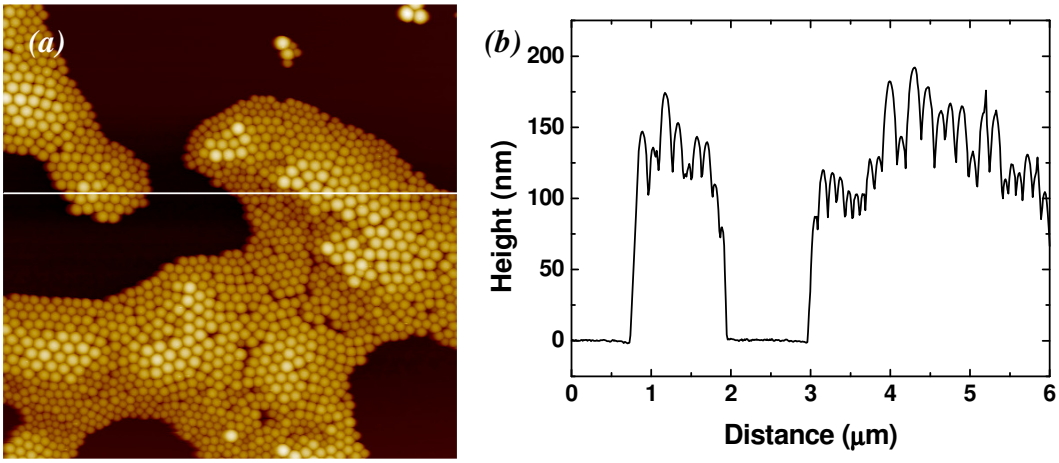

Figure 5-2. (a) 6 × 6 μm^2 topography scan of a colloidal sample prepared using the 10 g/L colloidal suspension and spin coating program A with (b) height profile corresponding to the white line.

With an increase in the colloidal concentration to 15 g/L we start to observe large monolayer structures of the colloidal particles, as seen in Figure 5-3. In particular we see in Figure 5-3b that the larger particles engulfed in the monolayer films exhibit high levels of ordering, with the surrounding smaller particle more prone to polycrystalline and amorphous structuring.

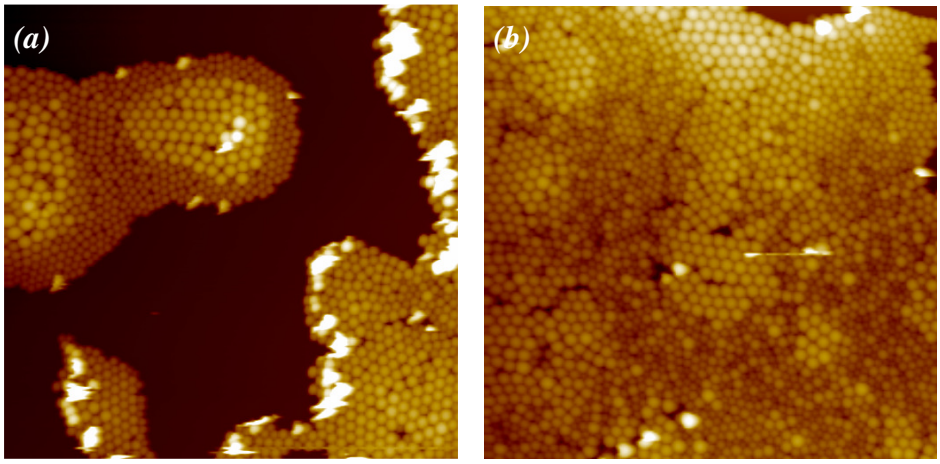

Figure 5-3. (a) & (b) 6 × 6 μm^2 topography scan of a colloidal sample prepared using the 15 g/L colloidal suspension and spin coating program A; (b) shows some of the finer structure of the film of polydisperse colloidal particles.

In Figure 5-4 at a colloidal concentration of 20 g/L we see that the size dependent ordering of the colloidal particles is still in effect, with larger well ordered particles surrounded by smaller particles with varying degrees of close packed structuring.

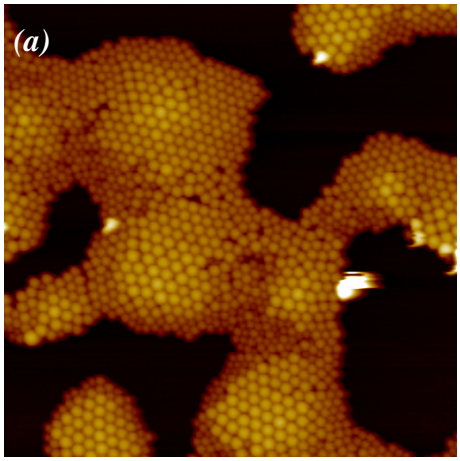

Figure 5-4. (a) 6 × 6 μm^2 topography scan of a colloidal sample prepared using the 20 g/L colloidal suspension and spin coating program A.

At a colloidal concentration of 25 g/L we begin to see the formation of a continuous film across the surface of the substrate, with only minor gaps appearing in the film, as seen in Figure 5-5. A height profile confirms that the colloidal film is monolayer,

and that protruding particles are in fact still within the upper region of the colloidal diameter CV. A 2D-FFT of the film structure reveals that the particles are configured in an amorphous configuration. While they lack the well ordered structure of the lower concentrations, the 25 g/L colloidal concentration samples still exhibit a characteristic spacing of 140 nm, which is approximately the median particle diameter.

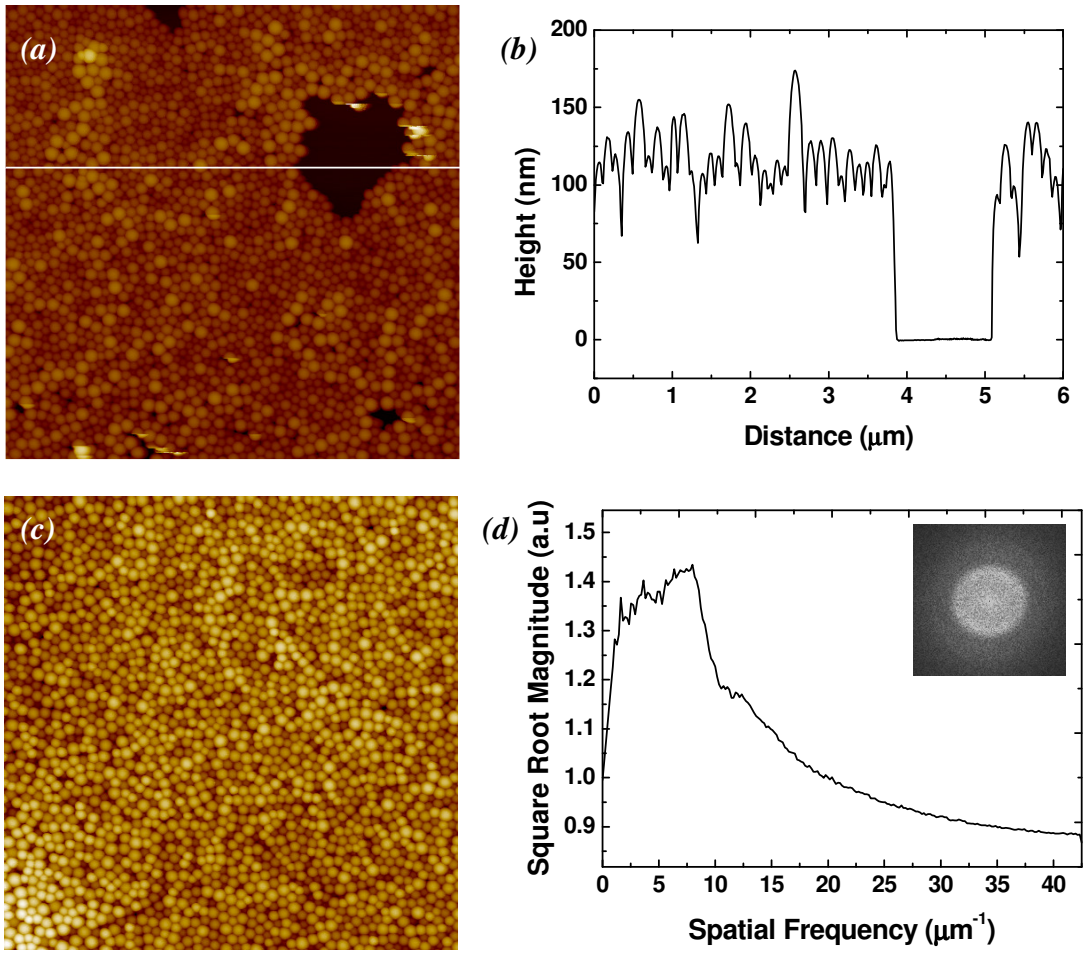

Figure 5-5. (a) 6 × 6 μm^2 topography scan of a colloidal sample prepared using the 25 g/L colloidal suspension and spin coating program A with (b) height profile corresponding to the white line showing monolayer structure. (a) 6 × 6 μm^2 topography scan of a continuous film with (d) corresponding radially averaged 2D-FFT.

Finally at a particle concentration of 50 g/L the film structuring has become noticeably less ordered, as seen in Figure 5-6. A 2D-FFT confirms that the characteristic length has increased to 170 nm which suggests a non close packed

ordering. The topography image clearly shows the existence of small spaces between particles that was not present in previous samples.

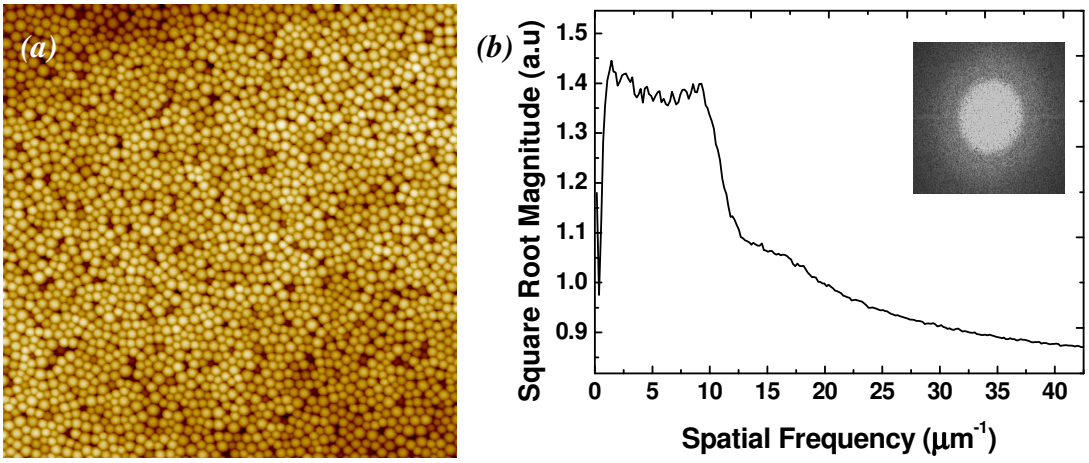

Figure 5-6. (a) 6 × 6 μm^2 topography scan of a colloidal sample prepared using the 50 g/L colloidal suspension and spin coating program A with (b) corresponding radially averaged 2D-FFT.

From these results we find that at low concentrations the particles assembled onto the substrate into isolated clusters and grew in size with increasing concentration until forming monolayer films. We observed in the majority of the lower colloidal concentration samples the formation of particle configurations that have larger particles in highly ordered structures surrounded by smaller particles that exhibit a mixture of polycrystalline and amorphous structuring. This formation has been observed in other systems where polydisperse or binary suspensions of colloidal particles have been allowed to self assemble into monolayer films. Such structuring is often are referred to as "Apollonian" or size-dependent packing [19, 20]. We attribute this behaviour to the polydispersity of our own colloidal suspension and the effects of capillary forces during the fourth stage of the spin coating process where the liquid film is sufficiently thin to induce lateral capillary forces between neighbouring particles. From capillary theory [21] it is clear that the lateral capillary force occurs due to the partial immersion of neighbouring particles forming a meniscus that induces an attractive force. As such the largest particles will be the first to experience such an attractive force. The film thickness at this point will be

larger than the diameter of smaller particles, so their mobility will allow for reconfiguration of the particles in the thin film; with larger particles being drawn together, forcing the smaller particles to the extremities. As the liquid film thins, it creates an ordering mechanism which effectively sorts the particles by size. We see this phenomenon most clearly with the lower concentration samples where the reduced particle density allows for a higher freedom of particle movement on the substrate due to the increased volume of liquid between particles. Thus particles are able to rearrange more easily facilitating more size dependent ordering. If we compare Figure 5-3b with Figure 5-5a we see that at a concentration of 15 g/L the largest particles have formed patches of highly ordered structures, while at a concentration of 25 g/L the largest particles are less ordered, exhibiting only smaller clusters of close packing. The 25 g/L and 50 g/L samples show a distinct lack of size dependent ordered crystals; indeed the 50 g/L did not display any observable order in its film structuring. This behaviour may be due to the adsorption density reaching a jamming limit on the surface of the mica substrate. Above this jamming limit the colloidal particles restricted in their lateral mobility, being able to approach neighbouring particles under the influence of lateral capillary forces, but unable to reorganise their ordering.

5.6.2. Variation of Rotational Acceleration

For investigations into the effects of increasing rotational acceleration we have used the 50 g/L colloidal suspension in order to ensure that total coverage of the mica substrate is achieved.

Figure 5-7 shows the film structure for an acceleration of 200 rpm/s. The topography image shows patches of highly ordered particles interspersed with dense amorphous structuring of the surrounding particles. A 2D-FFT of the topography shows a distinct ring indicating a characteristic spacing between particles of approximately 130 nm.

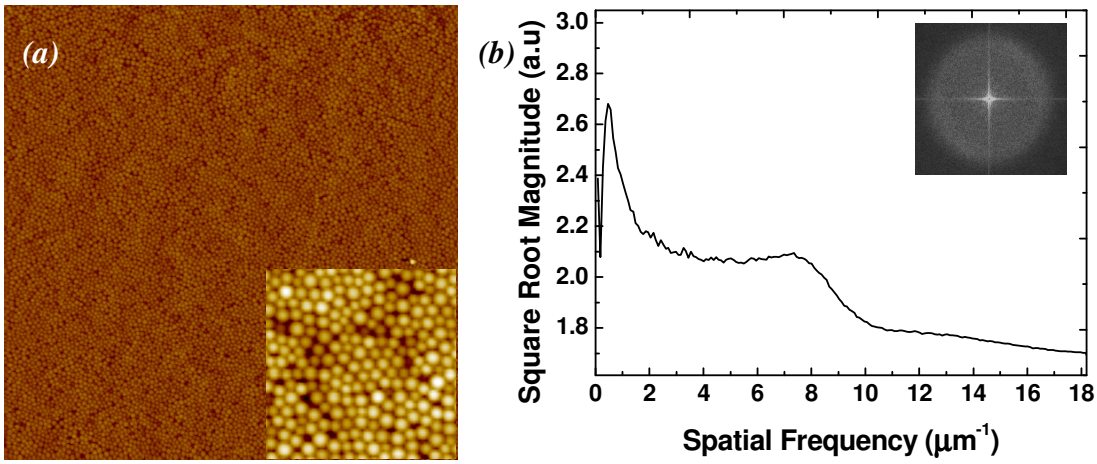

Figure 5-7. (a) 14 × 14 µm^2 topography scan of a colloidal sample prepared using the 50 g/L colloidal suspension with spin coating program B with an acceleration of 200 rpm/s with zoom insert. (b) Corresponding radially averaged 2D-FFT of (a).

Figure 5-8 shows the film structure for an acceleration of 400 rpm/s. We note that the topography image shows similar patches of highly ordered particles although not as prevalent as that of the 200 rpm/s sample. The 2D-FFT reveals the existence of a characteristic spacing between the particles, but we note that the characteristic spacing is increased slightly to 138 nm.

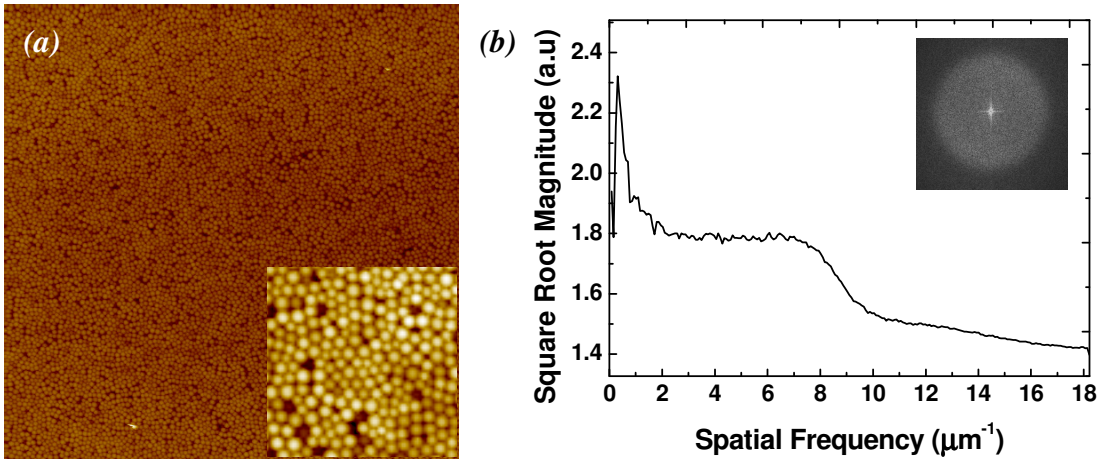

Figure 5-8. (a) 14 × 14 µm^2 topography scan of a colloidal sample prepared using the 50 g/L colloidal suspension with spin coating program B with an acceleration of 400 rpm/s with zoom insert. (b) Corresponding radially averaged 2D-FFT of (a).

Figure 5-9 shows a similar tread in behaviour with a reduction in the appearance of crystalline areas of the topography with increasing acceleration. At 600 rpm/s we see a continued expansion of the characteristic spacing observed on the 2D-FFT to 140 nm.

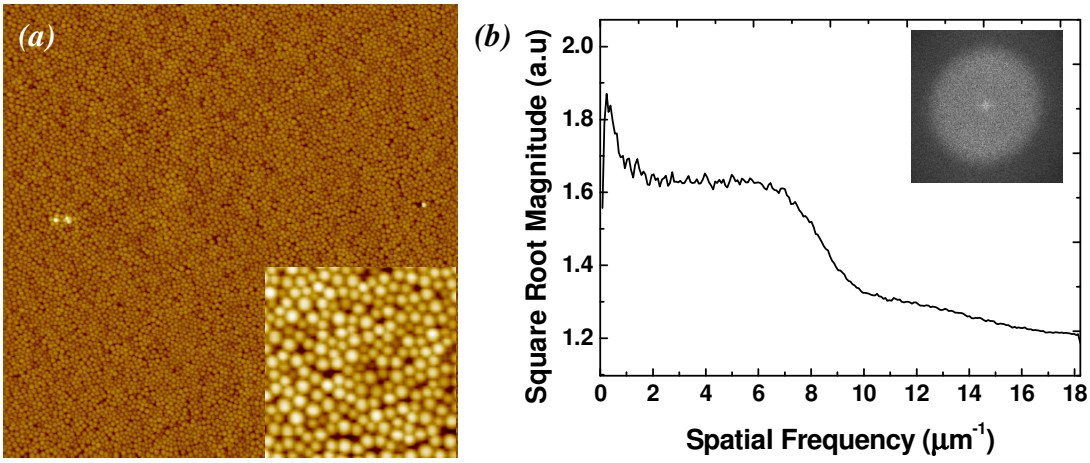

Figure 5-9. (a) 14 × 14 µm^2 topography scan of a colloidal sample prepared using the 50 g/L colloidal suspension with spin coating program B with an acceleration of 600 rpm/s with zoom insert. (b) Corresponding radially averaged 2D-FFT of (a).

Figure 5-10, representing a rotational acceleration of 800 rpm/s, shows the first large scale evidence of large gaps appearing between particles in the film, approximately

60-80 nm in size. Previous to this the observed film structure showed a predominantly continuous formation. These gaps are observed to become more widespread at a rotational acceleration of 1000 rpm/s, shown in Figure 5-11. The corresponding 2D-FFT images confirm that the characteristic spacing of the particles has increased measurably at these accelerations.

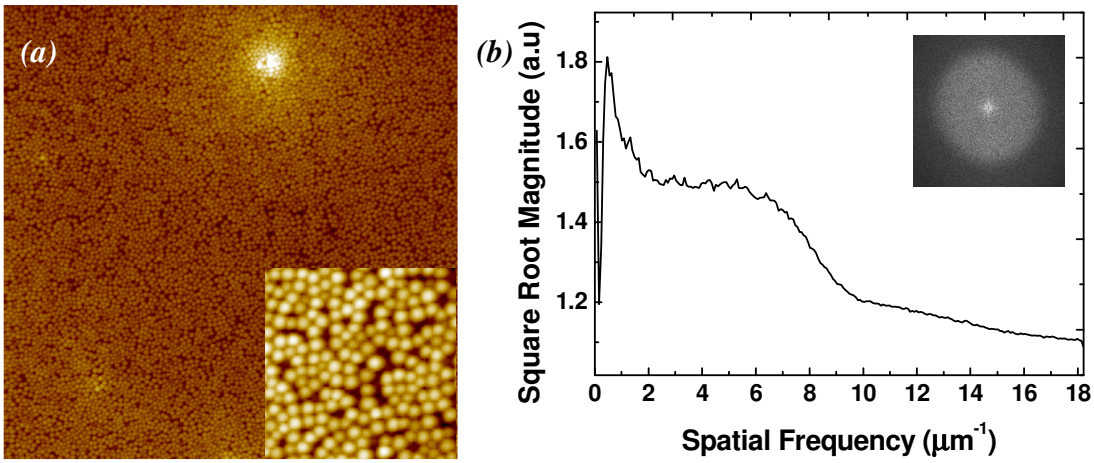

Figure 5-10. (a) 14 × 14 µm^2 topography scan of a colloidal sample prepared using the 50 g/L colloidal suspension with spin coating program B with an acceleration of 800 rpm/s with zoom insert. (b) Corresponding radially averaged 2D-FFT of (a).

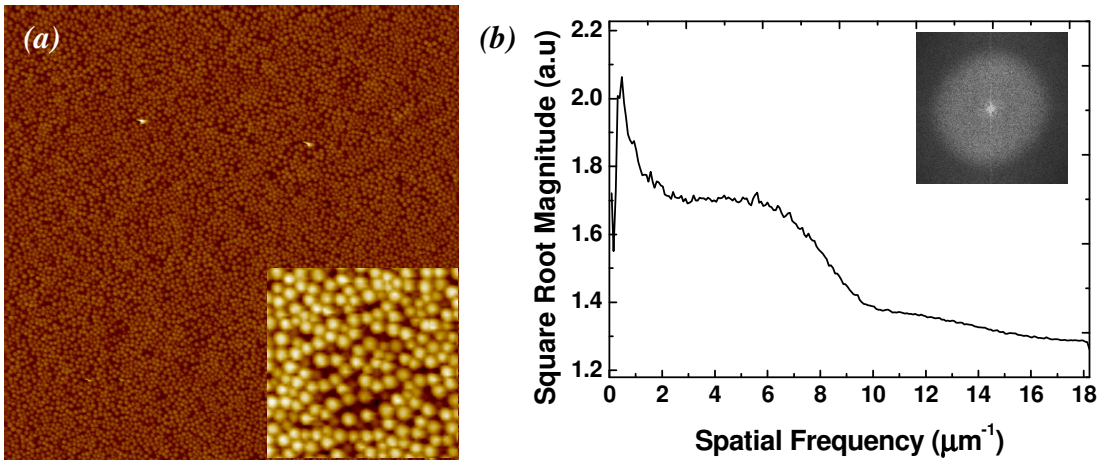

Figure 5-11. (a) 14 × 14 µm^2 topography scan of a colloidal sample prepared using the 50 g/L colloidal suspension with spin coating program B with an acceleration of 1000 rpm/s with zoom insert. (b) Corresponding radially averaged 2D-FFT of (a).

Table 5-1 gives an overview of the calculated characteristic particle spacing as a function of rotational acceleration and Figure 5-12 shows that there is a distinct change in the characteristic spacing of the particles between 600 rpm/s and 800 rpm/s suggesting a change in the system behaviour.

Table 5-1. Comparison of rotational acceleration and the characteristic spacing of the silica nanoparticles calculated from the radially averaged 2D-FFT measurements.

Rotational Acceleration (rpm/s)	Characteristic Spacing (nm)
200	133
400	138
600	140
800	168
1000	172

Error! Objects cannot be created from editing field codes.

Figure 5-12. Graph of Table 5-1 showing a distinct change in the relationship between the rotational acceleration and the characteristic particle spacing length.

With variation in the rotational acceleration of the substrate during the spin coating program we found that the average particle distance calculated using a radially averaged 2D-FFT measurements was observed to increase with increasing acceleration. Figure 5-12 shows a plot of the characteristic particle spacing against rotational acceleration. We consider that with increasing acceleration, the time to reach the target speed is reduced (step 2 of the generalised spin coating process), which corresponds to increased rate of change of shear force, which is responsible for the spreading of the colloidal suspension. In Figure 5-13 we present an illustration outlining the affect of acceleration of the thinning of the colloidal suspension and the subsequent capillary self assembly. At high rotational accelerations the bulk of colloidal suspension on the sample substrate is expelled relatively early in the spin coating program, leaving a relatively thin layer of

colloidal suspension behind. This thinner film results in reduced particle mobility so an even distribution of the particles across the surface via shear forces is not achieved. The subsequent lateral capillary force will be less effective in close packing the particles, due to the dependence of the capillary force magnitude on the interparticle separation [5]. This explains why gaps are observed in the higher acceleration samples, as these are generated by uneven spacing of particle leading to uneven lateral capillary forces between neighbouring particles. Conversely at lower accelerations the liquid surface tension at the edge of the sample has not been overcome by the centrifugal force at an early stage, allowing for the existence of a thicker liquid film in which the particles can form a monolayer structure via shear forces, thus facilitating capillary forces during the drying stage, leading to highly ordered structuring of the colloidal particles.

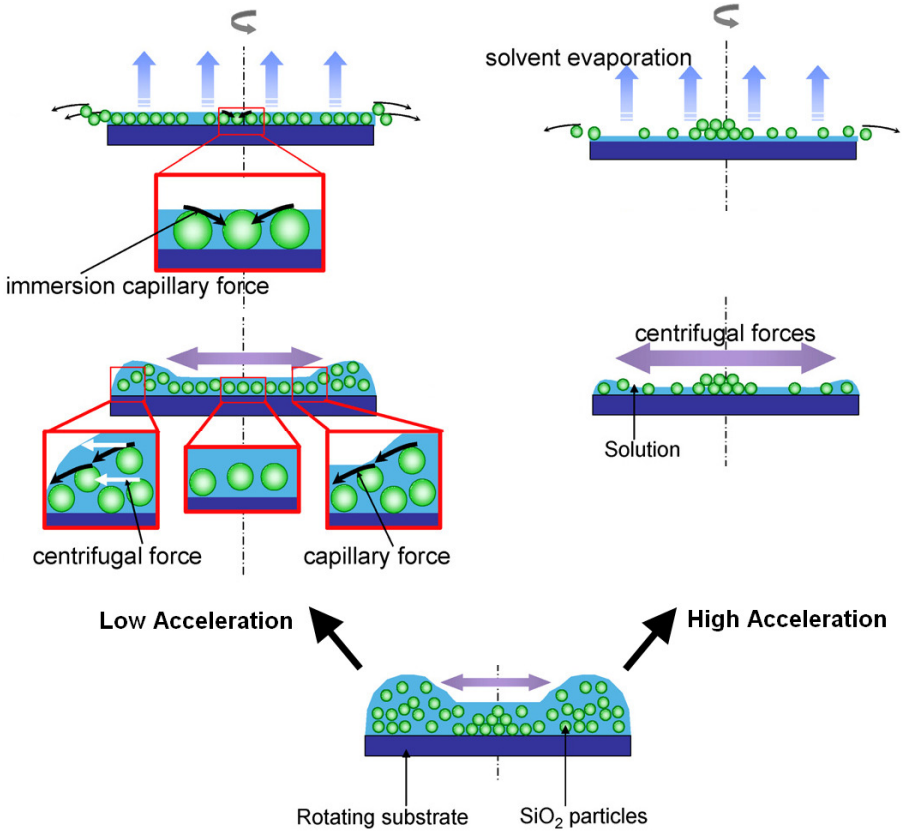

Figure 5-13. Illustration of possible phenomena occurred during spin coating of silica nanoparticles at different accelerations. Adapted from [22].

We also found that there was a noticeable increase in the characteristic spacing at 600 rpm/s suggesting a change in behaviour in the distribution of the particles on the surface. Rehg *et al.* [23] have noted that at sufficiently high accelerations the coated film may reaches its final thickness while the substrate is still accelerating while at low acceleration rates the effect of different acceleration protocols is negligible, since the time required for radial outflow to cease exceeds the time required for the substrate to reach its final angular velocity. It may be the case therefore that with accelerations greater than 600 rpm/s we enter a regime where the colloidal suspension film has reached its maximum thickness before maximum rotational speed has been achieved. This could result in poor dispersal of the colloidal particles at the substrate interface (due to the low rotational speed) resulting in compromised lateral capillary forces and thus less densely packed structures.

5.6.3. Variation of Rotational Speed

For investigations into the effects of increasing rotational speed we have also used the 50 g/L colloidal suspension in order to ensure that total coverage of the mica substrate is achieved.

In Figure 5-14 we see that for a rotational speed of 200 rpm the silica nanoparticles have formed into a monolayer which exhibits close packing of the colloidal particles, as seen in the zoomed section. The monolayer film did exhibit some exposed patches of substrate but the majority of the sample was homogeneous.

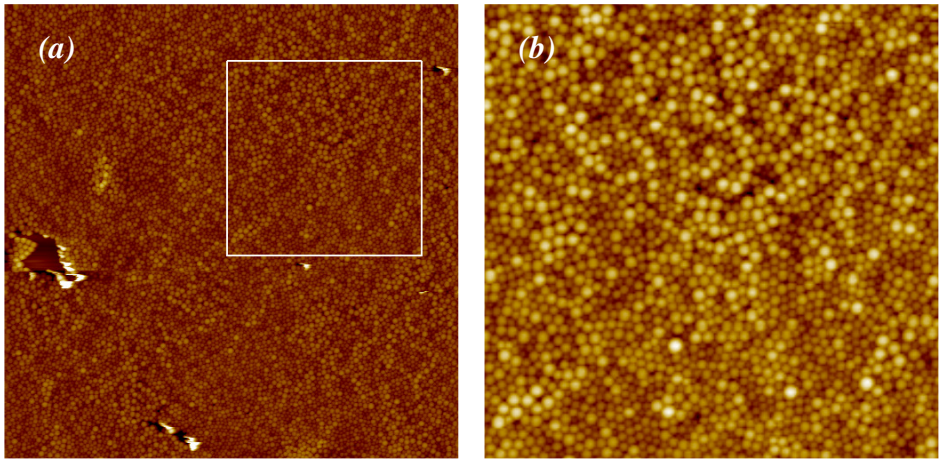

Figure 5-14. (a) 14 × 14 μm^2 topography scan of a colloidal sample prepared using the 50 g/L colloidal suspension with spin coating program C at a rotational speed of 200 rpm. (b) Corresponding image of zoomed section marked in (a) showing structured formation of particles.

For a rotational speed of 400 rpm we see in Figure 5-15 that the colloidal nanoparticles have become increasingly ordered in their configuration, with the zoomed section showing a high degree of polycrystalline structuring of the nanoparticles and a reduction in the appearance of gaps between neighbouring particles.

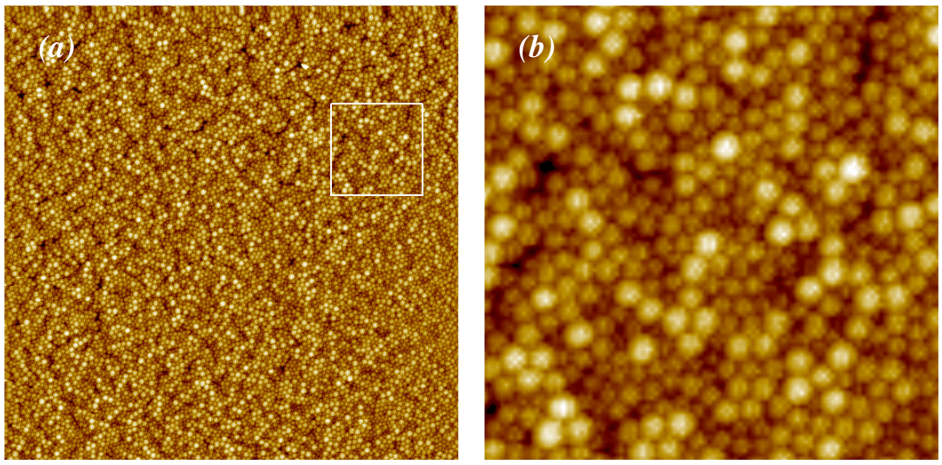

Figure 5-15. (a) 14 × 14 µm^2 topography scan of a colloidal sample prepared using the 50 g/L colloidal suspension with spin coating program C at a rotational speed of 400 rpm. (b) Corresponding image of zoomed section marked in (a) showing structured formation of particles.

With an increase of the rotational speed to 600 rpm we observe large scale crystallisation of the silica nanoparticles across the surface of the substrate (Figure 5-16a). We have chosen this particular image as it has some small voids in the film that allow us to take height profiles of the film. It should be noted that this is not representative of the majority of the sample area. The highly ordered structures are of a monolayer thickness as indicated by the height profile in Figure 5-16b. A smaller topography scan (Figure 5-16c) illustrates the hexagonal close packed nature of the film. We observed a multitude of grain boundaries across the surface of the substrate with various crystal orientations. 2D-FFT measurements of the topography show a distinctive six point FFT corresponding to the hexagonal packing of the colloidal particles and a crystal lattice constant of 130 nm.

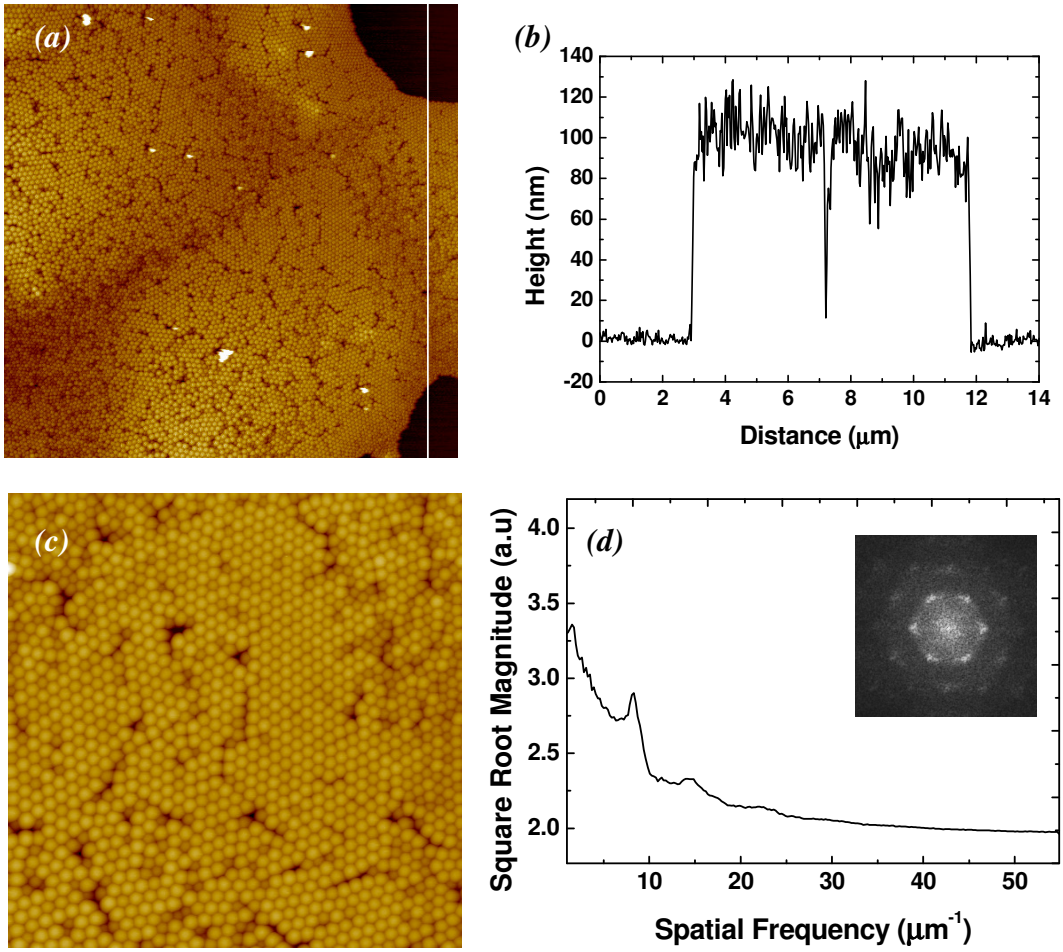

Figure 5-16. (a) (a) 14 × 14 μm^2 topography scan of a colloidal sample prepared using the 50 g/L colloidal suspension with spin coating program C at a rotational speed of 600 rpm. (b) Height profile of the structured film corresponding to the white line in (a). (c) Zoom showing the hexagonal close packed structuring of the silica nanoparticles with (d) a 2D-FFT with clear peak of the crystal lattice constant.

Figure 5-17 gives an overview of the topography images for rotational speeds from 800 rpm to 8000 rpm. We note that the previous large scale crystalline structuring of the silica nanocolloids has given way to a colloidal film of reduced order. The 800 rpm sample (Figure 5-17a) shows numerous small patches of polycrystalline and amorphous formations similar to that found in the 400 rpm sample. Similar structuring is found in the 1000 rpm samples but at 2000 rpm (Figure 5-17c) the occurrences of well ordered regions of particles have been severely diminished. By 6000 rpm (Figure 5-17e) we observe the appearance of gaps between neighbouring particles that becomes exacerbated with increasing rotational speed, as seen in the

8000 rpm sample (Figure 5-17f), along with a total loss of ordered structuring amongst the nanoparticles.

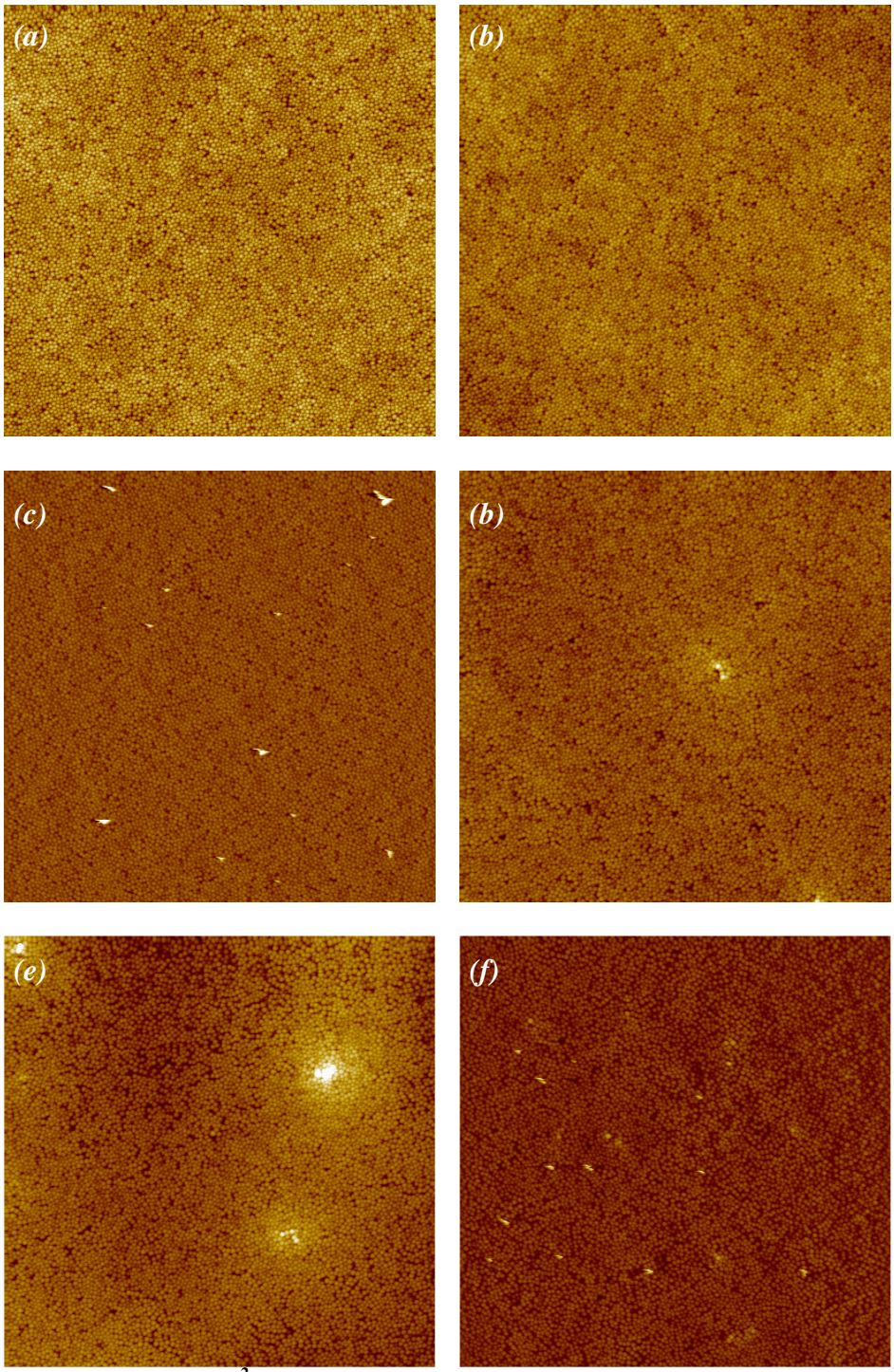

Figure 5-17. (a) 14 × 14 μm^2 topography scan of a colloidal sample prepared using the 50 g/L colloidal suspension with spin coating program C at a rotational speed of (a) 800 rpm, (b) 1000 rpm, (c) 2000 rpm, (d) 4000 rpm, (e) 6000 rpm and (f) 8000 rpm.

We found that the level of order in the structuring of the particles varied with rotational speed. We used radial distribution function analysis to quantitatively examine this level of order or "crystallinity" and the packing density [24]. A radial distribution function represents the probability of finding two particles separated by a distance *r*. It is generated by considering each particle, measuring the distance to every other particle and then counting the number of particles a distance *r* to $r + \delta r$ from that particle, with the denominator representing the area of the shell. This process is repeated for all particles until an average value is determined which is then normalised by dividing by the average particle number density $\langle \rho \rangle$ shown in 5-1. The resultant data is normalised again by setting the asymptotic value to equal one.

$$g(r) = \frac{1}{\langle \rho \rangle} \frac{dn(r, r+\delta r)}{da(r, r+\delta r)} \qquad \textbf{5-1}$$

Radial distribution analysis of several topography images revealed a selection of different particle behaviours for the rotational speeds used. Figure 5-18 shows the radial distribution analysis results for the 200 rpm, 600 rpm, 1000 rpm and 8000 rpm samples. We note that the 600 rpm has several distinct peaks indicating the presence of the highly crystalline structure, with reoccurring nearest neighbour distances. Both the 200 rpm and the 1000 rpm samples show a much lower first peak followed by a second and third peak before the correlation approaches one. This is indicative of a liquid like structure where ordering is much more localised [24]. Finally we see that the 8000 rpm graph has an even lower first peak but more interestingly its correlation is less than one suggesting a gaseous crystal structure lacking any real structuring.

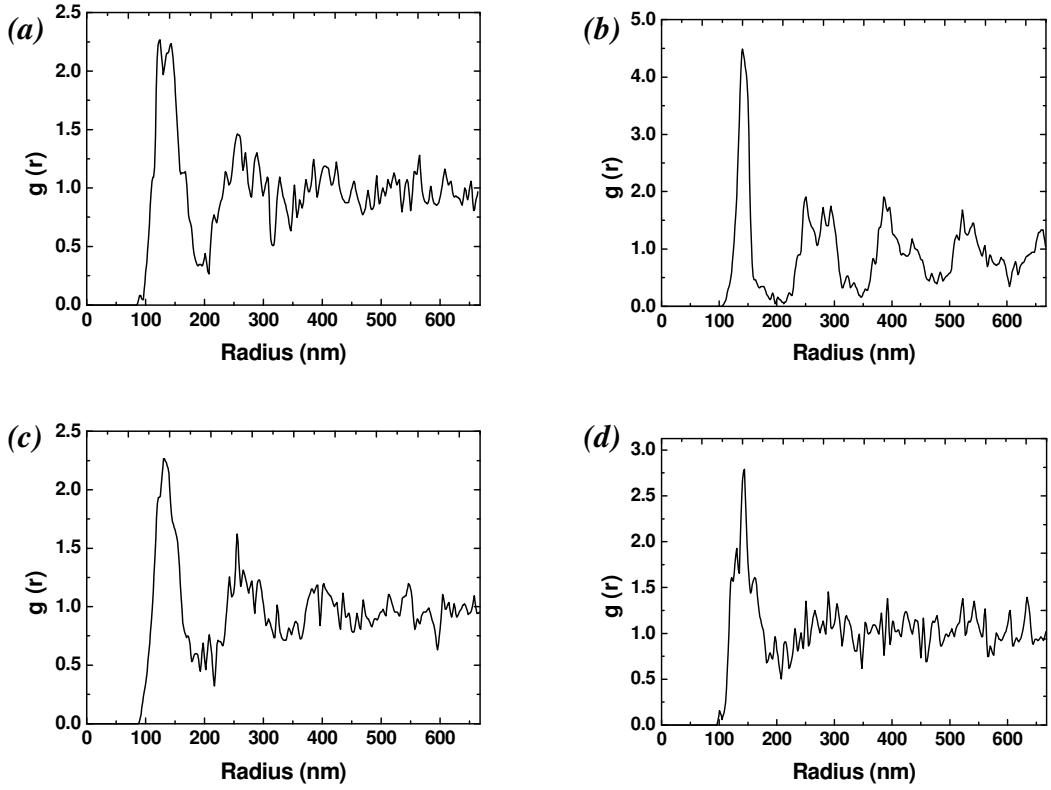

Figure 5-18. Radial distribution functions of the topography scans of samples prepared using spin coating program C with rotational speeds of (a) 200 rpm, (b) 600 rpm, (c) 1000 rpm and (d) 8000 rpm.

This suggests that the structuring of the particles goes through a transition of moderate order at low rotational speed to high order at a rotational speed of 600 rpm, and subsequently the order again diminishes with increasing rotational speed.

The spin coating modelling work of Emslie *et al.* [25] and Meyerhofer [26] provides relationships between the rotational speed and film thickness when the liquid film is in a stable condition where centrifugal and viscous forces are just in balance. In particular Meyerhofer has shown that the relationship between the final liquid film thickness h_f can be estimated by equation 5-2:

$$h_f = c_0 \left(\frac{e}{2(1-c_0)K} \right)^{\frac{1}{3}} \qquad \textbf{5-2}$$

Where c_0 is the solids concentration in the solution, e is the evaporation rate and K is a constant defined as $K=\rho\omega^2/3\eta$ where ρ is the fluid density, ω is the rotational speed and η is the fluid viscosity. The evaporation rate should be constant over the entire substrate and depend on rotation rate according to $e = C\sqrt{\omega}$ where the proportionality constant, C, must be determined for the specific experimental conditions. From this we can clearly see the dependence of h_f on ω. This film thickness will also dictates the magnitude of the lateral capillary force, due to the dependence of the force on the meniscus height, as discussed in previous chapters. In our system we find that there is an optimum rotational speed for a given system to produce highly structured configurations. We conclude that at low rotational speeds where the film has a more amorphous structuring, the lower shear forces have lead to dense distribution of the particles across the surface of the substrate. As the film will be much thicker than the particle diameter, extended periods of evaporation must occur before the establishment of lateral capillary forces. Subsequently the capillary self assembly occurs relatively late in the spin coating program, leading to more amorphous structuring of the particles. At 600 rpm, an equilibrium has been reached were the rotational speed has induced both sufficient shear forces to spread the particles in a monolayer distribution and form a liquid film thin enough to establish sufficiently strong lateral capillary forces so that close packed formations are created during the program time frame. At rotational speeds > 600 rpm the liquid film becomes increasingly thinner, limiting the establishment of effective lateral capillary forces. We also suggest that at very high rotational speeds the imposed shear stress may also contribute to the disordering of the nanoparticle structuring by causing any adsorbed particles to detach, limiting nucleation sites for the establishment of lateral capillary forces and suppressing effective capillary self assembly of the colloidal particles. Similar behaviour has been observed in other systems [11] using nanoparticles and a silicon substrate.

5.7. Conclusions

Using mica substrates we have studied systematically the effects of changes in the colloidal concentration, the rotational acceleration and the rotational speed on the structuring of the colloidal particles. The interplay between these parameters allowed for the production of large scale highly crystalline monolayer formations of silica nanoparticles on mica.

Changes in the colloidal concentration had a marked effect on configuration of the particles on the substrate, a phenomenon that was emphasised by the polydispersity of our samples. We found that *size dependent* ordering occurred, where the largest particles formed highly ordered structures that were surrounded by increasingly smaller particles configured into polycrystalline or amorphous structures. At high concentrations (>25 g/L) this phenomenon was found to be suppressed by the surface particle density and increasingly amorphous structuring occurred.

With increases in the rotational acceleration we took 2D-FFT of the topography and from the radially averaged profiles found that the interparticle spacing increased with increasing acceleration, from close packed structuring at low accelerations to increasingly spaced packing at high acceleration (>800 rpm/s). We attributed this observation to the effects of liquid shedding, where increased acceleration rates caused rapid shedding of the bulk liquid, resulting in diminished lateral capillary forces and thus reduced ordering of the colloidal particle structure.

The rotational speed was found to govern the “crystallinity” of the samples, with the discovery of an optimum rotational speed for the experimental parameters used. The use of radial distribution function techniques was utilised to quantitatively measure the level of order observed in the samples. It was found that at low rotational speed a fluid crystal structure was formed due to poor distribution of the colloidal particles and delayed establishment of capillary forces, and conversely, at high rotational speed the excessively thin film limited the magnitude of the lateral capillary force between particles and excessive shear stress triggering erosion of any crystalline

structuring to amorphous configurations. This system behaviour was found to be in good agreement with results from other researchers who have used poly(methyl methacrylate) beads on a silicon substrate.

5.8. References

[1] I. Langmuir, Journal of the American Chemical Society 40 (1918) 1361-1403.
[2] J. M. Jethmalani, W. T. Ford, Chemistry of Materials 8 (1996) 2138-2146.
[3] J. M. Jethmalani, H. B. Sunkara, W. T. Ford, S. L. Willoughby, B. J. Ackerson, Langmuir 13 (1997) 2633-2639.
[4] A. van Blaaderen, R. Ruel, P. Wiltzius, Nature 385 (1997) 321-324.
[5] N. D. Denkov, O. D. Velev, P. A. Kralchevsky, I. B. Ivanov, H. Yoshimura, K. Nagayama, Langmuir 8 (1992) 3183-3190.
[6] A. S. Dimitrov, K. Nagayama, Langmuir 12 (1996) 1303-1311.
[7] X. J. Hu, A. Jain, K. E. Goodson, HT2005: Proceedings of the ASME Summer Heat Transfer Conference 2005, Vol 1 (2005) 641-644.
[8] K. Nagayama, Colloids and Surfaces a-Physicochemical and Engineering Aspects 109 (1996) 363-374.
[9] Y. H. Ye, S. Badilescu, V. V. Truong, P. Rochon, A. Natansohn, Applied Physics Letters 79 (2001) 872-874.
[10] A. Mihi, M. Ocaña, H. Míguez, Advanced Materials 18 (2006) 2244-2249.
[11] J. Moon, J. A. Park, S. J. Lee, T. Zyung, Japanese Journal of Applied Physics 47 (2008) 7968-7971.
[12] S. H. Im, Y. T. Lim, D. J. Suh, O. O. Park, Advanced Materials 14 (2002) 1367-1369.
[13] O. D. Velev, E. W. Kaler, Langmuir 15 (1999) 3693-3698.
[14] J. H. Fendler, Chemistry of Materials 13 (2001) 3196-3210.
[15] P. Hanarp, D. S. Sutherland, J. Gold, B. Kasemo, Colloids and Surfaces A - Physicochemical and Engineering Aspects 214 (2003) 23-36.
[16] P. Guyot-Sionnest, Microchimica Acta 160 (2008) 309-314.
[17] G. C. Qi, Y. L. Yang, H. Yan, L. Guan, Y. B. Li, X. H. Qiu, C. Wang, Journal of Physical Chemistry C 113 (2009) 204-207.
[18] J. N. Israelachvili, N. A. Alcantar, N. Maeda, T. E. Mates, M. Ruths, Langmuir 20 (2004) 3616-3622.
[19] M. Antonietti, J. Hartmann, M. Neese, U. Seifert, Langmuir 16 (2000) 7634-7639.
[20] M. Yamaki, J. Higo, K. Nagayama, Langmuir 11 (1995) 2975-2978.
[21] P. A. Kralchevsky, V. N. Paunov, I. B. Ivanov, K. Nagayama, Journal of Colloid and Interface Science 151 (1992) 79-94.
[22] T. Ogi, L. B. Modesto-Lopez, F. Iskandar, K. Okuyama, Colloids and Surfaces a-Physicochemical and Engineering Aspects 297 (2007) 71-78.
[23] T. J. Rehg, B. G. Higgins, Aiche Journal 38 (1992) 489-501.
[24] B. Smith, J. Vasut, T. Hyde, L. Matthews, J. Reay, M. Cook, J. Schmoke, Scientific Exploration, Planetary Protection, Active Experiments and Dusty Plasmas 34 (2004) 2379-2383.
[25] A. G. Emslie, F. T. Bonner, L. G. Peck, Journal of Applied Physics 29 (1958) 858-862.
[26] D. Meyerhofer, Journal of Applied Physics 49 (1978) 3993-3997.

Chapter 6: Polystyrene Nanoparticles on Mica

6.1. Abstract

We studied the nanostructures and ultrathin films resulting from the deposition and adsorption of polystyrene nanocolloidal particles and methoxy poly(ethylene glycol) methacrylate surfactants on mica surfaces from mixed suspensions in water. Samples were prepared by droplet evaporation and dip-coating and imaged with atomic force microscopy. Topography and phase imaging revealed a significant richness in morphological features of the deposited/adsorbed films. We observed uniform ultrathin films and extended islands of the surfactant oligomers indicating their self-assembly in monolayers and multilayers while the polystyrene nanoparticles were embedded within the surfactant structures. Droplet evaporation resulted in the migration of particles towards the edges of the droplet leaving an intricate network of imprints within the surfactant film. Dip-coating induced the formation of extended nanoparticle clusters with colloidal crystalline structuring.

6.2. Introduction

Colloidal science can range over a vast variety of subjects: from modelling the behaviour of atoms to the creation of smart materials for large-scale applications in many sectors of industry. One particular area of interest is the self-assembly of colloidal and nanocolloidal particles on surfaces. This has the potential to achieve nanostructures and nanopatterns for advanced products such as high-dense, defect-free data storage devices, sensors and biochips made for substantially lower cost than at the present and using more environmentally friendly materials and processes (suspensions of particles in water) [1-3]. In order for these colloidal particles to maintain their dispersion in a liquid suspension and not sediment out by flocculation, they must have repulsive interactions to counteract the ubiquitous attractive van der Waals forces. Colloidal particles are stabilized against this attraction either by electrostatic repulsion from surface charges [4] or with steric repulsions originating from anchored polymers or surfactants [5]. While an electrostatic interaction provides the basis of colloidal stability [6, 7] by repulsion between like surface charges, it is limited because it can be used only with polar liquid mediums and it is susceptible to flocculation with extremes in pH, salt concentration and temperature. Surfactant-based colloidal particles can be produced to provide the necessary interparticle repulsive forces in either polar or apolar mediums depending on the particular application such as targeted drug delivery [8, 9] and smart biosensors based on selective surfactant films [10]. One such surfactant is poly(ethylene glycol) (PEG) or poly(ethylene oxide) (PEO); Both terms signify the same chemical, but historically PEG has tended to refer to oligomers and polymers with a molecular mass below 20,000 g/mol and PEO to polymers with a molecular mass above 20,000 g/mol. PEG is widely used as a surfactant for stabilizing colloid water suspensions due to its water-solubility and its low toxicity makes it ideal candidate for biomedical applications [11]. Functionalisation of a colloidal surface by PEG can be achieved by combining the PEG with a suitable co-monomer which attaches to the colloidal surface, anchoring the PEG chain and thus creating a surfactant layer of steric repulsion.

The advent of scanning probe microscopy (SPM) techniques such as atomic force microscopy (AFM) has given us the ability to image and manipulate nanometer-sized particles. Apart from the high-resolution topographical imaging of a material surface, AFM [12] can also provide information on the physical properties of the material under investigation in the form of phase information [13, 14] due to its direct interaction with the surface at the atomic level. The phase-image contrast originates from the material's mechanical and adhesive properties, facilitating an indirect distinction between different materials/chemical species on the surface of a sample that would otherwise be undetected using topography imaging alone.

In this chapter, suspensions of polystyrene nanocolloidal particles copolymerised with methoxy poly(ethylene glycol) methacrylate (MeOPEGMA) surfactants were used. We deposited/adsorbed the suspension material onto mica by droplet evaporation and dip-coating. In both cases, nanostructures, (sub-)monolayers and ultrathin films were formed and studied with AFM topography and phase imaging in air. We observed the formation of highly ordered crystalline structuring of the polystyrene nanoparticles and evidence of self assembled ultrathin films of the surfactant which originated from the nanocolloidal suspension as suspended excess material. To the best of our knowledge this is the first time that such a system has been investigated and the results we present are of an exploratory nature.

6.3. Materials

The colloidal particles are made from the polymerisation of styrene molecules with a non-ionic comonomer/stabilizer, methoxy poly(ethylene glycol) methacrylate (MeOPEGMA) (Figure 6-1), in a process outlined by Ottewill *et al.* [15]. The MeOPEGMA polymer consists of a 2000 g/mol molecular weight PEG terminated on one end with a methoxy group. On the other end is a methyl methacrylate group which co-polymerised with the styrene and chemically linked the PEG stabilizer to the particles. This resulted in the formation of a colloid particle with a polystyrene core and PEG polymer on its surface which provides steric repulsion against aggregation/flocculation (PS-PEG). The particle diameters were measured to be 41± 10 nm by dynamic light scattering (DLS). The colloidal concentration was 13.7 g/L ($\phi = 1.304\times10^{-2}$).

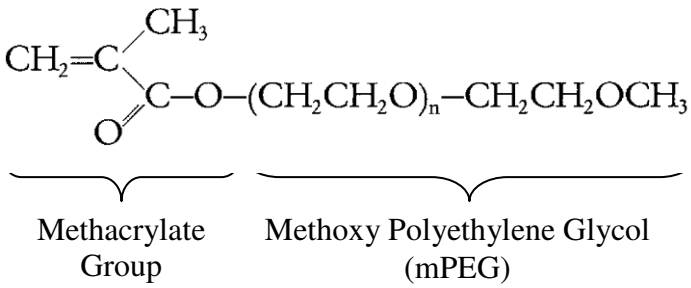

Figure 6-1. Chemical structure of the methoxy polyethylene glycol methacrylate (MeOPEGMA)

6.4. Experimental Methodology

Samples for imaging were prepared in two different manners: droplet evaporation and dip-coating. Mica sheets (Fisher, Leicestershire, United Kingdom), pre-cut in 11 mm squares, were freshly cleaved using a scalpel along the lateral plane of the sheet inside a fume cupboard to minimise airborne pollutants from contaminating the surface. The colloidal suspensions were agitated for 30 seconds to ensure

minimisation of any sedimentation that may have occurred. Droplet samples were created by applying 0.16 ml of the suspension using a pipette onto the freshly cleaved mica surface. The liquid droplet completely covered the mica surface and its contact line was 'pinned' onto the mica edge. Subsequently, the sample was placed into a drying box at room temperature/pressure, in an effort to avoid heterogeneous particles from contaminating the sample. These were left until the droplet had visibly evaporated, after which the sample was placed in a glass covered Petri dish and moved into an oven at 60 $^{\circ}$C for 1 h to ensure that any residual suspension liquid had evaporated. Dip-coating samples were prepared by submersion of the freshly-cleaved mica into a vial of the colloidal suspension in the upright position and left for a predetermined incubation time. The sample was then removed and rinsed gently with deionised water followed by drying from a nitrogen jet. The sample was then placed in a glass covered Petri dish and moved in an oven at 60 $^{\circ}$C for 1 h to ensure complete drying. If the samples were not imaged immediately after preparation, they were sealed with parafilm until imaged.

6.5. Measurements

Imaging was done using a Molecular Imaging PicoSPM AFM (Agilent Technologies, Santa Clara, CA, USA) operating in tapping mode (intermediate contact with the sample) using MikroMasch (Tallinn, Estonia) tips with a nominal spring constant and resonant frequency of 40 N/m and 170 kHz, respectively. The nominal tip radius was quoted as 10 nm. We operated in a light-tapping mode, where the contact amplitude approached the free oscillation amplitude of the cantilever, to minimise tip sample interaction forces. The cantilevers were oscillated at 5% below their natural resonance frequency. For post processing of the AFM images, Scanning Probe Image Processor (SPIP, Image Metrology, Hørsholm, Denmark) was used. All images presented are representative of the corresponding preparation protocol and were post-processed by simple flattening alone, unless otherwise stated.

6.6. Results

6.6.1. Droplet Application of PS-PEG Colloidal Suspension

On imaging a droplet-prepared sample near its centre, we were presented with a topography of islands of various sizes with a fractal-like edges, surrounded by an interconnected series of channels (Figure 6-2). The phase image shows a very high contrast between the islands and the surrounding network indicating that there is a difference in the mechanical/adhesive properties between the two, i.e. indicating a different material. A height profile of the surface (Figure 6-2d) reveals a uniform island thickness of approximately 13 nm.

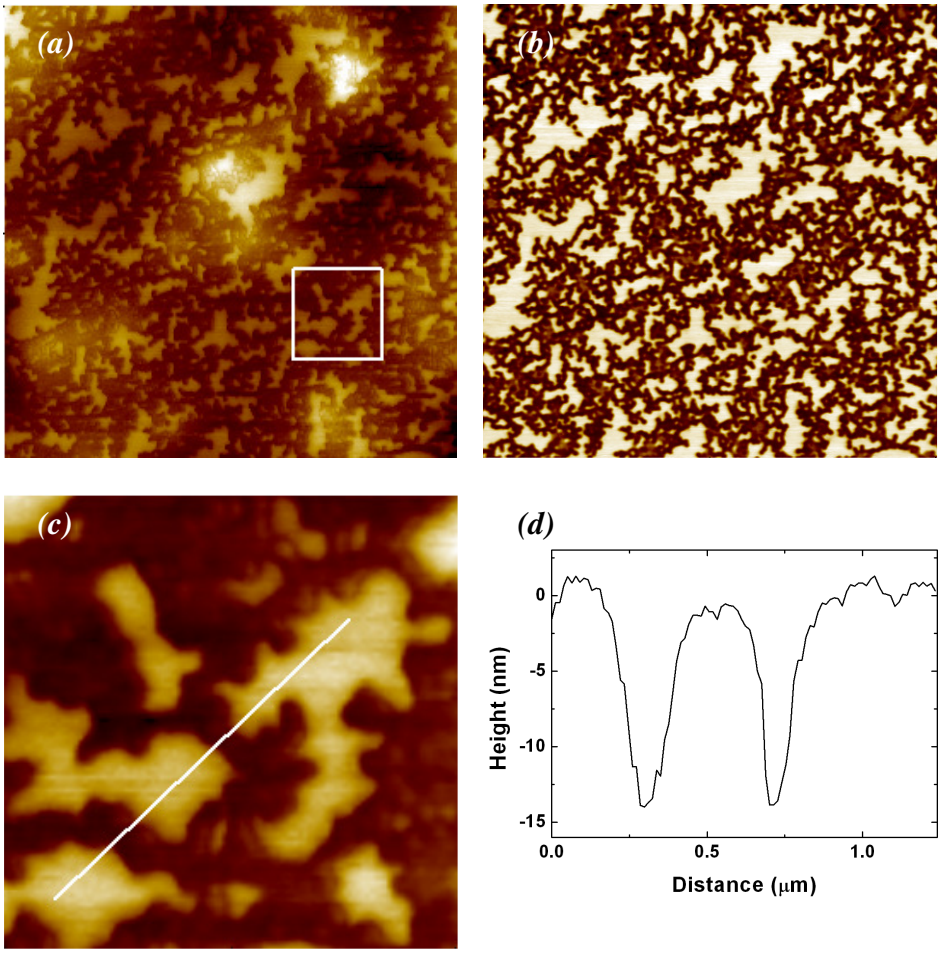

Figure 6-2. (a) 6.6 × 6.6 μm^2 topography AFM scan of the droplet-prepared sample (Z range 50 nm) with (b) associated phase image (voltage range 4.87 V) and (c) magnified section with (d) height profile corresponding to the white line in (c).

Figure 6-2 shows typical AFM data from a scan area towards the centre of the sample.

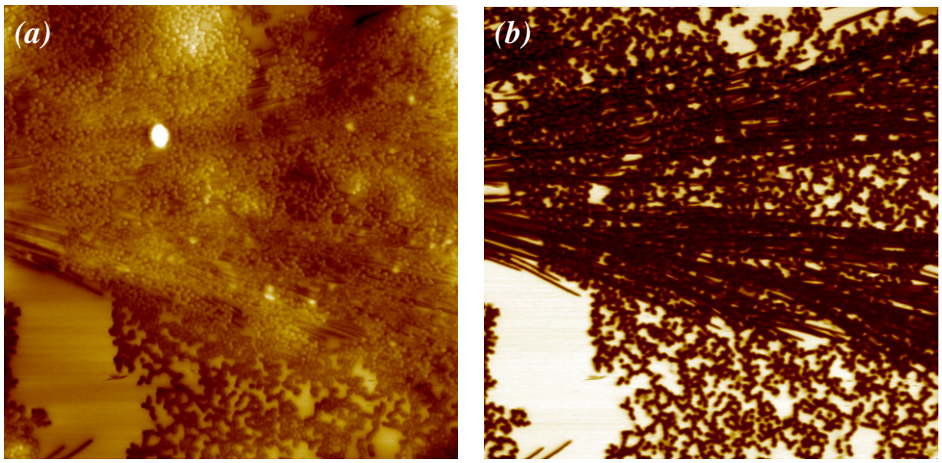

Figure 6-3. (a) 6.6 × 6.6 μm^2 topography scan of the droplet sample with (b) its corresponding phase image (Z range is 70 nm and phase voltage scale ≈ 5.2 V).

Moving towards the periphery of the sample (Figure 6-3) we start to observe topographical changes. The topography shows the existence of particles towards the top of the scan image. We also observe the same network of interconnected channels (previously observed in Figure 6-2). The middle of the sample exhibits some unusual trail lines, which are clearly present on the phase image. The depth of these lines is also approximately 13 nm. Towards the bottom of the topography image we see some isolated holes. The width of the isolated holes and trail lines are in the range of 40 nm.

6.6.2. Dip-Coating - Incubation Time 1 Hour

Figure 6-4 shows a typical example of an AFM image for a dip-coating sample for an incubation time of 1 h.

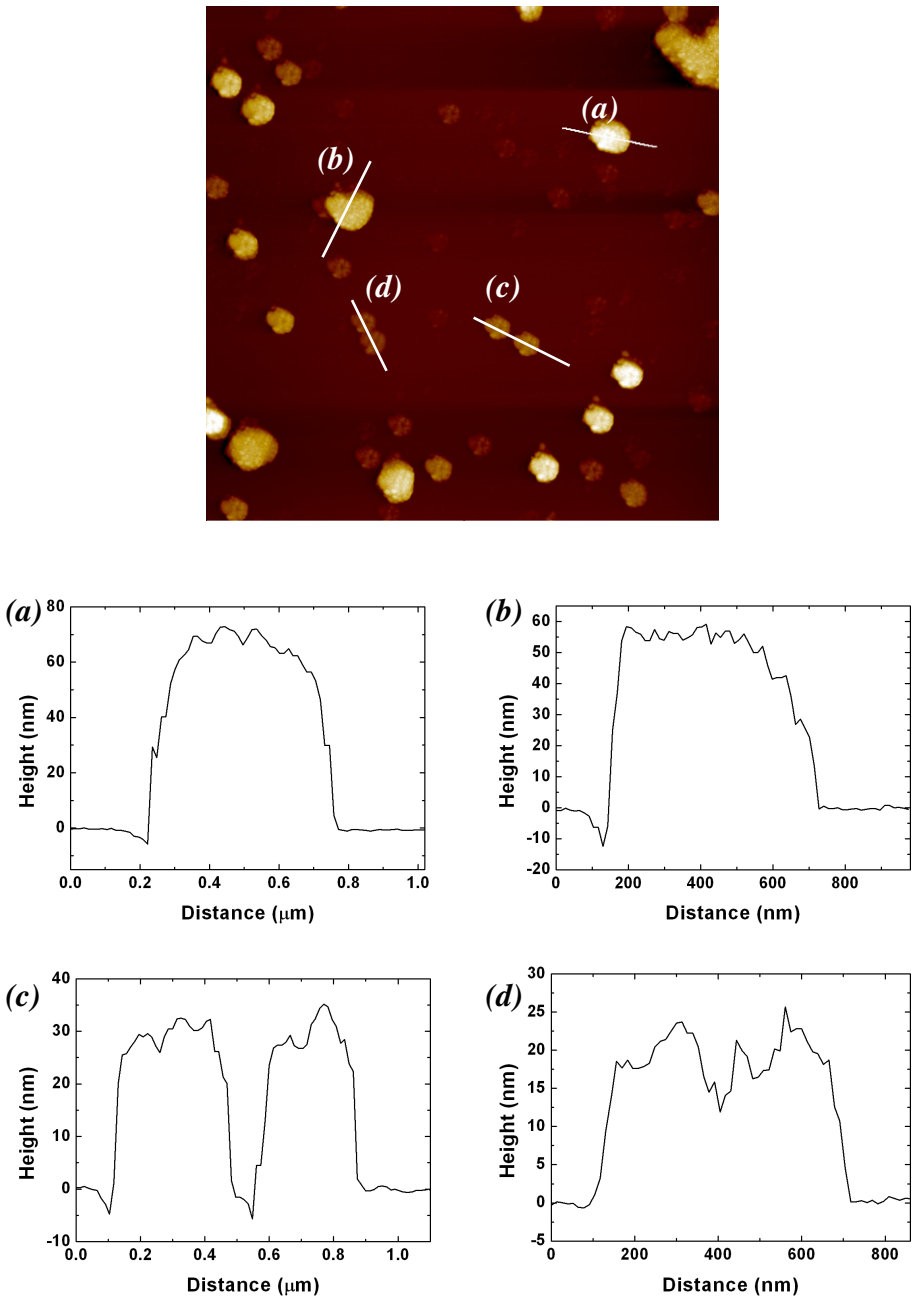

Figure 6-4. 6.6 × 6.6 μm^2 topography scan of the 1 hour incubation sample (Z range 80 nm) with height profiles of several of the colloidal clusters showing their relative height to the surrounding surface.

We observe the presence of numerous clusters of the particles, with varying heights across the surface. We also present a selection of profiles taken across the topography image giving an indication that their heights have some preferred values: the taller clusters are approximately twice that of the lower clusters. This is clearly demonstrated by frequency histograms of z-heights (Figure 6-5) obtained by grain analysis of the cluster formations. It shows that the maximal z-height ranges have peaks at 30 nm and 60-80 nm. The area coverage has a peak value of approximately 10^5 nm^2.

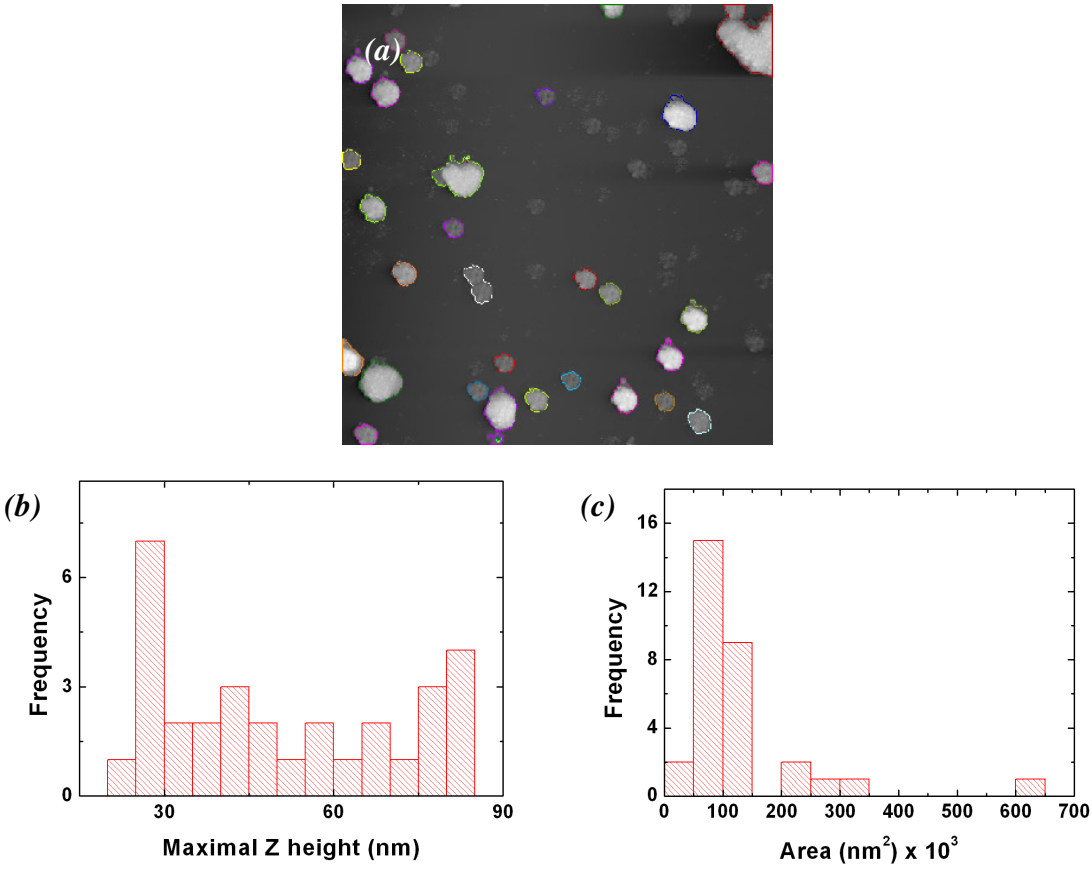

Figure 6-5. (a) Grain analysis of the 6.6 × 6.6 µm^2 topography scan of the sample submersed for 1 hour in PS–PEG. (b) Maximal z-height relative to the surrounding surface and (c) cluster area coverage.

6.6.3. Dip-Coating - Incubation Time 72 Hours

Increasing the submersion time to 72 h resulted in clearly-visible regular nanoparticle arrangements onto the mica substrate of various lateral sizes (Figure 6-6). We can also observe that the surrounding areas of the particle clusters have an extended border of uniform height. This layer has been measured to be approximately 12 nm thick (Figure 6-7) and can be found surrounding all particle adsorption sites. The phase image suggests that there is a distinct difference between the physical properties of this plateau layer and the underlying substrate.

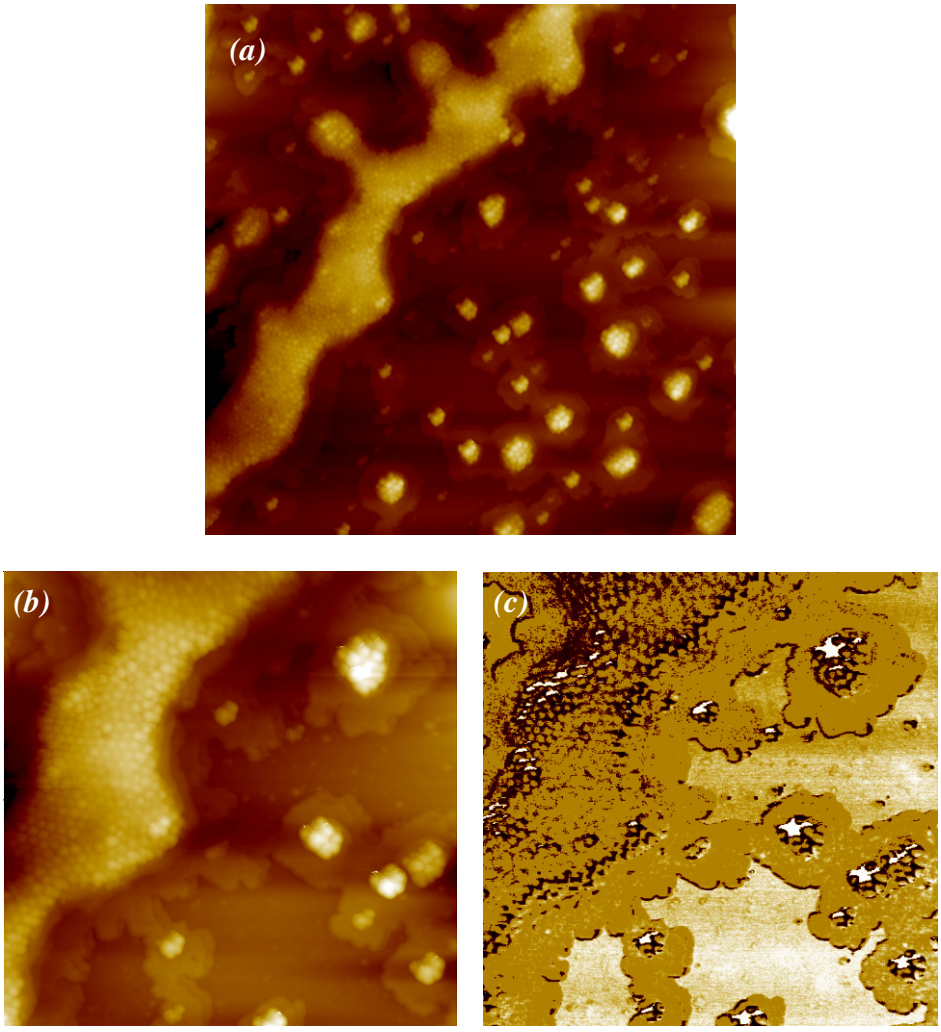

Figure 6-6. (a) 6.6 × 6.6 µm^2 topography scan with (b) 3 × 3 µm^2 zoom scan and (c) its corresponding phase information (high contrast) of the sample submersed for 72 hours in PS – PEG. The Z range is 100 nm for both topography scans. Phase voltage range is 4.7 volts.

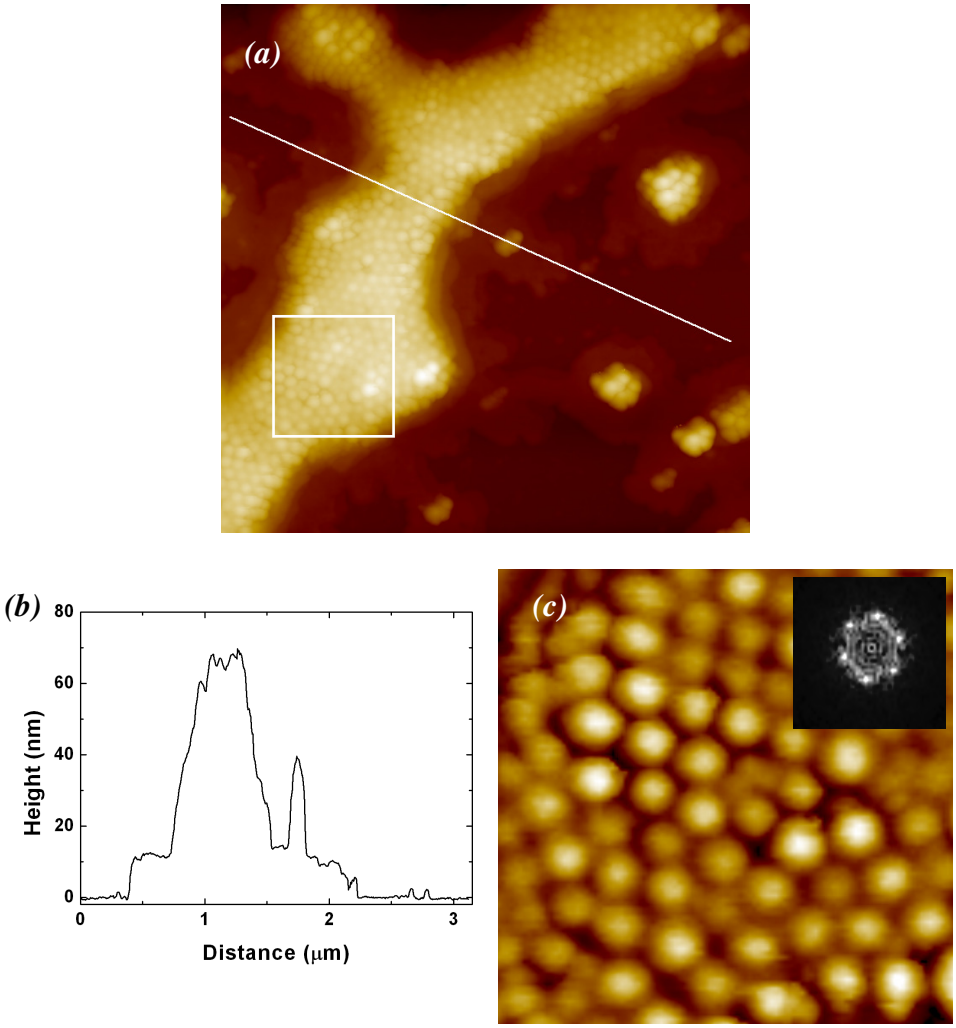

Figure 6-7. (a) (a) 3 × 3 μm^2 Topography scan (Z range is 100 nm) with (b) height profile of the larger structure shows a relative height of approximately 70 nm, an isolated small cluster at approximately 40 nm and a surrounding plateau height of approximately 12 nm. (c) Zoom of larger structure (imaged sharpened) showing highly crystalline structuring of the particles along with (insert) its 2D-FFT.

The structuring of the particles has been observed to be highly crystalline (Figure 6-7c). The particles are in a close packed hexagonal arrangement leading to very well ordered structure, as indicated by the fast Fourier transform (FFT). A characteristic length of 57 nm between the particles was evaluated from the FFT graph.

6.6.4. Dip-Coating - Incubation Time 240 Hours

After a submersion time of 10 days, scattered protrusions across the topography image were observed (Figure 6-8). Height profiles of the protrusions relative to the surrounding surface gives a range of elevations. Grain analysis (Figure 6-9) of the topography images shows that there are well-defined peaks in the relative z-heights of the protrusions at approximately 15, 25, 40 and 70 nm. Area coverage of the protrusions show peaks at 5×10^3, 19×10^3 and 28×10^3 nm^2.

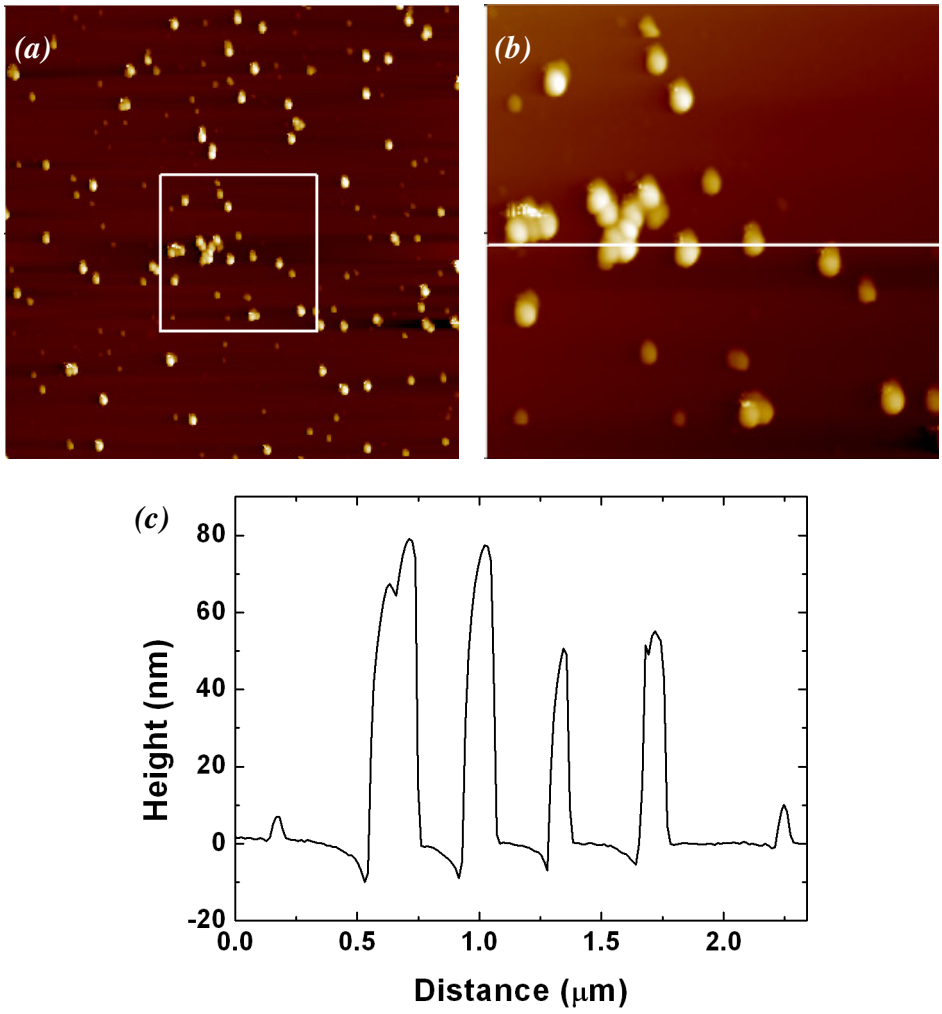

Figure 6-8. (a) 6.6 × 6.6 μm^2 topography scan of the sample submersed for 240 hours in PS–PEG. The Z range is 80 nm. (b) zoom section and (c) corresponding height profile.

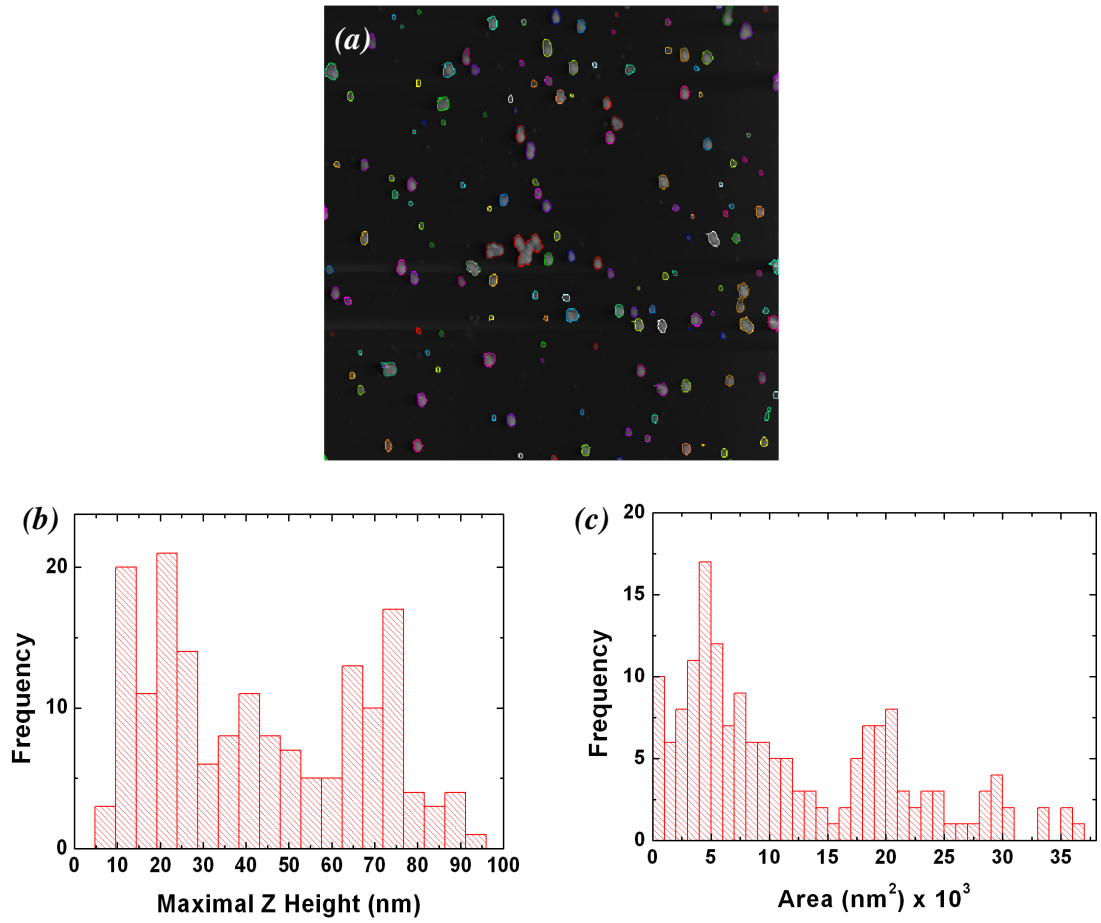

Figure 6-9. (a) Grain analysis of the 6.6 × 6.6 μm^2 topography scan of the sample submersed for 240 hours in PS–PEG. (b) Maximal z-height relative to the surrounding surface and (c) protrusion area coverage.

As we would have expected, increased submersion times create higher coverage of material on this sample than seen in the 72 h dip-coating experiments. We surmise that some sort of film layer has formed on the surface of the substrate of the 240 h samples. To investigate further, the tip was raised and the AFM reconfigured for contact mode. The set-point voltage to determine the tip contact force was raised to provide a sufficiently high enough cantilever tip-point force on the surface of the sample that would start to penetrate the film layer. The tip then scanned a square raster of approx. 1 × 1 μm^2 for 30 min that would effectively "dig" a hole into the surface through the film layer. The tip was then withdrawn and a tapping mode scan carried out over 4 × 4 μm^2 to image the dig site.

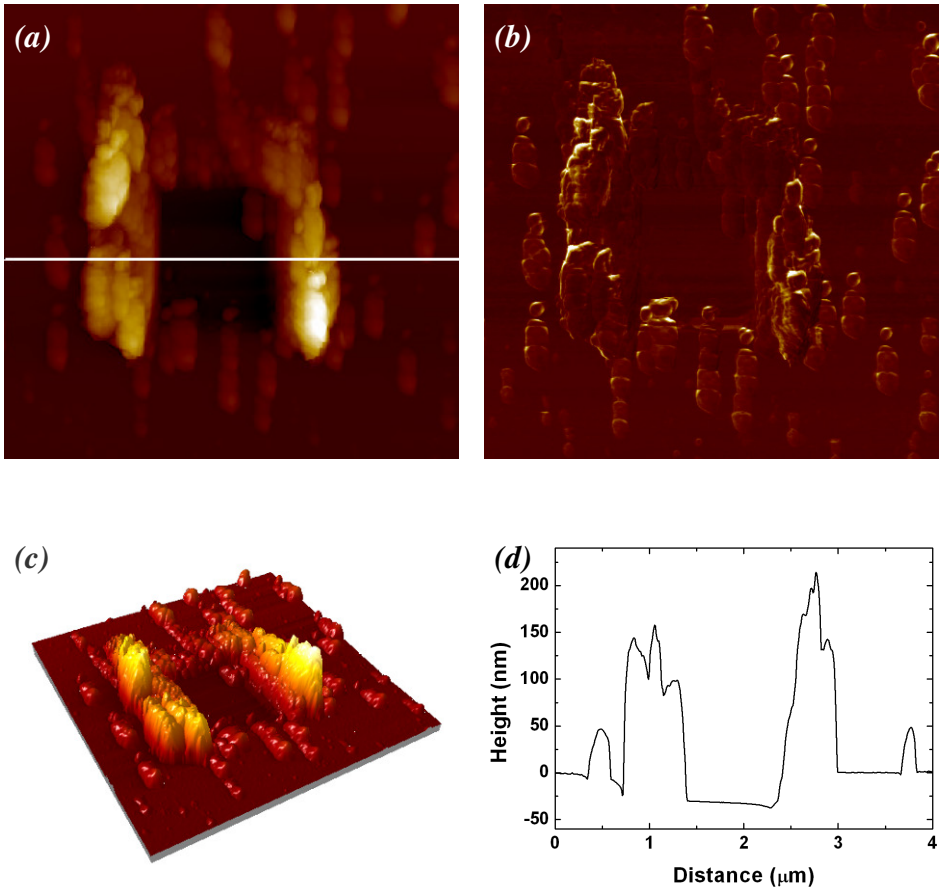

Figure 6-10. (a) 4 × 4 μm^2 topography scan of dig site on 240 hour incubation sample with (b) phase image and (c) 3D rendering of the topography and (d) height profile of the dig site. The Z range is 300 nm and the phase voltage range is 4.6 volts.

As is shown in Figure 6-10 the dig area is clearly marked and appears to have material built up on either side. The hole is quite clean and well defined. Measurements (Figure 6-10d) put the depth of the hole to be approximately 32 nm over the majority of its area. The material to the sides varies considerably in height spanning 100-300 nm. In contrast, the material further away from the hole that was present before the digging is approximately 70 nm in height (relative to the bottom of the dig site), which is in agreement with the larger protrusions observed in Figure 6-8. It is interesting to note that the phase image in Figure 6-10 suggests that the film maybe even thicker than what we dug out, as there is no contrast and thus little discernable difference in the physical properties between the surface and the bottom of the dig site indicating the same material.

6.7. Discussion

Our observations (Figure 6-2) suggest that a uniform ultrathin film of the excess PEG surfactant in the colloidal suspension was formed on the mica surface during the droplet evaporation. The surfactant islands borders form an intricate pattern of circular domains of the size of the nanocolloidal particles. It seems that both PS-PEG nanoparticles and PEG surfactant molecules were initially deposited on the surface but upon the slow evaporation of the droplet the subsequent convection current flows within the droplet induced desorption and redeposition of the particles towards the periphery of the sample (Figure 6-3). This is aided by the steric repulsion that exists between the surfactant-coated mica substrate and the PS-PEG nanoparticles. Additional evidence for this hypothesis comes from the trail lines appearing towards the perimeter of the sample (Figure 6-3). These lines could be caused by the PS-PEG particle being dragged as opposed to lifted due to the thinning of the droplets contact line as it nears complete evaporation of the liquid. The existence of particles at the perimeter also suggests mass transport within the droplet. The initiation of convection flows within the droplet as it began to evaporate caused the nanoparticles that were initially deposited on the sample surface to be lifted or dragged along to the extremities. The mechanism of movement of suspended material towards the periphery is well documented in other experimental work as the "coffee stain effect" [16], where a pinned droplet will stream liquid towards the perimeter in order to replace the evaporating liquid carrying within it any particulates in suspension.

The apparent thickness of the thin film is approximately 13 nm which is compatible with a dense self-assembled monolayer (SAM) of the MeOPEGMA oligomer that has a contour length of about 16 nm [17]. We note that we have imaged in ambient conditions; due to the humidity in the environment and to the fact that both mica and PEG have a high affinity for water, there is the opportunity for the PEG SAM to be swollen [18]. The MeOPEGMA oligomer terminates at one end with a methyl methacrylate group which is hydrophobic while PEG is hydrophilic. If we consider that the PEG component of the surfactant has a very high affinity for water then there

would be no reason for it to adsorb onto the surface for any of the submersion samples [19, 20]; the methacrylate termination group however will be in a bad solvent when in water, and so will prefer to align to the mica surface. If this adsorption configuration occurred at a high enough adsorption density it would have the effect of creating a self assembled monolayer of surfactant chains in a brush regime.

The presence of excess PEG also creates a situation where depletion forces may be generated between the colloidal particles. The range and strength of the attraction between colloids can be varied by the addition of free non-adsorbing polymer to the colloidal dispersion (free and non-adsorbing as opposed to the polymers used to coat the particles for steric stabilization). These polymers, when in an appropriate solvent, behave as random coils with a defined radius of gyration. On average, they are excluded from a shell of thickness comparable to this radius of gyration around the colloidal particle, called the depletion zone. When two colloidal particles are brought together, these depletion zones will overlap and the total volume accessible to the polymer will increase. It is this increase in free volume that causes an effective attraction.

In the dip coating samples, we have also observed a layer of approx. 12 nm surrounding the nanoparticle structures (Figure 6-7). In these samples we also see some evidence of slight steps in the surrounding layer edge which could come from capillary forces as the liquid around the nanoparticle structure evaporates. We note that there is an evaporation process of the remaining ultrathin water domains at the micro/nanoscale for the dip-coating samples even if most of the liquid has been dried by nitrogen injection [18]. The surfactants exposed at the edge of the plateau will subside and tilt in some form creating small nm-size steps. Parallel layering to the sample substrate cannot be excluded.

The clustering observed in the 1 h submersion samples (Figure 6-4) showed some interesting configurations. Grain analysis showed that the z heights relative to the surrounding surface had quite well-defined peaks at about 30 and 70 nm, suggesting

that there is evidence of bilayering occurring in the cluster structure. This is reinforced by the area histogram which has a very strong peak in the region of the ≈ 90×10^3 nm^2 indicating that there seems to be a preferred size for the area occupied by the cluster. The (≈ 10 nm) lower than expected height values could be the result of a thin film of surfactant having already formed on the mica substrate (approx. 12-13 nm). Thus, the height peaks compare well for a particle monolayer and bilayer since the particle size of the PS-PEG particle is ≈ 41nm.

The 240 h incubation samples were submersed for the longest time in this study and they had the highest material coverage of all the samples under investigation as shown by the digging experiment (Figure 6-10). The depth of the dig site (32 nm) indicates that there is a bilayer if not multilayer of the surfactant present on the mica substrate. The hydrophilic nature of the PEG combined with the hydrophobic methyl methacrylate termination would facilitate such multilayer lamellar structuring. This configuration could explain the range of protrusion sizes for these samples.

Further evidence for the multilayer surfactant formation comes from the grain analysis (Figure 6-9). The z-height histograms indicated reoccurring peaks relative to the surrounding surface at 15 nm, 25 nm, 40 nm and 70 nm. Peaks also appear on the area measurements at 5×10^3, 19×10^3 and 28×10^3 nm^2. This multimodal distribution suggests that there are regular separations in the z heights, the differences are in the region of 15-30 nm which would fit well with our proposed lamellar structuring of the surfactant. If this is the case then particles have become trapped on different layers of the surfactant; the multimodal distribution in the area measurements promotes this idea; particles at different but well defined depths will protrude through to the top layer creating a series of defined protrusions on the surface.

The FFT of the particle structures for the 72 h incubation time sample showed highly ordered crystalline structuring of the PS-PEG particles (Figure 6-7). It revealed that the characteristic length between the particles was 57 nm. The larger than expected length could be due to the presence of the dry surfactant layer between them. The

self-assembled crystalline structures were formed due to capillary/meniscus forces towards the final steps of the drying/evaporation; at this point the necessary interparticle forces required to draw the particles closely together were generated [21, 22]. A meniscus must exist between the particles of the suspension liquid in order to generate the capillary forces when the particles are still partially submerged in liquid at this point. As our tip radius is of the same order of magnitude as the particle diameter, tip convolution (Figure 6-11) may also result in the perception of particles appearing to be in a close packed formation even if they have a small gap between the particle-particle spacing.

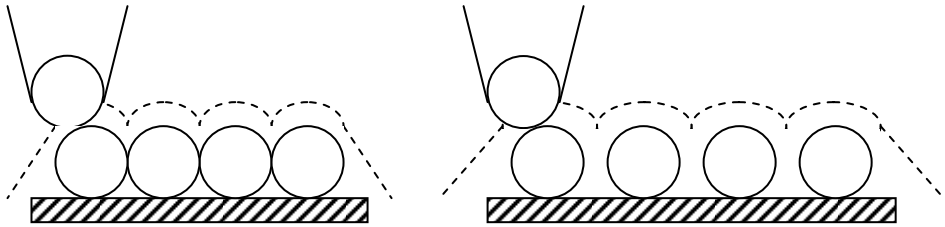

Figure 6-11. A Schematic diagram of the AFM tip convolution effect on particle spacing of the adsorbed colloidal particle. Dashed line represents the topography as perceived by the tip.

6.8. Conclusions

We found that the PS-PEG colloidal suspension containing an excess of PEG-surfactant molecules have produced mixed monolayers, (sub-)monolayers and ultrathin films on the mica surface. Our AFM study indicates that the PEG surfactant organised into self assembled monolayers and multilayer ultrathin films. Flow currents during the droplet evaporation led to the desorption and redeposition of PS-PEG colloidal nanoparticles into the periphery of sample leaving the formation of an imprint of the particle deposition towards the centre of the samples and thus creating a 'fingerprint' of the nanoparticle initial structuring. The dip-coating samples showed a rich range of nanostructures including highly ordered domains of the PS-PEG particles at low incubation times and particles embedded in a multilayer surfactant ultrathin film at higher incubation times. To the best of our knowledge this system has not been studied before and our AFM study indicates the presence of very interesting nanostructures and nanopatterns which could be relevant for many applications.

6.9. References

[1] Y. Xia, B. Gates, Y. Yin, Y. Lu, Advanced Materials 12 (2000) 693-713.
[2] C. P. Martin, M. O. Blunt, E. Vaujour, A. Fahmi, A. D'Ale, L. D. Cola, F. Vögtle, P. Moriarty, Self-Organised Nanoparticle Assemblies: A Panoply of Patterns, Elsevier, 2008.
[3] K. J. Mutch, V. Koutsos, P. J. Camp, Langmuir 22 (2006) 5611-5616.
[4] C. Scherer, A. M. F. Neto, Brazilian Journal of Physics 35 (2005) 718-727.
[5] J. Ghodbane, R. Denoyel, Colloids and Surfaces a-Physicochemical and Engineering Aspects 127 (1997) 97-104.
[6] E. J. W. Verwey, The Journal of Physical and Colloid Chemistry 51 (1947) 631-636.
[7] B. Derjaguin, L. Landau, Acta Physicochimica Urss 14 (1941).
[8] C. J. Drummond, C. Fong, Current Opinion in Colloid & Interface Science 4 (1999) 449-456.
[9] V. P. Torchilin, Journal of Controlled Release 73 (2001) 137-172.
[10] O. D. Velev, E. W. Kaler, Langmuir 15 (1999) 3693-3698.
[11] H. Otsuka, Y. Nagasaki, K. Kataoka, Current Opinion in Colloid & Interface Science 6 (2001) 3-10.
[12] H. J. Butt, R. Berger, E. Bonaccurso, Y. Chen, J. Wang, Advances in Colloid and Interface Science 133 (2007) 91-104.
[13] I. Schmitz, M. Schreiner, G. Friedbacher, M. Grasserbauer, Applied Surface Science 115 (1997) 190-198.
[14] G. Bar, Y. Thomann, R. Brandsch, H. J. Cantow, M. H. Whangbo, Langmuir 13 (1997) 3807-3812.
[15] R. H. Ottewill, R. Satgurunathan, Colloid and Polymer Science 273 (1995) 379-386.
[16] R. D. Deegan, O. Bakajin, T. F. Dupont, G. Huber, S. R. Nagel, T. A. Witten, Nature 389 (1997) 827-829.
[17] T. Wang, J. Xu, F. Qiu, H. Zhang, Y. Yang, Polymer 48 (2007) 6170-6179.
[18] E. Glynos, S. Pispas, V. Koutsos, Macromolecules 41 (2008) 4313-4320.
[19] L. Chai, J. Klein, Journal of the American Chemical Society 127 (2005) 1104-1105.
[20] M. O. Geke, R. A. Shelden, W. R. Caseri, U. W. Suter, Journal of Colloid and Interface Science 189 (1997) 283-287.
[21] P. A. Kralchevsky, N. D. Denkov, Current Opinion in Colloid & Interface Science 6 (2001) 383-401.
[22] P. A. Kralchevsky, K. Nagayama, Langmuir 10 (2002) 23-36.

Chapter 7: Conclusions and Future Work

7.1. Conclusions

We have explored the behaviour of silica nanocolloidal particles on mica substrates and discovered several new aspects of their behaviour. Our initial investigations using dip coating applications have shown that the particles adsorb onto the surface in an irreversible manner, but possess lateral mobility due to the weak van der Waals attraction between the particle and the mica substrate. As such, the adsorption densities possible are greater than what one would expect from the usually assumed RSA for nanocolloidal systems; the particles can reconfigure on the surface to accommodate higher numbers. Another advantage of this lateral mobility is in the final structuring of the particles when drying the sample. Self assembly of the nanoparticles was confirmed to be via the establishment of lateral capillary forces due to the formation of liquid menisci between neighbouring particles that were sufficiently close to one another. We were able to image this process directly and observed physical evidence of the process at the nanometer scale, something that has never been achieved before for nanoparticles. However, our analysis of the behaviour using current theory of capillary force modelling showed discrepancies in the magnitude of the calculated energies. At this scale there is the possibility that continuum properties such as surface tension are no longer constant, or that there are other physical effects at work that are not accounted for in the current model. In any case, the validity of such equations begins to break down as other effects such as liquid film instability become increasingly predominant. This was confirmed in our studies with different nanoparticle sizes. While the 100 nm particles were observed to form highly crystalline structures, the 10 nm particles structuring is dominated by the effects of dewetting. Indeed the fact that the 50 nm particles lacked *any* defining structure suggests that it was coming under the influence of an array of constructive and destructive influences and not just simple capillary forces.

We find therefore that there is a lower limit to the particle size suitable for the formation of highly structured films of nanoparticles generated using drying techniques. While we were able to create highly ordered structures of a micrometer scale using such techniques, our efforts with spin coating produced *millimeter* scale

crystalline monolayer films. Spin coating techniques have been shown to be extremely effective in creating similar formations at a centimeter scale with 315 nm particles [1] but our attempts have shown it to also be successful with smaller nanoparticles. Even larger monolayer crystalline formations should be possible with further refining of our preparation methodology.

Finally our investigations with sterically stabilised nanocolloids produced two interesting results. Firstly, due to the high affinity of the PEG for the mica surface we created a system where the PS-PEG becomes irreversibly adsorbed onto the substrate. Secondly, for the droplet evaporation samples a 'functionalised' substrate was generated by the excess PEG in suspension. Nanoparticles initially became embedded on the PEG film but were subsequently removed due to convective flow in the drying droplet. This left an imprint of the particle structuring in the PEG film adsorbed on the substrate; such methodology could be exploited for nano-imprinting and template applications.

7.2. Further Work

7.2.1. Oppositely Charged Particle-Substrate Systems

While the majority of systems investigated in this thesis have involved electrostatically stabilised particles with an equivalent charge to the substrate, opposite charge systems have been observed to behave in a distinctly different manner. The electrostatic *attraction* between the colloidal particle and the substrate leads to irreversible adsorption, inhibiting lateral movement resulting in different particle configurations [2] . As the magnitude of the electrostatic force is governed by the electrostatic double layer, we have an alternative mechanism by which adsorption can be controlled. To further investigate this we would manufacture substrates with charge gradients using modified silicon wafers with a hydrophilic/hydrophobic gradient [3, 4] or surfactant modified mica substrates [5]. In this way the *transitional* change in behaviour will be observed on one system, something which has never been studied before. This would allow the formation of particle density/morphology gradients on surfaces which have applications in the lab on a chip industry.

7.2.2. Anisotropic Shaped Colloidal Particles

All the colloidal particles used in this thesis were spherical in their shape, and the majority of literature available is concerned with similarly spherical particles. The use of anisotropic shaped colloidal particles is becoming an increasingly explored area [6]. We have carried out some preliminary investigations with one such colloidal particle, Snowtex (Nissan Chemical America Corporation, Houston, TX, USA). These are elongated particles approximately 9-15 nm in width and 40-100 nm in length. They have shown some unique structuring properties (Figure 7-1) that warrant further investigation, in particular the role of surfactant stabilisation and their packing order at higher colloidal concentrations.

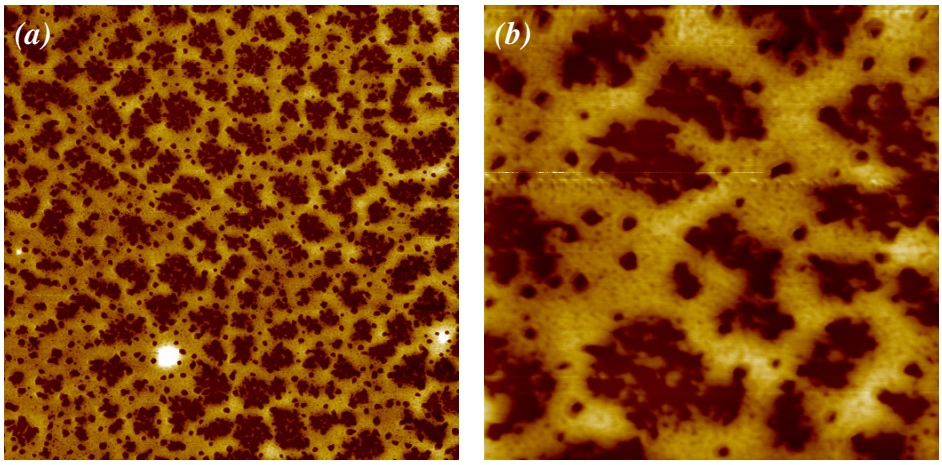

Figure 7-1. (a) 6.6 × 6.6 μm^2 and (b) 2 × 2 μm^2 topography images of a film structure composed of Snowtex particles with a PMMA surfactant for steric stabilisation. Z range is approximately 20 nm for both images.

7.2.3. Magnetic Colloidal Nanoparticles - Ferrofluids

We have also carried out some preliminary exploration into the behaviour of ferrofluids. Ferrofluids are nanoscopic particles of superparamagnetic material that have been stabilised with a surfactant and suspended in a carrier liquid. When exposed to an external magnetic field, the particles align to their respective net poles, causing the liquid's mechanical properties to change.

Continuing previous work done by our group [7], initial investigations into the effects of varying concentrations has shown a measurable effect on the topography. Low concentrations showed dispersed particle adsorption while at higher concentrations the formation of 2D cellular structures was found (Figure 7-2).

It is hoped that the magnetic aspect of this colloidal suspension can be exploited to create new and useful particle assemblies, simply by the application of a suitable external magnetic field.

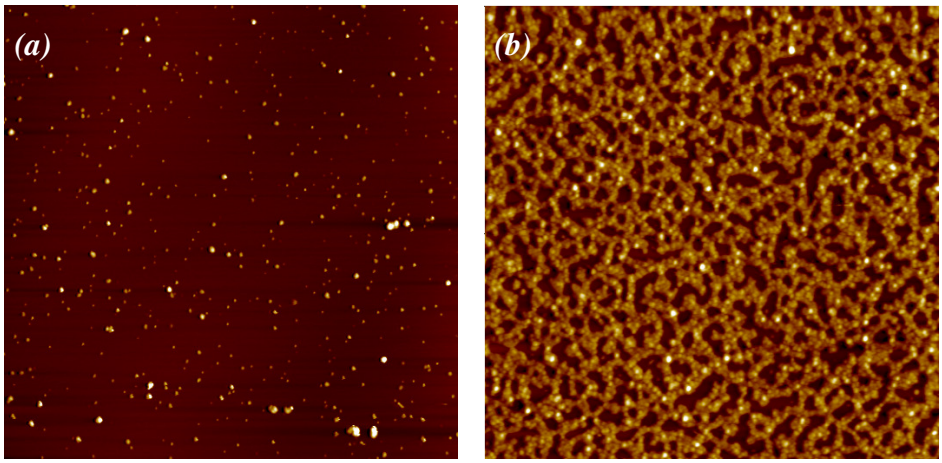

Figure 7-2. 6.6 × 6.6 μm^2 topography images of (a) ϕ = 3.3x10^{-7} and (b) ϕ = 3.3x10^{-5} volume fractions of magnetite ferrofluid particles of 10 nm adsorbed onto a mica substrate. Z range is approximately 30 nm.

7.2.4. Water Structures on Mica

For one sample of the 10 nm particles that was exposed to the open environment for an extended period of time there was an observable build up of liquid around the adsorbed nanoparticles. Height profiling measured the film thickness to be approximately 1.5 nm. This compares well with a water layer thickness observed on mica [8, 9]. The long-term effects of exposure to environmental humidity on nanoparticle structures of hydrophilic material warrant further investigation.

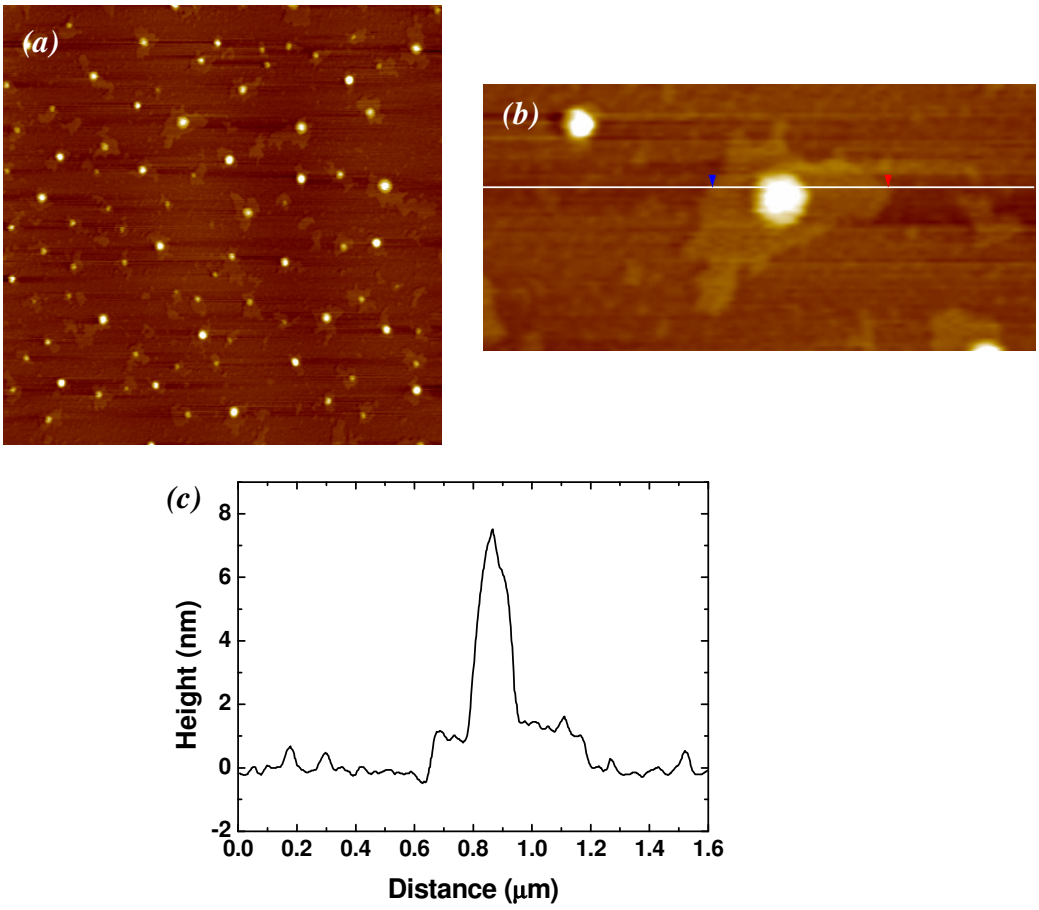

Figure 7-3. 6.6 × 6.6 µm^2 topography image of silica nanoparticles adsorbed onto mica, with a surrounding liquid film structure. (b) Zoom of one of the colloidal nanoparticles with (c) height profile of particle and liquid film.

7.3. References

[1] P. Jiang, T. Prasad, M. J. McFarland, V. L. Colvin, Applied Physics Letters 89 (2006) -.
[2] C. A. Johnson, A. M. Lenhoff, Journal of Colloid and Interface Science 179 (1996) 587-599.
[3] J. Ma, B. Y. Li, H. Y. Liu, Z. M. Zheng, J. Xu, Chinese Journal of Polymer Science 22 (2004) 131-135.
[4] M. Grundner, H. Jacob, Applied Physics a-Materials Science & Processing 39 (1986) 73-82.
[5] T. Nguyen, X. H. Gu, L. J. Chen, M. Fasolka, K. A. Briggman, J. Hwang, A. Karim, J. W. Martin, Abstracts of Papers of the American Chemical Society 227 (2004) U501-U501.
[6] S. C. Glotzer, M. J. Solomon, Nature Materials 6 (2007) 557-562.
[7] K. J. Mutch, V. Koutsos, P. J. Camp, Langmuir 22 (2006) 5611-5616.
[8] J. Hu, X. D. Xiao, D. F. Ogletree, M. Salmeron, Science 268 (1995) 267-269.
[9] M. Salmeron, J. Hu, X. d. Xiao, D. F. Ogletree, Surface Science 344 (1995) 221-236.